

Optical Whispering-Gallery Mode Resonators for Applications in Optical Communication and Frequency Control

Karen Grutter



Electrical Engineering and Computer Sciences
University of California at Berkeley

Technical Report No. UCB/EECS-2013-235

<http://www.eecs.berkeley.edu/Pubs/TechRpts/2013/EECS-2013-235.html>

December 20, 2013

Copyright © 2013, by the author(s).
All rights reserved.

Permission to make digital or hard copies of all or part of this work for personal or classroom use is granted without fee provided that copies are not made or distributed for profit or commercial advantage and that copies bear this notice and the full citation on the first page. To copy otherwise, to republish, to post on servers or to redistribute to lists, requires prior specific permission.

Optical Whispering-Gallery Mode Resonators for Applications in Optical Communication
and Frequency Control

by

Karen Esther Grutter

A dissertation submitted in partial satisfaction of the
requirements for the degree of
Doctor of Philosophy
in
Engineering - Electrical Engineering and Computer Sciences
in the
Graduate Division
of the
University of California, Berkeley

Committee in charge:

Professor Ming-Chiang Wu, Chair

Professor Clark Nguyen

Professor Liwei Lin

Fall 2013

Optical Whispering-Gallery Mode Resonators for Applications in Optical Communication
and Frequency Control

Copyright 2013

by

Karen Esther Grutter

Abstract

Optical Whispering-Gallery Mode Resonators for Applications in Optical Communication and Frequency Control

by

Karen Esther Grutter

Doctor of Philosophy in Engineering - Electrical Engineering and Computer Sciences

University of California, Berkeley

Professor Ming-Chiang Wu, Chair

High quality factor (Q) optical whispering gallery mode resonators are a key component in many on-chip optical systems, such as delay lines, modulators, and add-drop filters. They are also a convenient, compact structure for studying optomechanical interactions on-chip. In all these applications, optical Q is an important factor for high performance. For optomechanical reference oscillators in particular, high mechanical Q is also necessary. Previously, optical microresonators have been made in a wide variety of materials, but it has proven challenging to demonstrate high optical Q and high mechanical Q in a single, integrated device. This work demonstrates a new technique for achieving high optical Q on chip, a fully-integrated tunable filter with ultra-narrow minimum bandwidth, and the effect of material choice and device design on optical Q , mechanical Q and phase noise in microring optomechanical oscillators.

To achieve a high optical Q , phosphosilicate glass (PSG) is studied as a resonator material. The low melting point of PSG enables wafer-scale reflow, which reduces sidewall roughness without significantly changing lithographically-defined dimensions. With this process, optical Q s up to 1.5×10^7 are achieved, over ten times higher than typical silicon optical resonators.

These high- Q PSG resonators are then integrated with MEMS-actuated waveguides in a tunable-bandwidth filter. Due to the high Q of the PSG resonator, this device has a best-to-date minimum bandwidth of 0.8 GHz, with a tuning range of 0.8 to 8.5GHz.

Finally, microring optomechanical oscillators (OMOs) in PSG, stoichiometric silicon nitride, and silicon are fabricated, and their performance is compared after characterization via a tapered optical fiber in vacuum. The silicon nitride device has the best performance, with a mechanical Q of more than 1×10^4 and record-breaking OMO phase noise of -102 dBc/Hz at a 1 kHz offset from a 72 MHz carrier.

To my family

Contents

List of Figures	iv
List of Tables	xiv
1 Introduction	1
1.1 Overview of Optical Microresonators	1
1.2 Dissertation Organization	2
2 Theoretical Behavior of Optical Whispering Gallery Mode Resonators	4
2.1 Optical Whispering Gallery Modes	4
2.2 Evanescent Coupling to Optical Resonators	8
2.2.1 Coupled Modes of a Waveguide and Resonator	9
2.2.2 Propagation Constant of a Straight Rectangular Waveguide	11
2.2.3 Finding the Coupling Constant between a Waveguide and a Resonator	13
2.3 Summary/Conclusion	17
3 Cavity Optomechanics in Optical Microring Resonators	18
3.1 Overview of Cavity Optomechanics	18
3.2 Solving for Cavity Optomechanical Coupling	19
3.3 Other Effects that Depend on Cavity Power	26
3.3.1 The Kerr Effect in Optomechanical Resonators	27
3.3.2 Thermal Effects in Optomechanical Resonators	28
3.3.3 Photoelastic Effects in Optomechanical Resonators	30
3.4 Phase Noise in Cavity Optomechanical Oscillators	30
3.5 Summary	31
4 Achieving High Optical Q in Integrated Silica Devices	33
4.1 Factors Affecting Optical Q	33
4.2 Previous High Q_{opt} Resonators	34
4.3 Doped SiO ₂ as an Optical Resonator Material	35
4.4 Fabrication Process Development	36
4.4.1 Initial Results	38
4.4.2 Bubble Formation from Aggressive Reflow Conditions	40
4.4.3 Results from Post-Deposition Anneal Modification	42
4.5 Comparison to Previous Work and Implications	45

5	A Silica MEMS-Actuated Tunable-Bandwidth Filter	47
5.1	Previous Tunable-Bandwidth Filters	47
5.2	Device Design	48
5.2.1	MEMS Design	49
5.2.2	Optical Design	50
5.2.3	Fabrication Process Flow	52
5.3	Measurement	54
5.3.1	MEMS Characterization	54
5.3.2	Optical Measurements	54
5.4	Comparison to Previous Work and Outlook	57
6	Single-Material Optomechanical Oscillators	59
6.1	Previous Work	59
6.2	Device Design	61
6.2.1	Geometry	62
6.2.2	Materials	66
6.2.3	Layout	69
6.3	Fabrication	71
6.4	Measurement	73
6.4.1	PSG Optomechanical Resonator Measurements	76
6.4.2	Silicon Optomechanical Resonator Measurements	77
6.4.3	Si ₃ N ₄ Optomechanical Resonator Measurements	78
6.5	Device Performance Comparison	82
6.6	Outlook	85
7	Conclusion	87
	Bibliography	89
A	Whispering-Gallery Mode Code	97
A.1	TM Calculation	97
A.2	TE Calculation	100
A.3	Referenced Functions	104
B	Fabrication Details	106
B.1	Phosphosilicate Glass Etch Recipe	106
B.2	Silicon Etch Recipe and Sidewall Smoothing	106
B.3	Stoichiometric Silicon Nitride Etch Recipes	107

List of Figures

1.1	A waveguide coupling to a ring resonator. Light is sent into one end of the waveguide, and in the region where the ring and the waveguide are closest, that light interacts with the resonator mode, changing the output power in the waveguide depending on the degree of coupling between the two.	2
1.2	An example of an optomechanical resonator in phosphosilicate glass. Light travels in the whispering-gallery mode of the microring resonator and exerts radiation pressure radially outward on the outer edge of the ring.	3
2.1	Optical microdisk in a cylindrical coordinate system	5
2.2	A comparison of a numerically-calculated TM mode and a two-dimensional FEM eigenmode solution for a silicon microdisk ($n = 3.46$) with $R = 2.2 \mu\text{m}$ and $d = 220 \text{ nm}$. In the FEM, we set the disk refractive index to the calculated slab n_{eff} . The FEM resonant wavelength matches the calculated result. The contour plot shows E_z in the microdisk from a top view. We can determine the azimuthal mode number ℓ in the FEM by counting the cycles of E_z around the perimeter of the disk, and we find that it also matches the numerically-calculated value.	8
2.3	Optical power spectrum at the output of a waveguide coupling to an optical resonator. The optical frequency is represented by $\Delta\tau_0$, which is the detuning divided by the intrinsic linewidth of the optical resonator. The blue line, $\tau_{ex} = 0.2\tau_0$, is an example of overcoupling. The red line, where $\tau_{ex} = \tau_0$, is at critical coupling. Undercoupling is demonstrated by the green line, $\tau_{ex} = 7\tau_0$.	10
2.4	Cross section of a rectangular waveguide for reference when calculating its propagation constant. The coordinate system is chosen to correspond to that used for the whispering-gallery mode calculations, shown in Figure 2.1	11
2.5	Calculated propagation constants of a silicon waveguide and microdisk. For both, the thickness is $1 \mu\text{m}$, and the radius of the microdisk is $15 \mu\text{m}$. The propagation constants of each eigenmode of the resonator are represented by the dots, while the waveguides are represented by continuous lines. We calculated the propagation constant of waveguides with varied widths, and found a width for which the propagation constant matches that of the microdisk. (a) shows the calculations for the TM mode, and (b) shows the calculations for the TE mode.	13

- 2.6 Schematic of a waveguide coupling to a ring resonator for reference when analyzing the coupling constant c_m . (a) Top view of the coupling region. (b) Cross section of the waveguide and ring at the point of closest approach. 14
- 2.7 Examples of tuning the coupling constant between a 900-nm thick SiO₂ waveguide and microdisk resonator having a 50 μm radius ($\beta_{eq} = 5.14 \mu\text{m}^{-1}$). (a) The coupling constant c_m decreases exponentially as the gap between the waveguide and resonator increases. Here, we graph c_m for waveguides having different widths, and thus different propagation constants β . For $2w_1 = 2.8 \mu\text{m}$, $\beta_1 \approx 5.14 \mu\text{m}^{-1}$, matching the whispering-gallery mode β_{eq} . For $2w_1 = 420 \text{ nm}$, $\beta_1 \approx 4.07 \mu\text{m}^{-1}$. For $2w_1 = 3.5 \mu\text{m}$, $\beta_1 \approx 5.16 \mu\text{m}^{-1}$. (b) Tuning the waveguide's β_1 also changes c_m . Here, we set the waveguide width to $2w_1 = 900 \text{ nm}$, and we vary β_1 with respect to $\beta_2 = \beta_{eq}$ 15
- 2.8 Behavior of loaded Q_{opt} and measured power at the optical resonance frequency ω_0 as the gap is changed between a 900-nm thick SiO₂ waveguide having $2w_1 = 2.8 \mu\text{m}$ and microdisk resonator having a 50 μm radius. (a) The intrinsic Q_{opt} of the resonator is 10^5 . (b) The intrinsic Q_{opt} of the resonator is 10^7 16
- 3.1 A Fabry-Pérot optomechanical resonator. One of the mirrors is suspended on a spring, so it is mechanically compliant. (a) The cavity length is initially L , making the optical resonance frequency ω_0 . The pump laser ω_p is, in this case, blue-detuned from the optical resonance. The light in the cavity exerts radiation pressure on the compliant mirror. (b) The compliant mirror moves, increasing the cavity length to $L + \Delta L$. This shifts the cavity mode downward in frequency, reduces the proportion of the pump laser power that couples into the cavity, and decreases the radiation pressure on the mirror. 20
- 3.2 Sideband formation due to cavity length modulation. Stokes and Anti-Stokes sidebands form at $-\Omega_m$ and $+\Omega_m$ offsets from the laser frequency ω_p , respectively. (a) For blue detuning, the lower-frequency Stokes sideband has a larger magnitude than the Anti-Stokes sideband. (b) For red detuning, the higher frequency Anti-Stokes sideband has a larger magnitude than the Stokes sideband. 21
- 3.3 Spectra for non-sideband resolved and sideband-resolved optomechanical resonances, with the laser blue-detuned from the optical resonance. The Stokes and Anti-Stokes sidebands form above and below the pump laser wavelength, spaced by Ω_m . (a) In the non-sideband resolved regime, the optical resonance width is much greater than the mechanical frequency Ω_m . Both of the sidebands can fit within the optical resonance. (b) In the sideband-resolved regime, the mechanical frequency Ω_m is much larger than the optical linewidth, and the sidebands are too widely spaced to both fit within the optical resonance. As a result, in the case of blue-detuning, the Anti-Stokes sideband goes to zero. 23

- 3.4 Contour plots of the relative optical stiffness k_{om}/k_m with respect to the relative external photon lifetime τ_{ex}/τ_0 and the relative effective detuning $\Delta_{\text{eff}}\tau_0$. From left to right on the graphs, detuning goes from the red to blue regimes, and from bottom to top, the coupling changes from over- to under-coupled. (a) An example of a non-sideband-resolved device having mechanical frequency $\Omega_m = 20 \text{ MHz} \times 2\pi$ and $\tau_0^{-1} = 190 \text{ MHz} \times 2\pi$. (b) An example of a sideband-resolved device having mechanical frequency $\Omega_m = 500 \text{ MHz} \times 2\pi$ and $\tau_0^{-1} = 19 \text{ MHz} \times 2\pi$ 24
- 3.5 Contour plots of the relative optomechanical damping Γ_{om}/Γ_m with respect to the relative external photon lifetime τ_{ex}/τ_0 and the relative effective detuning $\Delta_{\text{eff}}\tau_0$. From left to right on the graphs, detuning goes from the cooling to amplification regimes, and from bottom to top, the coupling changes from over- to under-coupled. (a) An example of a non-sideband-resolved device having mechanical frequency $\Omega_m = 20 \text{ MHz} \times 2\pi$ and $\tau_0^{-1} = 190 \text{ MHz} \times 2\pi$. (b) An example of a sideband-resolved device having mechanical frequency $\Omega_m = 500 \text{ MHz} \times 2\pi$ and $\tau_0^{-1} = 19 \text{ MHz} \times 2\pi$ 25
- 3.6 Graphs of thermally-induced behavior of an optical resonator as it is interrogated by a tunable laser swept with decreasing frequency, starting blue-detuned from the intrinsic resonance. (a) The optical resonance ω_0 decreases as the laser is swept toward ω_0 , since the optical power coupling into the cavity is increasing, thereby increasing temperature. When the laser frequency drops below the temperature-shifted resonance, the power in the cavity drops, as does the temperature. Consequently, ω_0 returns to its original, intrinsic value. (b) This thermal effect is manifest in the optical spectrum measured at the coupling waveguide's through port. Instead of detecting a Lorentzian lineshape around ω_0 , the resonance shape is distorted. Lowering the optical input power reduces this distortion. 29
- 3.7 The Leeson model for phase noise in an oscillator indicates different noise sources and how they affect the shape of the noise spectrum with respect to the offset from the carrier frequency. In this example, the close-to-carrier slope is 30 dB/decade, indicating some additional $1/f$ noise source, such as vibration. Far from carrier, the noise is white, and the magnitude is set by sources such as thermal fluctuations and laser noise. The $1/f^2$ component comes from variations within the oscillator itself. 31
- 4.1 The theoretical effect of phosphorus content on silica viscosity. (Calculated from C.R. Hammond, *Physics and Chemistry of Glasses* **19**(3), pp. 41-42, 1978.) 36
- 4.2 Concept of PSG resonator with integrated, side-supported waveguide and grating coupler, including (a) overview of device, (b) cross-section of vertical grating coupler, (c) cross section showing side-supported waveguide coupling to resonator, and (d) finite element model of the optical mode in the side-supported waveguide 37

4.3	Fabrication process flow for PSG resonator with integrated waveguides and grating couplers, starting with an SOI wafer (a) Etch anchor vias through Si device layer (b) Deposit LPCVD PSG (c) Define in photoresist and fully etch devices (d) Define in photoresist and partially etch to form gratings and side-supported waveguides (e) Reflow PSG in N ₂ (f) Release in XeF ₂	38
4.4	SEMs of cross-sections of etched PSG	39
4.5	The reflow process has minimal effect on lithographically-defined dimensions. (a) Prior to reflow, the gap between the waveguide and resonator is about 510 nm. (b) Following a 4 hr reflow at 1050°C, the gap reduces to about 460 nm.	39
4.6	Measured Q_{opt} for varying thickness, reflow time, and reflow temperature . .	40
4.7	Doublet resonance from 2 μm thick, 50 μm radius disk reflowed for 4 hr at 1050°C. Measured via tapered fiber using a stepwise laser scan. Data is fit to a Lorentzian to determine the Q_{opt}	40
4.8	SEMs of cleaved PSG samples. (a) Cross-section of a 2 μm thick PSG film after 8 hr reflow at 1050°C. Bubbles are numerous but less than 10 nm in diameter. (b) Cross-section of a 3 μm thick PSG film after 4 hr reflow at 1100°C. Bubbles are larger than 10 nm in diameter. (c) Cross-section of a 2 μm thick PSG film that was deposited in two deposition/densification steps. After etch, PSG was reflowed 8 hours at 1050°C. Bubbles appear in two distinct groups.	41
4.9	Results from “oxidized” PSG process. (a) SEM cross-section of 2 μm thick PSG film annealed in N ₂ , O ₂ , and H ₂ O followed by device etch and 4 hr reflow at 1050°C. Bubbles could not be found under SEM. (b) Stepwise laser scan at 0.1 pm resolution of a resonance in 50 μm radius disk. Lorentzian fit of data indicates $Q_{opt} = 13.2$ million, but the number of points is too low to get a good fit of the resonance.	42
4.10	Measuring Q_{opt} with network analyzer and modulator. (a) Network analyzer measurement schematic. Optical resonance is probed by sidebands created by the modulator. Sidebands are scanned across resonance by changing modulation frequency ν . (b) Data from network analyzer measurement. Fit indicates $Q_{opt} = 14.7$ million.	43
4.11	Characterizing high Q_{opt} resonators with integrated, side-supported waveguides. Note that the resonators pictured here are spoke-supported rings instead of disks. These are useful as optomechanical devices and will be described in detail in Chapter 6. (a) We fabricated arrays of waveguide and resonators with varying spacing. To enable edge coupling, we dice perpendicular to the waveguides. (b) We coupled into the diced facets of the side-supported waveguides using lensed fibers mounted on separate micropositioning stages. Insertion loss was around 11 dB.	44
4.12	Measurement of Q_{opt} of a 50 μm radius spoke-supported ring, where the ring-waveguide spacing is 400 nm. The resonance was scanned via a tunable laser stepped at a resolution of 0.1 pm. The Lorentzian fit of the data yields a loaded Q_{opt} of 4 million.	45

4.13	Q_{opt} of notable optical disk and ring resonators with respect to device radius. (a) Si disk from [1] (b) Si disk from [2] (c) The high- Q_{opt} reflowed PSG from this work (d) SiO ₂ microtoroid from [3] (e) SiO ₂ wedge resonator from [4] (f) Thick stoichiometric Si ₃ N ₄ resonator from [5] (g) SiO ₂ /Si ₃ N ₄ hybrid ring resonator from [6] (h) SiO ₂ wedge resonator from [4] (i) SiO ₂ /Si ₃ N ₄ hybrid ring resonator from [6]	46
5.1	There are two main methods by which bandwidth tuning in optical filters has been accomplished. (a) In MZI-based tuning, a waveguide couples to the resonator in two places, and the relative phase between these two coupling points is changed by changing the propagation constant in the waveguide between the two points. This tunes the effective coupling constant between the waveguide and the resonator, thereby tuning the bandwidth. (b) In positional tuning, the distance between the waveguide and the resonator is changed. This changes the coupling constant, thus changing the bandwidth of the optical filter.	48
5.2	Schematic of silica tunable-bandwidth filter concept. The waveguide and resonator are suspended in air, while the MEMS actuator is implemented in silicon underneath the silica layer. The waveguide is “anchored” by lateral connections to the MEMS, and the resonator is anchored in its center.	49
5.3	Theoretical MEMS displacement with respect to applied voltage between the MEMS shuttle and drive electrodes. One curve shows the displacement while taking into account only the electrostatic force due to the sides of the comb fingers, while the other curve also includes the electrostatic force due to parallel-plate attraction between the comb finger tips and the base of the opposing comb. For small displacements, these two graphs match.	51
5.4	The coupling constant c_m between waveguides of varying width and a microdisk resonator with a 50 μm radius, as calculated using Eq. 2.20.	52
5.5	Optimized adiabatically-tapered junction for attaching a 1 μm -wide suspended waveguide to an anchor or the MEMS actuator. Beam propagation method simulations predict approximately 0.07 dB loss per junction.	52
5.6	Cross sections and top views of the fabrication process for MEMS-actuated PSG tunable-bandwidth filter. Cross sections are not of a specific cut across the device, but rather show representative components. The process begins with an SOI wafer with a thick ($\sim 25 \mu\text{m}$) device layer, on which we deposit 1 μm LPCVD PSG. (a) The PSG is partially etched to form contact pads. (b) We define and etch both optical and MEMS components in PSG. (c) While protecting optical components with photoresist, we etch most of the way into the SOI device layer. (d) All exposed Si surfaces are thermally oxidized. (e) We reactively-ion etch away the thermal oxide from all horizontal surfaces. (f) The device is released by isotropically etching Si in XeF ₂	53

- 5.7 SEMs of the fabricated tunable-bandwidth filter. (a) A perspective view, including the MEMS actuator as well as the waveguide and optical resonator. The waveguide and resonator are suspended in air while the comb drive still has a thick layer of silicon below the PSG layer. (b) A zoomed-in view of the waveguide coupling to the resonator. The PSG has been smoothed by the reflow process. Some compressive stress in the PSG has caused the waveguide to bow upwards by about 1 μm 54
- 5.8 The tunable-bandwidth filter is characterized optically with lensed fibers coupled to the ends of the waveguide. A tunable laser scans its wavelength stepwise across the optical resonance to determine the optical quality factor. The waveguide position is tuned by changing the DC bias between the MEMS shuttle and the drive combs. 55
- 5.9 Experimental measurements of the displacement with respect to voltage of a MEMS comb drive actuator designed for the tunable-bandwidth filter. The theoretical displacement curve (red line) is calculated from the theory presented in Section 5.2.1. The values used for the theoretical calculation are shown to the right. Of course, due to fabrication variation, these values may not exactly correspond to those of the fabricated device. 55
- 5.10 Measured optical resonance changes in a MEMS-actuated PSG tunable-bandwidth optical notch filter. (a) Spectra of a single optical resonance as the waveguide-resonator coupling gap is tuned. The widest resonance was for an applied bias of 84 V, and the narrowest was for an applied bias of 38 V. A larger bias results in a smaller coupling gap. For the narrower resonances, a resonance doublet is discernable. (b) The resonance wavelength shifted as the waveguide was moved. For smaller coupling gaps, the resonance wavelength was shorter. As the waveguide was moved away, the resonance wavelength increased, approaching the unloaded λ_0 of the cavity. The coupling gap here was approximated by fitting to the theory presented in Section 2.2.3. 56
- 5.11 Tracking of the measured loaded Q_{opt} and normalized minimum power in an optical resonance as the waveguide position was tuned. (a) Filter behavior with respect to the DC bias applied between the MEMS shuttle and the drive comb. Below a bias of about 55 V, the doublet resonance was undercoupled enough that the two resonances could be differentiated; for larger biasing, the resonances overlapped too much to distinguish between them. As a result, the Lorentzian fit of the data fits both resonances simultaneously and yields an artificially low Q_{opt} . (b) Tuning behavior with respect to the approximate gap between the waveguide and resonator, obtained by fitting to the theory presented in Section 2.2.3. The quality factor data does not appear to fit well because the measured Q_{opt} , when the two resonances of the doublet were indistinguishable, was artificially low. Also, for larger coupling gaps, the normalized power does not fit well. This is likely a consequence of the compressive stress in the waveguide, which causes the relationship between displacement and voltage to deviate from theory at the extremes of the positional tuning range. 57

6.1	FEM simulation of one of the optical whispering-gallery modes of a spoke-supported ring. Ring shape is indicated with white lines, and color shading shows relative electric field magnitude. Since the optical mode is radially symmetric, radiation pressure force F_{RP} is also radially symmetric.	62
6.2	FEM simulation of some mechanical eigenmodes of a Si ring having $R_o = 50 \mu\text{m}$ and $R_i = 30 \mu\text{m}$. Initial ring shape is indicated with black lines, and color shading indicates stress in device.	63
6.3	FEM simulation of the fundamental radially-symmetric mode of a Si spoke-supported ring having $R_o = 50 \mu\text{m}$ and $R_i = 40 \mu\text{m}$. Initial ring shape is indicated with black lines, and color shading indicates stress in device. The amount of perturbation of a ring's mode can be quantified by comparing its mechanical frequency to that of the ring without spokes.	64
6.4	FEM simulation of the second-order radially-symmetric mechanical mode of a Si spoke-supported ring having $R_o = 50 \mu\text{m}$ and $R_i = 40 \mu\text{m}$. Initial ring shape is indicated with black lines, and color shading indicates stress in device. The amount of perturbation of a ring's mode can be quantified by comparing its mechanical frequency to that of the ring without spokes.	65
6.5	Comparison of stress exerted on center anchor by four- and two-spoke resonators	65
6.6	FEM simulation of the fundamental radially-symmetric mechanical mode of a Si spoke-supported ring having $R_o = 50 \mu\text{m}$ and $R_i = 40 \mu\text{m}$, and anchored as via a "cloverleaf" anchor design. Initial ring shape is indicated with black lines, and color shading indicates stress in device.	66
6.7	Choosing optical ring widths using finite-element modeling	67
6.8	Two-dimensional FDTD simulation of final grating design at $\lambda = 1550 \text{ nm}$. Here, $h = 900 \text{ nm}$, $d_{PE} = 613 \text{ nm}$, $\Lambda = 1.355 \mu\text{m}$, and the angle of incidence is 5°	70
6.9	SEMs of fabricated PSG optomechanical devices. (a) A wide-angle view showing PSG resonator with integrated waveguide tapering to vertical grating coupler. (b) Cross-section of grating coupler, showing post-reflow shape of grating. (c) An anchored PSG resonator coupling to side-supported waveguide. (d) An anchored PSG stand-alone resonator.	71
6.10	Fabrication process for stand-alone Si optomechanical resonators (a) Start with an SOI wafer and deposit SiO_2 hard mask (b) Pattern and etch anchors down to Si substrate (c) Deposit thick poly-Si to fill anchor holes (d) Blanket etch poly-Si down to SiO_2 layer, leaving anchor filled (e) In photoresist, pattern the device layer and etch through SiO_2 and Si device layer (f) Release in vapor-phase HF or in HF followed by CPD	72
6.11	SEMs of stand-alone Si devices. (a) Top view of released thin (220 nm), $20 \mu\text{m}$ radius device. The small triangles in the middle of the "clover leaves" indicated where there is still sacrificial oxide attached to the underside following timed release. (b) Perspective view of released thick ($\approx 1 \mu\text{m}$), $15 \mu\text{m}$ radius device. This device is anchored with poly-Si.	72

- 6.12 Fabrication process for stand-alone stoichiometric Si_3N_4 optomechanical resonators (a) Start with a plain Si wafer and deposit at least $2\ \mu\text{m}$ SiO_2 sacrificial layer, then pattern and etch anchors down to Si substrate (b) Deposit about $400\ \text{nm}$ Si_3N_4 (c) Pattern photoresist and RIE the Si_3N_4 device layer (d) Release in buffered HF followed by CPD 73
- 6.13 SEM of fabricated Si_3N_4 stand-alone resonator having $r_o = 25\ \mu\text{m}$, $r_i = 17\ \mu\text{m}$, and $L_{\text{spoke}} = 14.5\ \mu\text{m}$ 73
- 6.14 Optomechanical device measurement setups (a) Measuring stand-alone devices with a tapered fiber. Tapered fiber, mounted on a separate micropositioning stage, is stretched across the sample and aligned to the resonator. (b) Measuring devices with integrated waveguides and grating couplers. Cleaved ClearCurve[®] fibers are mounted on custom fixtures and tightly curved (radius of curvature $\approx 5\ \text{mm}$) so they can couple to gratings at the correct angle while fitting under the microscope objective. 74
- 6.15 Measurement setup for optomechanical measurements. After coupling to the device under test (DUT) via either a tapered fiber or integrated waveguide, the optical signal is detected at the photodiode. The photodiode signal is amplified and sent either to an electrical spectrum analyzer (ESA) or the phase noise test set. Mechanical motion of the DUT is transduced to a modulation on the optical signal, which is seen as a resonance on the ESA. For devices with especially high threshold power P_{th} , an erbium-doped fiber amplifier (EDFA) is used to get enough power into the resonator to achieve self-oscillation. 75
- 6.16 Example of a measurement of threshold power P_{th} in air of a two-spoke PSG resonator with $r_o = 52.5\ \mu\text{m}$. Coupling to resonator was achieved via an integrated waveguide with edge-coupled lensed fibers. Based on the change in the mechanical resonance amplitude seen on the ESA with respect to input optical power, we estimate P_{th} to be about $240\ \mu\text{W}$, which is close to the theoretical approximation of P_{th} 76
- 6.17 Phase noise measurements in air and vacuum of a four-spoke PSG ring with $r_o = 52.5\ \mu\text{m}$. The mechanical mode that self-excited in these device was the fundamental radially-symmetric mode, which had $\Omega_m/2\pi = 18.6\ \text{MHz}$. After reducing air damping, Q_{mech} increased from 1200 to 7200 and phase noise improved by $7\ \text{dBc/Hz}$. P_{opt} for these measurements was chosen to optimize the phase noise. 77
- 6.18 Measured higher-order harmonics of the $67.2\ \text{MHz}$ fundamental frequency in a two-spoke PSG device with $r_o = 15\ \mu\text{m}$. This device was measured in air with an integrated waveguide and vertical grating couplers. To excite harmonics out to $500\ \text{MHz}$, the power at the device was approx. $30\ \text{mW}$ 77
- 6.19 Theoretical calculation of P_{th} with respect to photon lifetime due to coupling to the waveguide τ_{ex} and effective detuning from the optical resonance. This calculation is for a $220\ \text{nm}$ thick silicon optomechanical resonator with $r_o = 17.5\ \mu\text{m}$, $r_i = 13\ \mu\text{m}$, $Q_{opt} = 1.1 \times 10^5$, $\Omega_m/2\pi = 87\ \text{MHz}$, and $Q_{mech} = 1.7 \times 10^4$. 79

- 6.20 Phase noise measurements in vacuum of a four-spoke Si ring with $r_o = 20 \mu\text{m}$ pumped at two different optical resonances. One resonance had $Q_{opt} = 2.1 \times 10^5$ and the other had a $Q_{opt} < 10^5$. The mechanical mode was the fundamental radially-symmetric mode, $\Omega_m/2\pi = 77.3 \text{ MHz}$. The intrinsic Q_{mech} was 1.36×10^4 . The measurement at lower Q_{opt} has more close-to-carrier “technical” noise, but for medium offsets, the phase noise is improved (-97 dBc/Hz) with respect to the higher- Q_{opt} measurement (-94 dBc/Hz), as expected. P_{opt} for this measurement was chosen to optimize the phase noise. Clearly, Q_{opt} also greatly affects the amount of power needed for regenerative oscillations, since the lower- Q_{opt} measurement required 15 mW of optical power, whereas the higher- Q_{opt} measurement required only 700 μW 80
- 6.21 A comparison of Q_{mech} in one- and two-spoke Si_3N_4 resonators to that of four-spoke resonators. Graphed here is the difference between the four-spoke Q_{mech} and the two-spoke Q_{mech} with respect to device outer radius. Only one single-spoke resonator survived the fabrication process without sticking to the substrate, and that single point is also graphed. Data indicates that four-spoke resonators have consistently higher Q_{mech} than two-spoke resonators, and the single-spoke resonators also supports the trend that fewer spokes degrades Q_{mech} . In addition, the difference in Q_{mech} between four- and two-spoke resonators decreases as device radius increases. 81
- 6.22 Phase noise and Q_{mech} measurements of the best measured Si_3N_4 optomechanical oscillator. This device had $r_o = 25 \mu\text{m}$ and $\Omega_m/2\pi = 74 \text{ MHz}$ for the fundamental radially-symmetric mode. (a) Phase noise measurements in air and vacuum of a four-spoke Si_3N_4 ring resonator. The mechanical mode that self-excited in these device was the fundamental radially-symmetric mode. After reducing air damping, Q_{mech} increased from 1800 to 10400 and phase noise improved by about 7 dBc/Hz. P_{opt} for these measurements was chosen to optimize the phase noise. (b) Brownian motion measurement in vacuum of the Si_3N_4 ring. A Lorentzian fit of the data indicates the intrinsic $Q_{mech} = 10400 \text{ MHz}$ 83
- 6.23 Measured optomechanical frequency comb of the 74 MHz fundamental frequency in a four-spoke Si_3N_4 device with $r_o = 25 \mu\text{m}$, measured in vacuum. The interval between each “comb” is 74 MHz. To excite harmonics out to 1 GHz, the power at the device was approximately 5.5 mW. Even more harmonics become visible with higher input power; for a power at the device of 32 mW, harmonics out to about 3 GHz are visible above the noise. 83

6.24 A comparison of the phase noise of the best single-material devices presented in this chapter and the phase noise of previously-reported optomechanical oscillators. The phase noise in dashed lines is the approximate spectrum of the two reported OMOs in the literature. The SiO₂ microtoroid (green dashed line) was measured in air and had $Q_{mech} = 2000$, $\Omega_m = 217 \text{ MHz} \times 2\pi$. [7] The previously-reported Si₃N₄ ring OMO (blue dotted line) was measured in air at a laser power of 32 mW and had $Q_{mech} = 2000$ and $\Omega_m = 42 \text{ MHz} \times 2\pi$. [8] The performance metrics of the other resonators are listed in Figures 6.17, 6.20, and 6.22.(a) Raw phase noise data for these devices. (b) Phase noise of all devices scaled to 10 MHz.

List of Tables

2.1	Numerically-calculated TM fundamental radial modes around $\lambda = 1550$ nm for a silica microdisk having $R = 50$ μm and $d = 2$ μm	7
2.2	Numerically-calculated TE fundamental radial modes around $\lambda = 1550$ nm for a silica microdisk having $R = 50$ μm and $d = 2$ μm	7
3.1	Material parameters pertinent to the Kerr effect and thermal effects	27
4.1	Important optical parameters of common microprocessing materials around $\lambda=1550\text{nm}$	33
6.1	Key performance metrics of integrated radiation-pressure-induced cavity optomechanical devices	60
6.2	Important material parameters of SiO_2 , Si, and Si_3N_4	68
6.3	Summary of best results for Si devices	78
6.4	Summary of best results for Si_3N_4 devices	82

Acknowledgments

I wish to express my sincere gratitude to my adviser Professor Ming Wu for his encouragement and guidance throughout my research. I would also like to thank the other members of my dissertation committee, Clark Nguyen and Liwei Lin, for reviewing this dissertation.

I am also grateful to the members of the Integrated Photonics Lab. It has been a pleasure to work with all of them, and I learned a lot from our interactions. I would especially like to thank Ming-Chun Tien for his mentorship at the beginning of my graduate career. Also, I would like to acknowledge Anthony Yeh, Alejandro Grine, Niels Quack, Tristan Rocheleau, and Turker Beyazoglu, each of whom worked with me on different aspects of this work. Their perspectives and contributions were instrumental in helping me complete the work in this dissertation.

The staff of the Marvell Nanofabrication Laboratory were very important in enabling me to fabricate all the devices in this work. Not only did they maintain the equipment and respond cheerfully to equipment problems, they also gave me good advice on the best ways to use the tools.

Many people outside the university provided support to me during this process. I would especially like to acknowledge the members of the Veritas Graduate Christian Fellowship women's small group; their encouragement, advice, and perspective are much appreciated. Finally, I wish to thank my spouse Alexander Grutter for his practical help while I wrote this dissertation, including proofreading, cooking, and making sure I got some sleep, as well as for his unwavering confidence in my work for the past five years.

Chapter 1

Introduction

1.1 Overview of Optical Microresonators

Optical resonators come in a variety of geometries and sizes, from the 4 km-long Fabry-Pérot resonator at the Laser Interferometer Gravitational Wave Observatory (LIGO) [9] to a subwavelength metallodielectric “nanopatch” laser with a physical volume of approximately $0.03 \mu\text{m}^3$. [10] Just as mechanical and electrical resonators enable a wide range of devices, so optical resonators have been demonstrated to be important components in a many applications. Some examples include displacement sensors, [11], chemical sensors, [12] lasers, [10, 13, 14] optical delay lines, [15] and optical filters [16–20].

The canonical example of an optical resonator, the Fabry-Pérot resonator, has multiple optical resonances, which are dependent on the cavity length. Fabry-Pérot resonators can be implemented on-chip, but require some kind of highly-reflective, parallel mirrors precisely spaced. In on-chip devices, these mirrors are implemented vertically, via multi-layered distributed Bragg reflectors, [21] or horizontally, via ~ 100 nm-scale lithographically-defined gratings. [22] Both of these methods require precise and complex fabrication. In contrast, a microdisk or ring resonator, which is similar to a Fabry-Pérot resonator in that its multiple optical resonances are determined by the effective optical length around the cavity, can be implemented very simply with a single-mask, low-resolution process, and its input and output are in the plane of the wafer, making it easily integrable with on-chip photonic circuits. Thus, the optical dielectric microdisk resonator is a good candidate for utilizing the properties of optical resonators in integrated devices.

One of the key performance metrics of an optical resonator is its quality factor, a measure of how much light energy is stored in the resonator with respect to the light energy lost per resonance cycle. In dielectric microdisks, energy can be lost to absorption in the resonator material and scattering off of discontinuities either within the material or at its boundary. Minimizing these loss mechanisms narrows the resonance linewidth and increases the amount of light circulating in the cavity for the same input power.

Getting light into and out of the resonator is also crucial for any application. With dielectric microdisks, this is accomplished by evanescently coupling to the outer edge of the resonator with some type of dielectric waveguide, as shown in Figure 1.1. The waveguide acts as an additional loss mechanism to the resonator, so its presence changes the observed

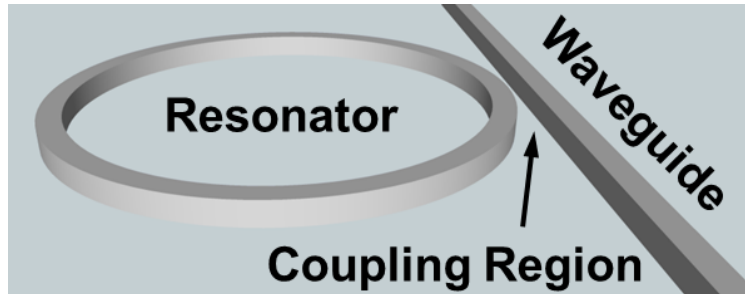


Figure 1.1: A waveguide coupling to a ring resonator. Light is sent into one end of the waveguide, and in the region where the ring and the waveguide are closest, that light interacts with the resonator mode, changing the output power in the waveguide depending on the degree of coupling between the two.

(“loaded”) quality factor of the system. The degree to which this coupling occurs is dependent on the waveguide dimensions, refractive index, and distance from the resonator. Controlling this coupling dynamically enables real-time tuning of the resonance linewidth, which is useful for optical filtering and correcting the power coupling ratio to the desired value after fabrication.

Even more interesting properties become evident for optical microdisk or ring resonators that are mechanically compliant, usually by being suspended in air instead of attached to a substrate. In such a device, motion of the resonator affects the amount of light coupling into it. If the intensity of the light in the resonator is sufficiently high, it exerts significant radiation pressure on the movable resonator boundary (see Figure 1.2), either amplifying or suppressing this motion. Further increasing the input optical power in an amplified optomechanical oscillator results in regenerative mechanical oscillations, and such a system can potentially be used as an all-optical reference oscillator.

In this work, we will present a method for integrating ultra-high optical quality factor microdisk resonators on a chip with integrated waveguides. Leveraging this technique, we will demonstrate a MEMS tunable-bandwidth optical notch filter with a narrow minimum bandwidth. In addition, we will explore the effects of material and design properties on optomechanical device performance in order to minimize noise in optomechanical reference oscillators.

1.2 Dissertation Organization

Chapter 2 describes the theory behind the optical modes in a whispering-gallery mode disk resonator. We then show how these modes couple to a waveguide and discuss how varying parameters can tune this coupling.

In Chapter 3, we describe a model for the optomechanical coupling in a cavity optomechanical device, aiming to highlight the important factors affecting this interaction. We focus specifically on behavior in the blue-detuned (amplified) regime. The influence of other nonlinear effects on these devices is also discussed. Finally, we examine a model for oscillator phase noise and how it applies to optomechanical oscillators in particular.

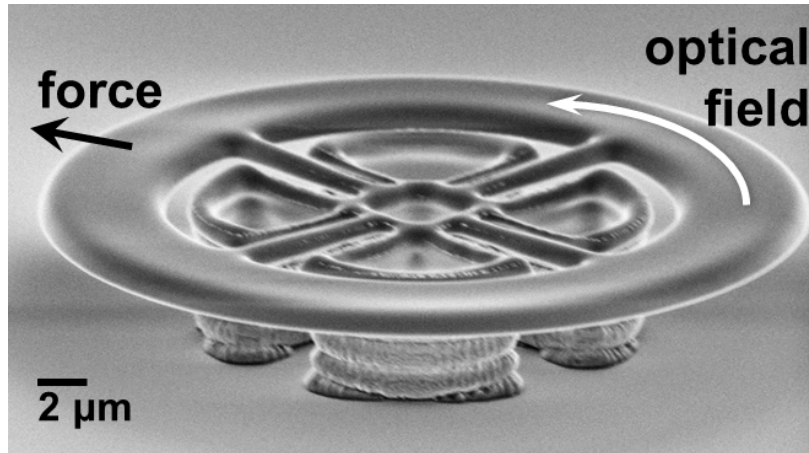


Figure 1.2: An example of an optomechanical resonator in phosphosilicate glass. Light travels in the whispering-gallery mode of the microring resonator and exerts radiation pressure radially outward on the outer edge of the ring.

We then present in Chapter 4 a new fabrication method for achieving high optical quality factor in on-chip silica resonators. The experimental results will be analyzed with a focus on the processing techniques which make the sidewall smoothing process described here most effective.

The fabrication process developed in Chapter 4 will then be used as a platform to develop a tunable-bandwidth optical notch filter in Chapter 5. The narrow minimum bandwidth of this device is made possible by high optical quality factor silica resonators, and the bandwidth is tuned via MEMS actuation of the coupling waveguide with respect to the resonator.

In Chapter 6, we present the optical and mechanical design and fabrication of optomechanical oscillators implemented in spoke-supported rings made of phosphosilicate glass, silicon, and stoichiometric silicon nitride. The performance of these devices is presented and compared, with the goal of finding the key parameters for minimizing phase noise.

Finally, Chapter 7 will conclude and summarize this work.

Chapter 2

Theoretical Behavior of Optical Whispering Gallery Mode Resonators

“Whispering gallery modes” (WGMs) are resonant modes that arise around the inside of circular or cylindrical cavities. First discovered as acoustic modes in the dome of St. Paul’s Cathedral and described mathematically by Lord Rayleigh in 1878, [23] WGMs can also form in optical and mechanical cavities. The optical WGMs of micron-scale dielectric disks and rings are especially interesting for their potential applications as on-chip optical resonators. These applications include filtering, [16–19] lasing, [14, 24] and optomechanical coupling. [7, 8, 25] In this chapter, we mathematically describe optical WGMs, and we show how waveguides can couple light into and out of them.

2.1 Optical Whispering Gallery Modes

We solve for whispering gallery modes of a microdisk resonator, diagrammed in Figure 2.1. We can approximately group the optical solutions into TM and TE, where the TM mode is defined by the electric field, which is dominated by E_z , and the TE mode is defined by the magnetic field, which is dominated by H_z . [26] To transform the system into two dimensions, we use the effective index method, and assume that the microdisk is thin enough that it only supports one mode in the z direction. Once the system has been reduced to an infinitely tall cylinder with refractive index n_{eff} , the mode of the resonator surrounded by air is as follows, where ψ is E_z for TM or H_z for TE [27, 28]:

$$\psi \propto \begin{cases} J_\ell(k_0 n_{eff} \rho) e^{-j\ell\phi + j\omega t} & \rho \leq R \\ H_\ell^{(2)}(k_0 \rho) e^{-j\ell\phi + j\omega t} & \rho > R \end{cases} \quad (2.1)$$

The variable k_0 is the wavenumber in free space, J_ℓ is the Bessel function of the first kind, and $H_\ell^{(2)}$ is the Hankel function of the second kind. (We assume that there are no incoming waves outside the cavity, so there are no Hankel functions of the first kind. [29]) We can write the rest of the field equations of microdisk in the slab mode approximation as follows [27, 30]:

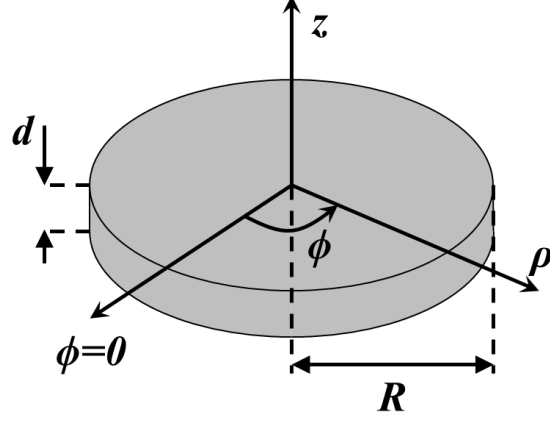


Figure 2.1: Optical microdisk in a cylindrical coordinate system

$$H_\rho = \frac{-j}{\mu_0 \omega} \frac{1}{\rho} \frac{\partial E_z}{\partial \phi} \quad H_\phi = \frac{j}{\mu_0 \omega} \frac{\partial E_z}{\partial \rho} \quad H_z = E_\rho = E_\phi = 0 \quad (\text{TM}) \quad (2.2a)$$

$$E_\rho = \frac{j \mu_0 \omega}{k_0^2 n^2} \frac{1}{\rho} \frac{\partial H_z}{\partial \phi} \quad E_\phi = \frac{-j \mu_0 \omega}{k_0^2 n^2} \frac{\partial H_z}{\partial \rho} \quad E_z = H_\rho = H_\phi = 0 \quad (\text{TE}) \quad (2.2b)$$

Here, n_{eff} is the slab effective index. Since k_0 and n_{eff} are dependent on the resonant wavelength $\lambda_{\ell m}$, we define the following variables:

$$U_{\ell m} = \frac{2\pi}{\lambda_{\ell m}} R n_{eff} \quad (2.3a)$$

$$Q_{\ell m} = \frac{2\pi}{\lambda_{\ell m}} R \quad (2.3b)$$

Here, ℓ and m are the azimuthal and radial mode numbers, respectively. We can now rewrite Eq. (2.1) at $t = 0$ in terms of these new coefficients:

$$\psi = \begin{cases} \psi_A J_\ell(U_{\ell m} \rho/R) e^{-j\ell\phi} & \rho \leq R \\ \psi_B H_\ell^{(2)}(Q_{\ell m} \rho/R) e^{-j\ell\phi} & \rho > R \end{cases} \quad (2.4)$$

By applying the boundary condition that the tangential components of H and E are continuous at $\rho = R$, we obtain the following eigenvalues:

$$\frac{H_\ell^{(2)'}(Q_{\ell m})}{Q_{\ell m} H_\ell^{(2)}(Q_{\ell m})} = n_{eff}^2 \frac{J_\ell'(U_{\ell m})}{U_{\ell m} J_\ell(U_{\ell m})} \quad (\text{TM}) \quad (2.5a)$$

$$\frac{H_\ell^{(2)'}(Q_{\ell m})}{Q_{\ell m} H_\ell^{(2)}(Q_{\ell m})} = \frac{J_\ell'(U_{\ell m})}{U_{\ell m} J_\ell(U_{\ell m})} \quad (\text{TE}) \quad (2.5b)$$

These equations can be numerically solved for the resonant wavelengths by choosing a $\lambda_{\ell m}$ to calculate the slab mode n_{eff} , then solving Eq. (2.5) for $\lambda_{\ell m}$. [31] Initially, the solution $\lambda_{\ell m}$ will not match the wavelength chosen to calculate n_{eff} , but the solution can be found by iterating through until the n_{eff} wavelength matches the eigenvalue solution. Alternatively, we can numerically build a function for n_{eff} with respect to λ , so that the eigenvalue can be expressed entirely in terms of $\lambda_{\ell m}$. Then, we can solve for the resonant wavelength without having to iterate, as in the first method. For our purposes, we are most interested in the fundamental radial mode $m = 1$, since it is the most confined of the radial modes.

Now, knowing the resonant wavelengths $\lambda_{\ell m}$, we can also find the equivalent propagation constant β_{eq} of each resonant mode. [32] This is the propagation constant that a mode with the same fields as the microdisk would have in a straight waveguide, and it is useful for analyzing how a waveguide would couple to the microdisk. First, we find an expression for the time average of the power propagating around the disk per unit height, as follows [30]:

$$P_{WGM} \approx \int_0^{R_c} \frac{1}{2} \left(\vec{E} \times \vec{H}^* \right) \cdot \hat{\phi} d\rho \quad (2.6a)$$

$$P_{WGM} \approx \frac{\ell}{2\mu_0\omega} \int_0^{R_c} \frac{|E_z|^2}{\rho} d\rho \quad (\text{TM}) \quad (2.6b)$$

$$P_{WGM} \approx \frac{\ell}{2\epsilon_0\omega} \int_0^{R_c} \frac{1}{n^2} \frac{|H_z|^2}{\rho} d\rho \quad (\text{TE}) \quad (2.6c)$$

Here, R_c is the ‘‘radiation caustic,’’ which is the radius outside of which the optical power radiates outward and inside of which the optical field is evanescent. The radiation caustic $R_c \approx \ell R/Q_{\ell m}$. [33] The corresponding equations for power in a slab waveguide are [30]:

$$P_{SW} \approx \frac{\beta}{2\mu_0\omega} \int_0^{R_c} |E_z|^2 d\rho \quad (\text{TM}) \quad (2.7a)$$

$$P_{SW} \approx \frac{\beta}{2\epsilon_0\omega} \int_0^{R_c} \frac{1}{n^2} |H_z|^2 d\rho \quad (\text{TE}) \quad (2.7b)$$

Setting the power in the whispering gallery mode (Eq. 2.6) equal to the power in the slab waveguide (Eq. 2.7), we can find the equivalent propagation constant of the whispering gallery mode [32]:

$$\beta_{eq} \approx \frac{\ell \int_0^{R_c} \frac{|E_z|^2}{\rho} d\rho}{\int_0^{R_c} |E_z|^2 d\rho} \quad (\text{TM}) \quad \beta_{eq} \approx \frac{\ell \int_0^{R_c} \frac{1}{n^2} \frac{|H_z|^2}{\rho} d\rho}{\int_0^{R_c} \frac{1}{n^2} |H_z|^2 d\rho} \quad (\text{TE}) \quad (2.8)$$

For the purposes of numerical calculations, we normalize the field to the value at the disk edge as follows:

$$\tilde{\psi} = \begin{cases} \frac{J_\ell(U_{\ell m} \rho/R)}{J_\ell(U_{\ell m})} & \rho \leq R \\ \frac{H_\ell^{(2)}(Q_{\ell m} \rho/R)}{H_\ell^{(2)}(Q_{\ell m})} & \rho > R \end{cases} \quad (2.9)$$

Table 2.1: Numerically-calculated TM fundamental radial modes around $\lambda = 1550$ nm for a silica microdisk having $R = 50$ μm and $d = 2$ μm

ℓ	$\lambda_{\ell m}$ (nm)	n_{eff}	β_{eq} (μm^{-1})
272	1563.73	1.4072	5.57
273	1558.43	1.4075	5.59
274	1553.16	1.4078	5.61
275	1547.92	1.4080	5.63
276	1542.72	1.4083	5.65
277	1537.56	1.4085	5.67
278	1532.43	1.4088	5.69

Table 2.2: Numerically-calculated TE fundamental radial modes around $\lambda = 1550$ nm for a silica microdisk having $R = 50$ μm and $d = 2$ μm

ℓ	$\lambda_{\ell m}$ (nm)	n_{eff}	β_{eq} (μm^{-1})
273	1563.26	1.4154	5.61
274	1557.91	1.4156	5.63
275	1552.60	1.4158	5.65
276	1547.33	1.4159	5.67
277	1542.09	1.4161	5.69
278	1536.88	1.4163	5.71
279	1531.72	1.4165	5.73

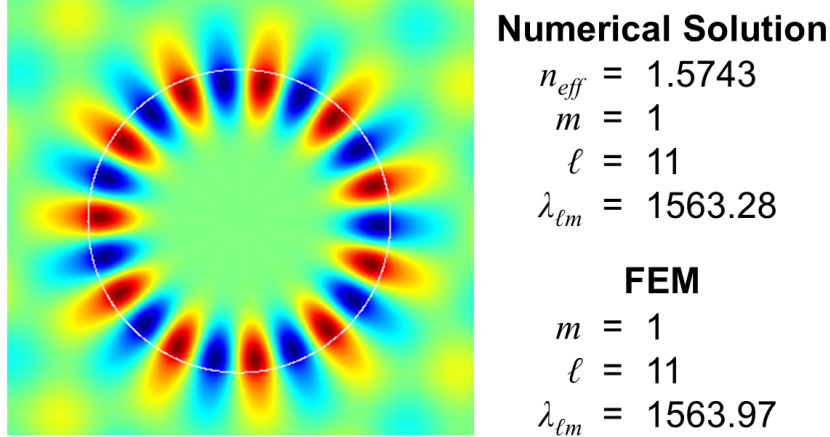


Figure 2.2: A comparison of a numerically-calculated TM mode and a two-dimensional FEM eigenmode solution for a silicon microdisk ($n = 3.46$) with $R = 2.2 \mu\text{m}$ and $d = 220 \text{ nm}$. In the FEM, we set the disk refractive index to the calculated slab n_{eff} . The FEM resonant wavelength matches the calculated result. The contour plot shows E_z in the microdisk from a top view. We can determine the azimuthal mode number ℓ in the FEM by counting the cycles of E_z around the perimeter of the disk, and we find that it also matches the numerically-calculated value.

This applies to both mode types, where $\tilde{\psi} = \tilde{E}_z$ for TM and $\tilde{\psi} = \tilde{H}_z$ for TE. As an example, we solve for the modes in a $2 \mu\text{m}$ -thick silica ($n_1 = 1.45$) microdisk with $50 \mu\text{m}$ radius, using the numerical code shown in Appendix A. Results for both TE and TM are shown in Tables 2.1 and 2.2. These calculations reveal another important parameter of the optical resonator: the free spectral range (FSR), which is the interval between adjacent modes. For example, based on Table 2.1, the FSR of that device around $\lambda = 1550 \text{ nm}$ is about 5 nm .

We can simulate the whispering gallery modes in a two-dimensional finite element model (FEM) by specifying the disk's refractive index as the slab effective mode index n_{eff} . Using this method, we find that the FEM wavelengths and azimuthal mode numbers match the numerically-calculated values well. An example of this matching is shown in Figure 2.2.

2.2 Evanescent Coupling to Optical Resonators

Now that we know the form of the whispering gallery modes that exist in optical microdisk resonators, we can consider how to get light into and out of the resonator. As was mentioned in the previous section, the optical field just outside the disk edge is evanescent. By introducing another interface, such as a waveguide, within that evanescent field, we may convert some of that light into a propagating mode. This also works in reverse, enabling us to send light into the resonator. In the case of a waveguide overlapping with the evanescent field, some of the evanescent field may couple into the waveguide mode and propagate along the waveguide. By choosing the waveguide dimensions and distance from the resonator, we can control how much power is coupled out of or into the resonator.

2.2.1 Coupled Modes of a Waveguide and Resonator

Starting with a simple system in which a light in a single waveguide is coupling to an optical resonator, we can express the field amplitude in the resonator with respect to time as [34]

$$\dot{\psi}(t) = \left(-j\omega_0 - \frac{\kappa}{2}\right) \psi(t) + \frac{s_{in}(t)}{\sqrt{\tau_{ex}}} \quad (2.10)$$

where ω_0 is the resonant frequency of the resonator, the total photon decay rate $\kappa = \tau_0^{-1} + \tau_{ex}^{-1}$, τ_0 is the intrinsic photon lifetime, τ_{ex}^{-1} is the rate of coupling to the waveguide, and s_{in} is the field amplitude in the waveguide. If we assume that the field amplitudes are $\psi(t) = \psi_0 e^{-j\omega t}$ and $s_{in}(t) = s_{in} e^{-j\omega t}$, where ω is the frequency of the input optical signal, we can solve for the field amplitude in the resonator and the power circulating in the resonator, where τ_{rt} is the round-trip time in the resonator and Δ is the detuning $\omega - \omega_0$:

$$\psi_0 = \frac{1}{\kappa/2 - j\Delta} \frac{s_{in}}{\sqrt{\tau_{ex}}} \quad (2.11a)$$

$$|s_r|^2 = \frac{|\psi_0|^2}{\tau_{rt}} = \frac{1}{\kappa^2/4 + \Delta^2} \frac{|s_{in}|^2}{\tau_{ex}\tau_{rt}} \quad (2.11b)$$

Of course, with a single waveguide probing the resonator, we are most interested in the signal at the output (“through port”) of the waveguide. The field amplitude at the through port is related to the input field amplitude by $s_{thru} = s_{in} - \psi_0/\sqrt{\tau_{ex}}$. [34] Thus, the through power is:

$$|s_{thru}|^2 = |s_{in}|^2 \left(1 - \frac{1}{\tau_{ex}} \frac{\kappa - 1/\tau_{ex}}{\Delta^2 + \kappa^2/4}\right) \quad (2.12)$$

which is a Lorentzian with linewidth κ . From this expression, we find three regimes of coupling, shown in Figure 2.3. The first regime is the overcoupled regime, which is when the photon lifetime due to the waveguide coupling is shorter than the intrinsic photon lifetime of the optical resonator ($\tau_{ex} < \tau_0$). In this regime, the Lorentzian linewidth of the resonance is $\kappa > 2/\tau_0$, and the power at ω_0 measured at the through port increases as τ_{ex} decreases.

The second regime is the critically-coupled regime, in which $\tau_{ex} = \tau_0$. When critically coupled, the full-width at half-maximum of the resonance is $\kappa = 2/\tau_0$, and the power $|s_{thru}|^2$ at the optical resonance frequency ω_0 is at its minimum possible value. For a system in which there are no other loss mechanisms, such as scattering off the waveguide, the through-port power at ω_0 is zero.

The final regime is the undercoupled regime, where $\tau_{ex} > \tau_0$. In this case, the resonator’s photon lifetime dominates the photon lifetime of the system. Thus, the linewidth of the resonance is $\kappa < 2/\tau_0$, and it approaches $\kappa = 1/\tau_0$ as τ_{ex} continues to decrease. Thus, by decreasing τ_{ex} , we can approximately measure the intrinsic photon lifetime and intrinsic optical quality factor $Q_{opt} = \omega_0\tau_0$ of the resonator. The through-port power at ω_0 is greater than the value at critical coupling, and it continues to increase as τ_{ex} grows.

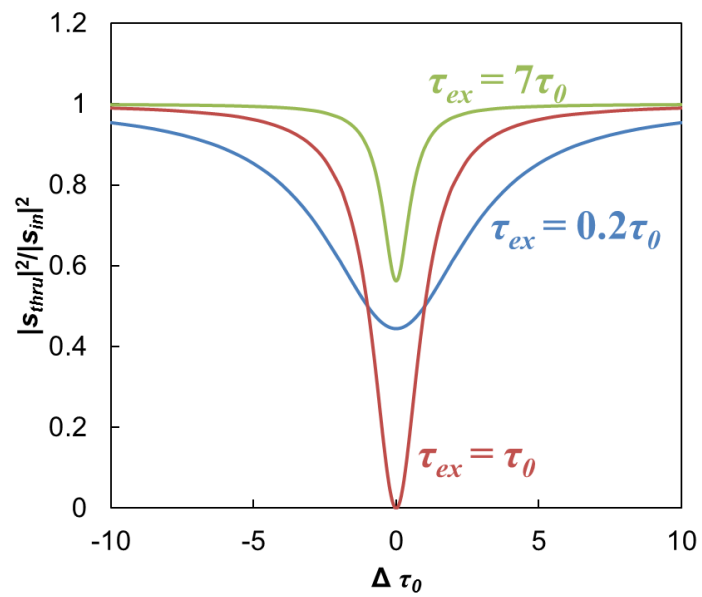


Figure 2.3: Optical power spectrum at the output of a waveguide coupling to an optical resonator. The optical frequency is represented by $\Delta\tau_0$, which is the detuning divided by the intrinsic linewidth of the optical resonator. The blue line, $\tau_{ex} = 0.2\tau_0$, is an example of overcoupling. The red line, where $\tau_{ex} = \tau_0$, is at critical coupling. Undercoupling is demonstrated by the green line, $\tau_{ex} = 7\tau_0$.

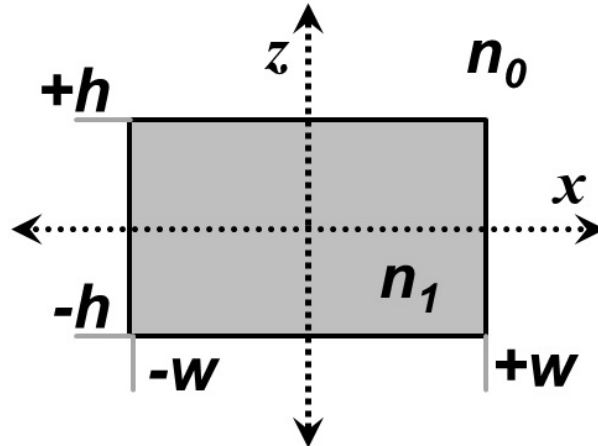


Figure 2.4: Cross section of a rectangular waveguide for reference when calculating its propagation constant. The coordinate system is chosen to correspond to that used for the whispering-gallery mode calculations, shown in Figure 2.1

Having found how a system of a single waveguide coupling to a resonator behaves with respect to τ_{ex} , it is useful to know on what factors τ_{ex} depends. We will derive this in the next two sections.

2.2.2 Propagation Constant of a Straight Rectangular Waveguide

Before evaluating the mode coupling between a straight waveguide and a resonator, we must first define the modes of the waveguide itself, shown in Figure 2.4. The coordinate system here is chosen to match that of the resonator. Marcatili first proposed a method for solving for the modes of a rectangular waveguide from Maxwell's equations. [30,35] Although this method neglects the field in the cladding at the corners of the waveguide (for example, the region where $x > w$ and $z > h$), its solutions are comparable to those found by other methods that incorporate these regions.

We start with the wave equations of this system. They can be broken up into two sets of solutions: one in which E_z and H_x are dominant, and one in which E_x and H_z are dominant. We call these TM and TE, respectively, to match the nomenclature used for the whispering-gallery mode solution. These are as follows:

$$\frac{\partial^2 H_x}{\partial x^2} + \frac{\partial^2 H_x}{\partial z^2} + (k_0^2 n^2 - \beta^2) H_x = 0 \quad (\text{TM}) \quad \frac{\partial^2 H_z}{\partial x^2} + \frac{\partial^2 H_z}{\partial z^2} + (k_0^2 n^2 - \beta^2) H_z = 0 \quad (\text{TE}) \quad (2.13a)$$

$$H_z = 0 \quad H_x = 0 \quad (2.13b)$$

$$H_y = -\frac{j}{\beta} \frac{\partial H_x}{\partial x} \quad H_y = -\frac{j}{\beta} \frac{\partial H_z}{\partial z} \quad (2.13c)$$

$$E_x = -\frac{1}{\omega \epsilon_0 n^2 \beta} \frac{\partial^2 H_x}{\partial x \partial z} \quad E_x = \frac{\omega \mu_0}{\beta} H_z + \frac{1}{\omega \epsilon_0 n^2 \beta} \frac{\partial^2 H_z}{\partial x^2} \quad (2.13d)$$

$$E_y = \frac{j}{\omega \epsilon_0 n^2} \frac{\partial H_x}{\partial z} \quad E_y = -\frac{j}{\omega \epsilon_0 n^2} \frac{\partial H_z}{\partial x} \quad (2.13e)$$

$$E_z = -\frac{\omega \mu_0}{\beta} H_x - \frac{1}{\omega \epsilon_0 n^2 \beta} \frac{\partial^2 H_x}{\partial z^2} \quad E_z = \frac{1}{\omega \epsilon_0 n^2 \beta} \frac{\partial^2 H_z}{\partial x \partial z} \quad (2.13f)$$

The first-order solution for the wave equation is of the following form:

$$\psi = \begin{cases} \psi_0 \cos(k_x x) \cos(k_z z) & -w \leq x \leq w \text{ and } -h \leq z \leq h \\ \psi_0 \cos(k_x w) \cos(k_z z) \exp(-\alpha_x(x-w)) & x > w \text{ and } -h \leq z \leq h \\ \psi_0 \cos(k_x x) \cos(k_z h) \exp(-\alpha_z(z-h)) & -w \leq x \leq w \text{ and } z > h \end{cases} \quad (2.14)$$

For TM, $\psi = H_x$, and for TE, $\psi = H_z$. Since the waveguide and cladding are symmetric, we need only solve the mode in the cladding to the right of and above the resonator. By substituting Eq. 2.14 back into Eq. 2.13a, we find that the wavenumbers must satisfy the following relations, in both TM and TE modes:

$$-k_x^2 - k_z^2 + k_0^2 n_1^2 - \beta^2 = 0 \quad (2.15a)$$

$$\alpha_x^2 - k_z^2 + k_0^2 n_0^2 - \beta^2 = 0 \quad (2.15b)$$

$$-k_x^2 + \alpha_z^2 + k_0^2 n_0^2 - \beta^2 = 0 \quad (2.15c)$$

We can farther simplify this by eliminating β :

$$\alpha_x^2 = k_0^2(n_1^2 - n_0^2) - k_x^2 \quad (2.16a)$$

$$\alpha_z^2 = k_0^2(n_1^2 - n_0^2) - k_z^2 \quad (2.16b)$$

From this point on, we only present the solution for the TM mode. The TE mode is easily found by following the same procedure. We now find the relationship between the transverse wavenumbers in the core k_x and k_z and the transverse wavenumbers in the cladding α_x and α_z by applying the boundary conditions of continuous tangential magnetic field at $x = w$ and continuous tangential electric field at $z = h$.

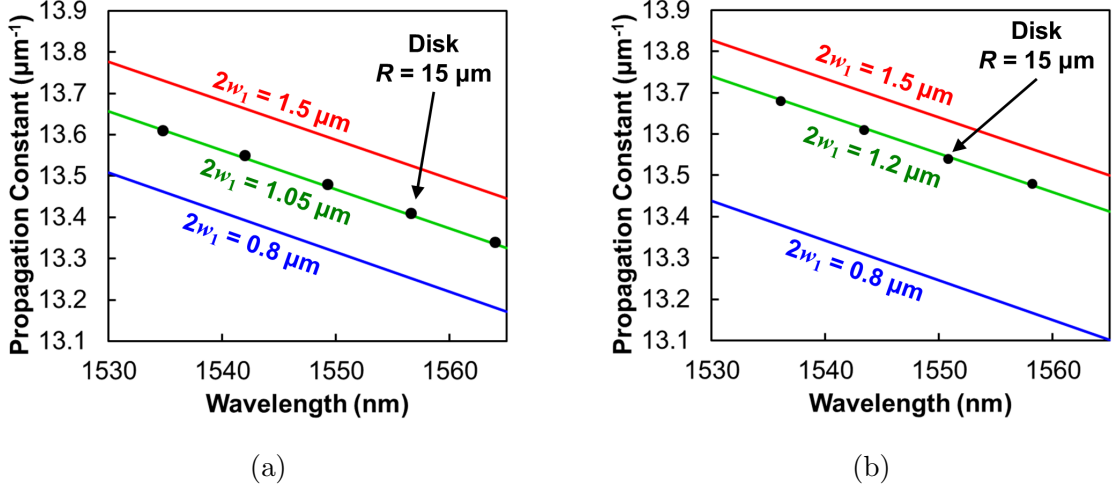


Figure 2.5: Calculated propagation constants of a silicon waveguide and microdisk. For both, the thickness is $1 \mu\text{m}$, and the radius of the microdisk is $15 \mu\text{m}$. The propagation constants of each eigenmode of the resonator are represented by the dots, while the waveguides are represented by continuous lines. We calculated the propagation constant of waveguides with varied widths, and found a width for which the propagation constant matches that of the microdisk. (a) shows the calculations for the TM mode, and (b) shows the calculations for the TE mode.

$$k_x w = \tan^{-1} \left(\frac{\alpha_x}{k_x} \right) \quad (2.17a)$$

$$k_z h = \tan^{-1} \left(\frac{n_1^2 \alpha_z}{n_0^2 k_z} \right) \quad (2.17b)$$

Now, using Eq. 2.16 and 2.17, we can obtain numerical values for k_x and k_z . With these and Eq. 2.15a, we can finally find the propagation constant of the waveguide. This value is especially important when coupling between a waveguide and a resonator, as having propagation constants that are too different results in a large phase mismatch, which decreases the efficiency of coupling between the waveguide mode and the resonator mode. Thus, we design waveguides to have matching propagation constants. An example is shown in Figure 2.5, where we see that choosing the right waveguide width enables simultaneous propagation constant matching for several of a resonator's optical modes.

2.2.3 Finding the Coupling Constant between a Waveguide and a Resonator

The rate of coupling between two waveguides (or, in our case, a waveguide and a ring) is specified by the coupling constant, which we define as $c_m = \tau_{rt}/\tau_{ex}$. In the case of a straight waveguide laterally coupling to an optical microring resonator, the coupling occurs over a short distance, so we can approximate it as a two-dimensional solution. We can

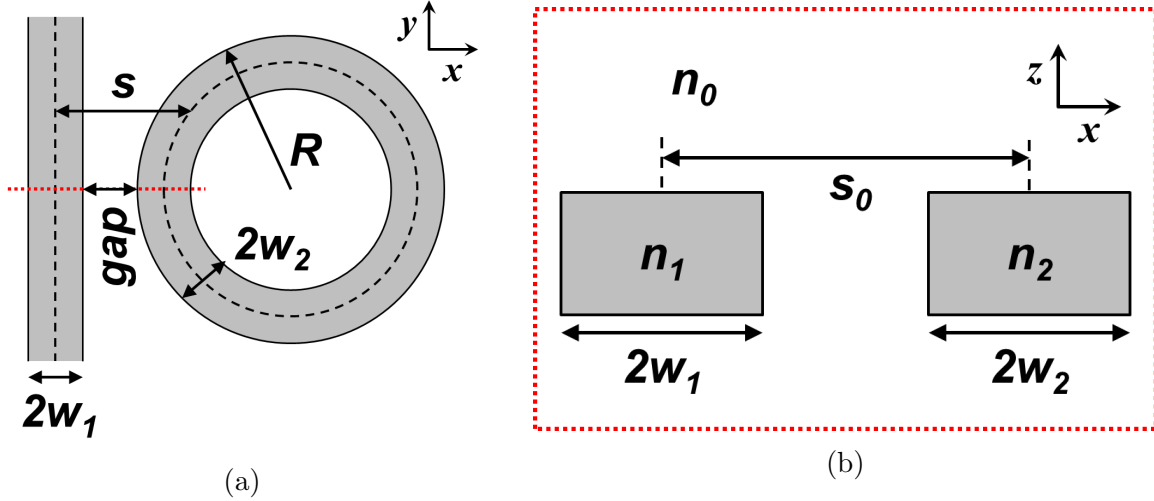


Figure 2.6: Schematic of a waveguide coupling to a ring resonator for reference when analyzing the coupling constant c_m . (a) Top view of the coupling region. (b) Cross section of the waveguide and ring at the point of closest approach.

further simplify the system by assuming the waveguide and resonator are infinitely thick, so there is also no z dependence. The coupling at some y position along the waveguide is an overlap integral of the optical fields \vec{e}_1 and \vec{e}_2 over the cross-sectional area. This is expressed as [36,37]

$$c_m^{1/2}(s(y)) = \frac{\epsilon_0 \omega}{4} \int_{-\infty}^{\infty} (n_1^2 - n_0^2) \vec{e}_1(x) \cdot \vec{e}_2^*(x) dx \quad (2.18)$$

where $s(y)$ is half the center-to-center spacing of the waveguide and ring with respect to y . To get the total coupling constant, we integrate along y in the coupling region:

$$c_m^{1/2} = \int_{-\infty}^{\infty} c_m^{1/2}(s(y)) \exp(-j(\beta_1 - \beta_2)y) dy \quad (2.19)$$

Here, β_1 and β_2 are the propagation constants of waveguides 1 and 2. To evaluate the integral, we approximate the center-to-center spacing of the waveguide and ring as a parabola with respect to y : $s(y) = s_0 + y^2/(2R)$. Using this to evaluate the integral in Eq. 2.19, Little, et al. found the following expression for the coupling constant between a straight waveguide and ring [36]:

$$c_m^{1/2} = \frac{\omega \epsilon_0 \cos(k_{x2} w_2)}{2\sqrt{P_1 P_2} (k_{x1}^2 + \alpha_2^2)} (n_1^2 - n_0^2) \sqrt{\frac{\pi R}{\alpha_2}} e^{\alpha_2(w_2 - 2s_0)} \dots \quad (2.20)$$

$$\times (\alpha_2 \cos(k_{x1} w_1) \sinh(\alpha_2 w_1) + k_{x1} \sin(k_{x1} w_1) \cosh(\alpha_2 w_1))$$

For waveguide i , k_{xi} is the transverse propagation constant, w_i is half the waveguide width, P_i is the power in the waveguide, α_i is the decay constant outside the waveguide, and n_i is the index of refraction. These values are calculated as follows [36]:

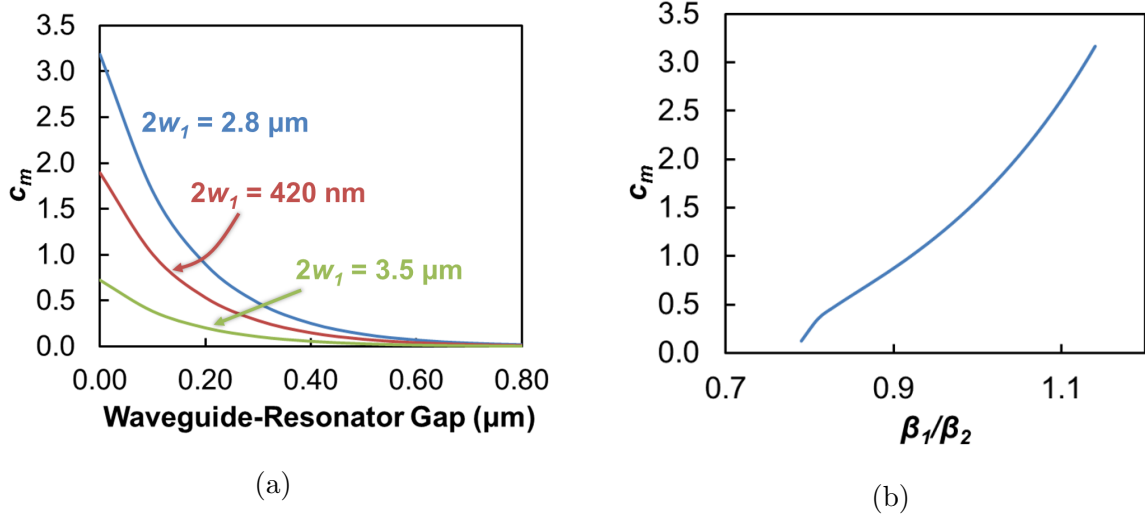


Figure 2.7: Examples of tuning the coupling constant between a 900-nm thick SiO₂ waveguide and microdisk resonator having a 50 μm radius ($\beta_{eq} = 5.14 \mu\text{m}^{-1}$). (a) The coupling constant c_m decreases exponentially as the gap between the waveguide and resonator increases. Here, we graph c_m for waveguides having different widths, and thus different propagation constants β . For $2w_1 = 2.8 \mu\text{m}$, $\beta_1 \approx 5.14 \mu\text{m}^{-1}$, matching the whispering-gallery mode β_{eq} . For $2w_1 = 420 \text{ nm}$, $\beta_1 \approx 4.07 \mu\text{m}^{-1}$. For $2w_1 = 3.5 \mu\text{m}$, $\beta_1 \approx 5.16 \mu\text{m}^{-1}$. (b) Tuning the waveguide's β_1 also changes c_m . Here, we set the waveguide width to $2w_1 = 900 \text{ nm}$, and we vary β_1 with respect to $\beta_2 = \beta_{eq}$.

$$k_{xi} = \sqrt{n_i^2 k_0^2 - \beta_i^2} \quad (2.21a)$$

$$P_i = \frac{\beta_i}{2\omega\mu_0} (w_i + 1/\alpha_i) \quad (2.21b)$$

$$\alpha_i = \sqrt{\beta_i^2 - n_0^2 k_0^2} \quad (2.21c)$$

In the case of a waveguide coupling to a microdisk, the width of “waveguide” 2, which corresponds to the disk, is not immediately obvious. An approximate equivalent waveguide width can be derived from the whispering gallery mode’s equivalent propagation constant β_{eq} . Rowland and Love define this equivalent width as $2w_2 = 2(R - \ell/\beta_{eq})$. [32]

Based on Eq. 2.20, the coupling constant can be tuned with several parameters, including the lateral separation and relative propagation constants. As an example, we graph three instances of the coupling constant with respect to distance in Figure 2.7a. Each instance has a waveguide of a different width, and therefore a different β_1 . This indicates that the coupling constant decays exponentially as the waveguide is moved away from the resonator. As another example, we graph the coupling constant as the propagation in the waveguide is changed in Figure 2.7b. Tuning with this parameter results in a more linear change in c_m .

In a fabricated device, tuning the propagation constant of the waveguide can be accomplished by changing its effective index through some nonlinear optical effect. Previous demonstrations utilized the electro-optic effect [20] and the thermo-optic effect. [38] However,

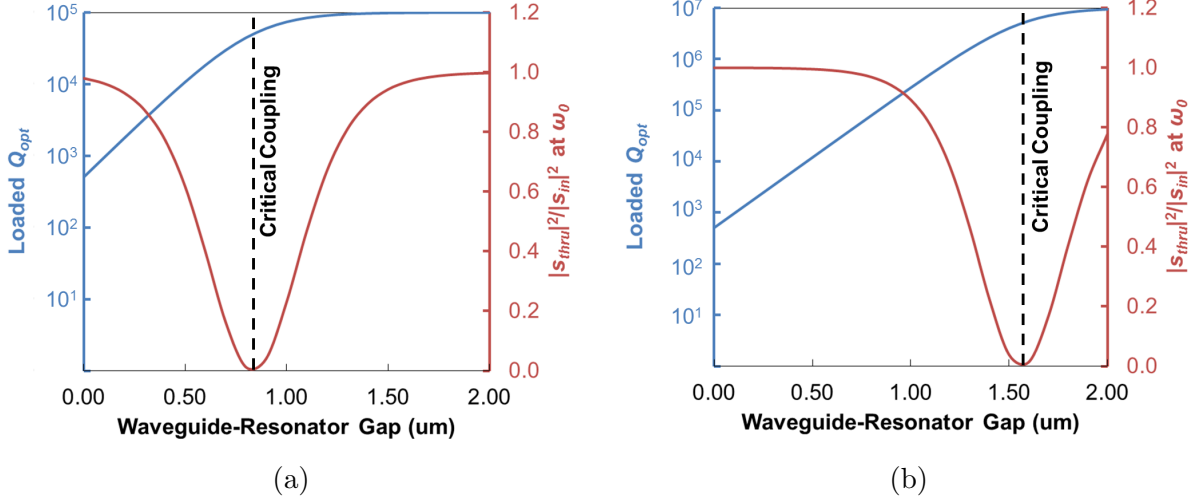


Figure 2.8: Behavior of loaded Q_{opt} and measured power at the optical resonance frequency ω_0 as the gap is changed between a 900-nm thick SiO_2 waveguide having $2w_1 = 2.8 \mu\text{m}$ and microdisk resonator having a $50 \mu\text{m}$ radius. (a) The intrinsic Q_{opt} of the resonator is 10^5 . (b) The intrinsic Q_{opt} of the resonator is 10^7 .

the magnitude of tuning is dependent on the nonlinear optical properties of the material, whereas positional tuning of the coupling constant is not material-dependent. We will be examining positional tuning more in-depth.

Figure 2.8 shows the loaded Q_{opt} (equal to ω_0/κ) with respect to the gap between the waveguide and the resonator. We also graph the normalized power at the through port at the optical resonance frequency ω_0 . These graphs illustrate the coupling regimes discussed in Section 2.2.1. When the waveguide is close to the resonator, it is overcoupled: the loaded Q_{opt} is less than the intrinsic Q_{opt} ($\kappa > 1/\tau_0$), and the power measured at ω_0 is greater than zero. As the waveguide moves away, it passes through critical coupling, where the loaded Q_{opt} is half of the intrinsic Q_{opt} and the measured power at ω_0 is zero. As the waveguide moves even farther away, the loaded Q_{opt} approaches the intrinsic Q_{opt} and the normalized power measured at ω_0 approaches one. Figures 2.8a and 2.8b, we also see that this behavior is modified by the intrinsic Q_{opt} , in that the critical coupling distance is larger for larger Q_{opt} .

This analysis does not include some additional effects that are observed experimentally. One of these, which was mentioned in Section 2.2.1, is the existence of other loss sources in addition to the intrinsic loss of the resonator and the loss of power to the waveguide. These result from non-idealities in the coupling to the waveguide, and cause the critically-coupled power at the through port at ω_0 to be greater than zero. Another effect not mentioned here is the resonance frequency shift due to the presence of the waveguide. When the waveguide is close to the resonator, it slightly raises the effective index of the optical mode. As a result, as the waveguide is moved away, ω_0 decreases, approaching the intrinsic resonant frequency of the cavity.

2.3 Summary/Conclusion

These models of the optical modes in a microdisk and of the coupling behavior of a waveguide to these modes have enabled the design and characterization of a variety of devices that utilize optical microdisk resonators. In this work, we use this theory extensively for measuring the intrinsic Q_{opt} of high- Q resonators by coupling to position-controlled tapered fibers (see Chapter 4), tuning the bandwidth of an optical filter with position-controlled on-chip waveguides (see Chapter 5), and coupling light into and out of optomechanical oscillators (see Chapter 6).

Chapter 3

Cavity Optomechanics in Optical Microring Resonators

It has long been observed that light can impart momentum to objects in the vacuum of space, but optical fields are generally not strong enough exert detectable force on objects in the friction-filled environment of Earth. However, when light is confined in high-quality-factor optical cavities, intensity of the optical field is greatly enhanced, so the radiation pressure can be very large. In addition, the displacement sensitivity of the optical readout of an optical cavity is very high, so even small displacements due to radiation pressure can be detected.

There have been many recent demonstrations of optomechanical interactions using micro-fabricated, high- Q optical resonators. In some, the optical resonator is a separate structure from the mechanical resonator, and the interaction occurs where the mechanical resonator encounters the evanescent field of the optical resonator. [39, 40] In cavity optomechanical systems, the optical and mechanical modes are supported by the same structure. [41, 42] The effect of the optomechanical interaction can vary, as well; the optical field can be used to dampen or amplify a mechanical resonance. In this work, we will focus specifically on cavity optomechanical devices in which we use the optical field to amplify the mechanical resonance.

3.1 Overview of Cavity Optomechanics

For the purposes of gaining a conceptual understanding of a cavity optomechanical system, a good example is a Fabry-Pérot cavity in which one of the mirrors is mechanically compliant, as shown in Figure 3.1a. Initially, the pump laser at frequency ω_p is blue-detuned from the cavity optical resonance ω_0 . The light resonating in the cavity exerts a radiation pressure force on the compliant mirror, and the mirror moves, lengthening the cavity (Figure 3.1b). Changing the length of the cavity also changes the optical resonant frequency of the cavity, so the detuning of the pump laser from the resonance changes. As a result, less light from the pump laser couples into the cavity, and the magnitude of radiation pressure on the mirror decreases. With less force pushing on the mirror, it moves to its original position. Now, the detuning of the pump laser returns to its initial value, and the cycle starts again

(Figure 3.1a).

Just as the mirror's motion is affected by the light in the cavity, the optical field is affected by the motion of the mirror. As the mirror vibrates at radial frequency Ω_m , it acts as a phase modulator of the light in the cavity, scattering some of the light down in frequency by Ω_m and some up by Ω_m . These are called the Stokes and Anti-Stokes sidebands, respectively. The transfer of energy between the optical mode and the mechanical mode can be understood as coming from the energy gained or lost when photons are scattered into these sidebands. When the pump laser is blue-detuned, there are more photons in the lower-frequency Stokes sideband, so optical energy decreases (see Figure 3.2a). This “missing” energy is added to the mechanical mode, resulting in **amplification**. For a red-detuned pump laser, shown in Figure 3.2b, there are more photons in the higher-frequency Anti-Stokes sideband, so the energy in the optical mode increases. This extra energy is drawn from the mechanical mode, **cooling** the mechanical resonance.

The behavior of this Fabry-Pérot (FP) optomechanical system directly corresponds to that of an optical dielectric ring or disk resonator. The disk circumference is the equivalent of the cavity length, and, while this FP's mechanical frequency depends on the mirror mass and its spring's constant, the mechanical frequency of a disk or ring more complex, depending on the device geometry and material properties. The fabricated devices presented in this work are all ring resonators.

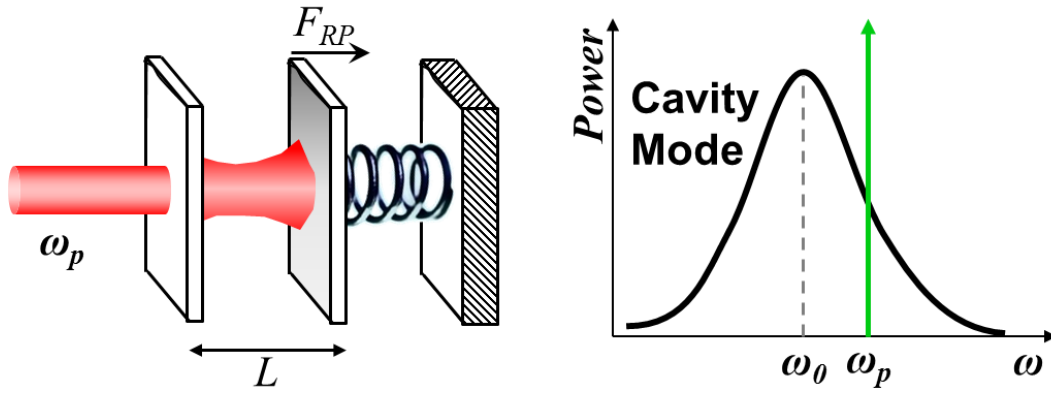
3.2 Solving for Cavity Optomechanical Coupling

We now describe this coupling between the optical and mechanical modes of a radiation-pressure-driven optomechanical resonator mathematically. [43] has developed a small-signal model for this analysis. We start with the coupled equations for the optical field in the cavity $\psi_0(t)$ and mechanical displacement $x(t)$.

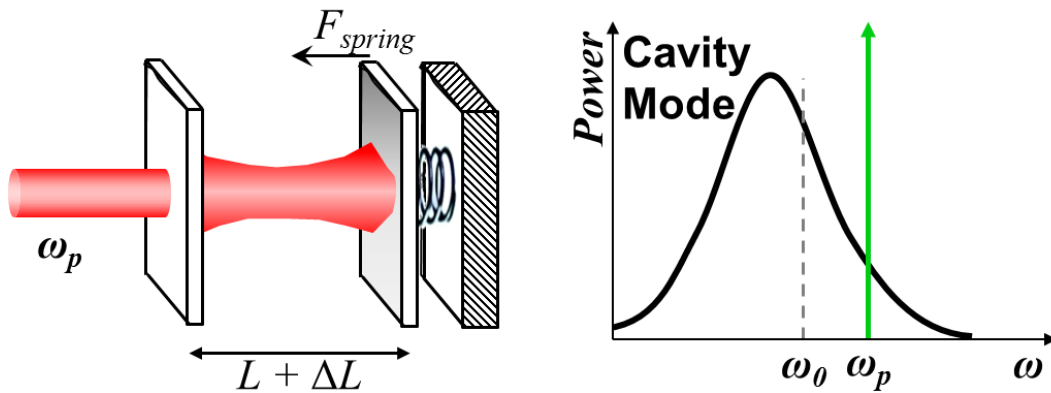
$$\dot{\psi}_0(t) = \left(j(\Delta - g_{om}x(t)) - \frac{\kappa}{2} \right) \psi_0(t) + \frac{s_{in}}{\sqrt{\tau_{ex}}} \quad (3.1a)$$

$$F_{RP}(t)/m_{eff} = \ddot{x}(t) + \Gamma_m \dot{x}(t) + \Omega_m^2 x(t) \quad (3.1b)$$

It is clear that Eq. 3.1a is the equivalent of Eq. 2.10, where τ_{ex} is the external photon lifetime due to a waveguide coupling to it, and assuming constant input power and $\psi(t) = \psi_0(t) \exp(-j\omega t)$ and with the optical detuning $\Delta = \omega - \omega_0$ modified by $g_{om}x(t)$. Here, g_{om} is the optomechanical coupling parameter, which quantifies by how much ω_0 changes per unit displacement. For a ring of radius R that is moving radially, $g_{om} = -\omega_0/R$. Eq. 3.1b is simply the equation of motion for the mechanical resonance, where Γ_m is the mechanical damping, Ω_m is the mechanical resonance frequency, and m_{eff} is the effective mass at that frequency. The effective mass is, essentially, the mass that the device would have if it were a point mass on a spring. For a ring resonator, the mass is instead distributed through the mode shape, so the m_{eff} in a particular mechanical mode will be somewhat different from its physical mass. It can be found for a known mode shape by integrating over that mode shape to determine the potential energy with respect to the displacement parameter x . By setting this equal to the lumped-element potential energy expression $U = k_{eff}x^2/2$, we find the lumped spring



(a)



(b)

Figure 3.1: A Fabry-Pérot optomechanical resonator. One of the mirrors is suspended on a spring, so it is mechanically compliant. (a) The cavity length is initially L , making the optical resonance frequency ω_0 . The pump laser ω_p is, in this case, blue-detuned from the optical resonance. The light in the cavity exerts radiation pressure on the compliant mirror. (b) The compliant mirror moves, increasing the cavity length to $L + \Delta L$. This shifts the cavity mode downward in frequency, reduces the proportion of the pump laser power that couples into the cavity, and decreases the radiation pressure on the mirror.

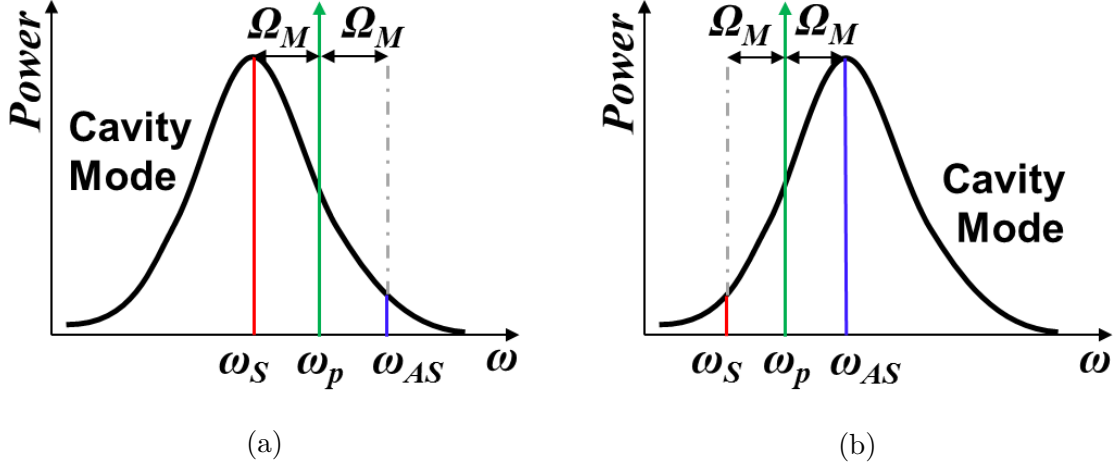


Figure 3.2: Sideband formation due to cavity length modulation. Stokes and Anti-Stokes sidebands form at $-\Omega_m$ and $+\Omega_m$ offsets from the laser frequency ω_p , respectively. (a) For blue detuning, the lower-frequency Stokes sideband has a larger magnitude than the Anti-Stokes sideband. (b) For red detuning, the higher frequency Anti-Stokes sideband has a larger magnitude than the Stokes sideband.

constant k_{eff} . From there, we obtain the effective mass, knowing $\Omega_m = \sqrt{k_{eff}/m_{eff}}$. [44] The effective mass can also be extracted using finite element modeling.

The driving force for the equation of motion in Eq. 3.1b is $F_{RP}(t)$, the force due to radiation pressure, and it is proportional to the optical power in the cavity divided by the photon group velocity. In a dielectric microdisk resonator, this can be expressed as [45]:

$$F_{RP}(t) \approx \frac{2\pi n_{eff}}{c} \frac{\hbar\omega|\psi_0(t)|^2}{2\pi R n_{eff}/c} = -\hbar g_{om}|\psi_0(t)|^2 \quad (3.2)$$

where $|\psi_0|^2$ is normalized to the number of photons. (With this normalization, it follows that $|s_{in}|^2$ is the number of photons entering the coupling region per second.) Now we see that Eq. 3.1a and 3.1b are coupled through radiation pressure by the fact that a change in cavity field results in a displacement and vice versa. If we assume a steady state, we find the following values for displacement $x(t) = x_0$ and cavity field $\psi_0(t) = \psi_0$:

$$\psi_0 = \frac{1}{\kappa/2 - j(\Delta - g_{om}x_0)} \frac{s_{in}}{\sqrt{\tau_{ex}}} \quad (3.3a)$$

$$x_0 = \frac{-\hbar g_{om}|\psi_0|^2}{m_{eff}\Omega_m^2} \quad (3.3b)$$

Again, we note that Eq. 3.3 is the equivalent of Eq. 2.11 with the effective detuning modified by g_0x_0 . For a solution that is not steady state, we assume the deviation from the steady-state solution is small:

$$\psi_0(t) = \psi_0 + \delta\psi(t) \quad (3.4a)$$

$$x(t) = x_0 + \delta x(t) \quad (3.4b)$$

$$F_{RP}(t) = -\hbar g_{om} |\psi_0|^2 + \delta F(t) \quad (3.4c)$$

By substituting these and Eq. 3.3 into Eq. 3.1 and taking into account that $\delta\psi \ll \psi_0$ and $\delta x \ll x_0$, we obtain the following small-signal coupled equations:

$$\delta\dot{\psi}(t) = \left(j(\Delta - g_{om}x_0) - \frac{\kappa}{2} \right) \delta\psi(t) - jg_{om}\psi_0\delta x(t) \quad (3.5a)$$

$$\ddot{\delta x}(t) + \Gamma_m \dot{\delta x}(t) + \Omega_m^2 \delta x(t) = (-\hbar g_{om}\psi_0(\delta\psi(t) + \delta\psi^*(t)) + \delta F(t)) / m_{eff} \quad (3.5b)$$

To solve these differential equations, we transform these equations and their complex conjugates to the frequency domain, where $f(\Omega) = \int_{-\infty}^{\infty} f(t) \exp(j\Omega t) dt$:

$$-j\Omega \delta\psi(\Omega) = \left(j(\Delta - g_{om}x_0) - \frac{\kappa}{2} \right) \delta\psi(\Omega) - jg_{om}\psi_0\delta x(\Omega) \quad (3.6a)$$

$$-j\Omega \delta\psi^*(\Omega) = \left(-j(\Delta - g_{om}x_0) - \frac{\kappa}{2} \right) \delta\psi^*(\Omega) + jg_{om}\psi_0\delta x(\Omega) \quad (3.6b)$$

$$\delta x(\Omega) (-\Omega^2 - j\Omega\Gamma_m + \Omega_m^2) = (-\hbar g_{om}\psi_0(\delta\psi(\Omega) + \delta\psi^*(\Omega)) + \delta F(\Omega)) / m_{eff} \quad (3.6c)$$

Solving Eq. 3.6a and 3.6b for $\delta\psi(t)$ and $\delta\psi^*(t)$, we find two solutions for the small signal field:

$$\delta\psi(\Omega) = \frac{-jg_{om}\psi_0\delta x(\Omega)}{\kappa/2 - j(\Omega + \Delta - g_{om}x_0)} \quad (3.7a)$$

$$\delta\psi^*(\Omega) = \frac{jg_{om}\psi_0\delta x(\Omega)}{\kappa/2 - j(\Omega - \Delta + g_{om}x_0)} \quad (3.7b)$$

These correspond to the Stokes- and Anti-Stokes sidebands on the optical signal (Figure 3.3), which form in the same way that a phase modulator produces upper and lower sidebands offset from the optical signal by the modulation frequency. The magnitude of these sidebands is shaped by the optical mode, a Lorentzian of linewidth κ , so one of them is larger than the other, depending on Δ . Knowing the magnitude of these sidebands, we can substitute them into Eq. 3.6c to find the small-signal equation of motion with respect to detuning and ψ_0 :

$$\begin{aligned} \frac{\delta F(\Omega)}{m_{eff}\delta x(\Omega)} = & -\Omega^2 - j\Omega\Gamma_m \\ & - j\Omega \left(\frac{\hbar g_{om}^2 \psi_0^2}{m_{eff}\Omega} \left(\frac{\kappa/2}{\kappa^2/4 + (\Omega + \Delta - g_{om}x_0)^2} - \frac{\kappa/2}{\kappa^2/4 + (\Omega - \Delta + g_{om}x_0)^2} \right) \right) \\ & + \Omega_m^2 + \frac{\hbar g_{om}^2 \psi_0^2}{m_{eff}} \left(\frac{\Omega + \Delta - g_{om}x_0}{\kappa^2/4 + (\Omega + \Delta - g_{om}x_0)^2} - \frac{\Omega - \Delta + g_{om}x_0}{\kappa^2/4 + (\Omega - \Delta + g_{om}x_0)^2} \right) \end{aligned} \quad (3.8)$$

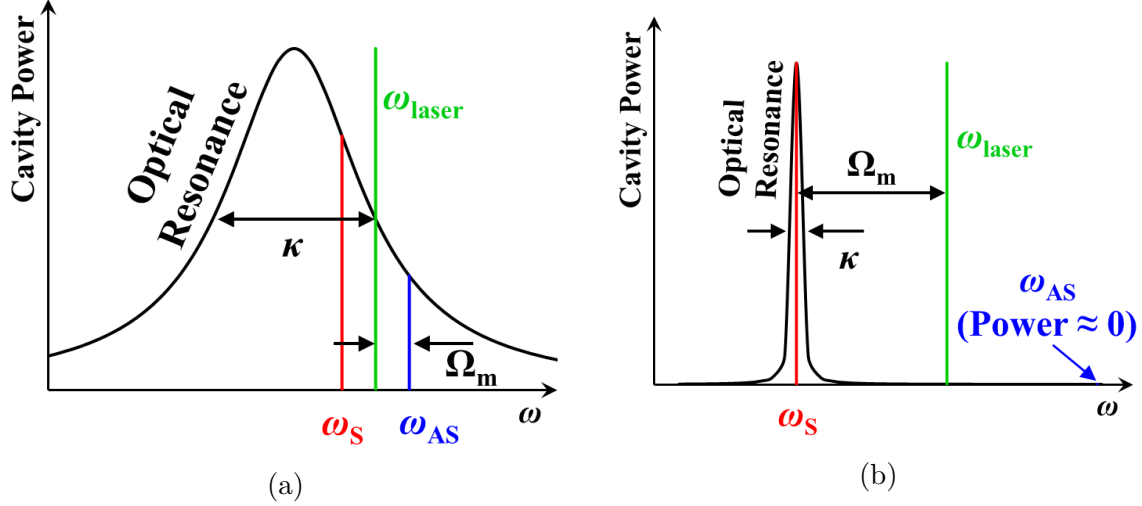


Figure 3.3: Spectra for non-sideband resolved and sideband-resolved optomechanical resonances, with the laser blue-detuned from the optical resonance. The Stokes and Anti-Stokes sidebands form above and below the pump laser wavelength, spaced by Ω_m . (a) In the non-sideband resolved regime, the optical resonance width is much greater than the mechanical frequency Ω_m . Both of the sidebands can fit within the optical resonance. (b) In the sideband-resolved regime, the mechanical frequency Ω_m is much larger than the optical linewidth, and the sidebands are too widely spaced to both fit within the optical resonance. As a result, in the case of blue-detuning, the Anti-Stokes sideband goes to zero.

Looking at the imaginary and real terms of the equation of motion, we see that there is now an effective damping and spring constant resulting from the optomechanical coupling. Defining an effective detuning from the steady-state optical resonance $\Delta_{\text{eff}} = \Delta - g_{om}x_0$, at the mechanical resonance frequency these are:

$$\Gamma_{\text{eff}} = \Gamma_m + \Gamma_{om} = \Gamma_m + \frac{\hbar g_{om}^2 \psi_0^2}{m_{\text{eff}} \Omega_m} \left(\frac{\kappa/2}{\kappa^2/4 + (\Omega_m + \Delta_{\text{eff}})^2} - \frac{\kappa/2}{\kappa^2/4 + (\Omega_m - \Delta_{\text{eff}})^2} \right) \quad (3.9a)$$

$$k_{\text{eff}} = m_{\text{eff}} \Omega_m^2 + k_{om} = k_m + \hbar g_{om}^2 \psi_0^2 \left(\frac{\Omega_m + \Delta_{\text{eff}}}{\kappa^2/4 + (\Omega_m + \Delta_{\text{eff}})^2} - \frac{\Omega_m - \Delta_{\text{eff}}}{\kappa^2/4 + (\Omega_m - \Delta_{\text{eff}})^2} \right) \quad (3.9b)$$

These new parameters are dependent on the optical field in the cavity, the effective input laser detuning Δ_{eff} , and the optical linewidth $\kappa = \tau_0^{-1} + \tau_{\text{ex}}^{-1}$. (As discussed in 2.2.1, $c_m = \tau_{\text{rt}}/\tau_{\text{ex}}$ is an expression of the coupling between a waveguide and an optical resonator, and τ_0 is the intrinsic photon lifetime of the resonator) As for detuning, it is straightforward to see that when $\Delta_{\text{eff}} = 0$, Γ_{om} and k_{om} are both zero, so there is no measurable optomechanical coupling effect. However, when $\Delta_{\text{eff}} < 0$ (red-detuned), $\Gamma_{om} > 0$. Because the optomechanical coupling adds to the damping, we call this the “cooling” regime. Finally, when $\Delta_{\text{eff}} > 0$ (blue-detuned), $\Gamma_{om} < 0$. Because the optomechanical coupling subtracts from the intrinsic mechanical damping, we call this the “amplification” regime.

We can further divide up the regimes into “non-sideband-resolved” and “sideband-resolved.” In the non-sideband-resolved regime, the photon lifetime is much less than the the time of

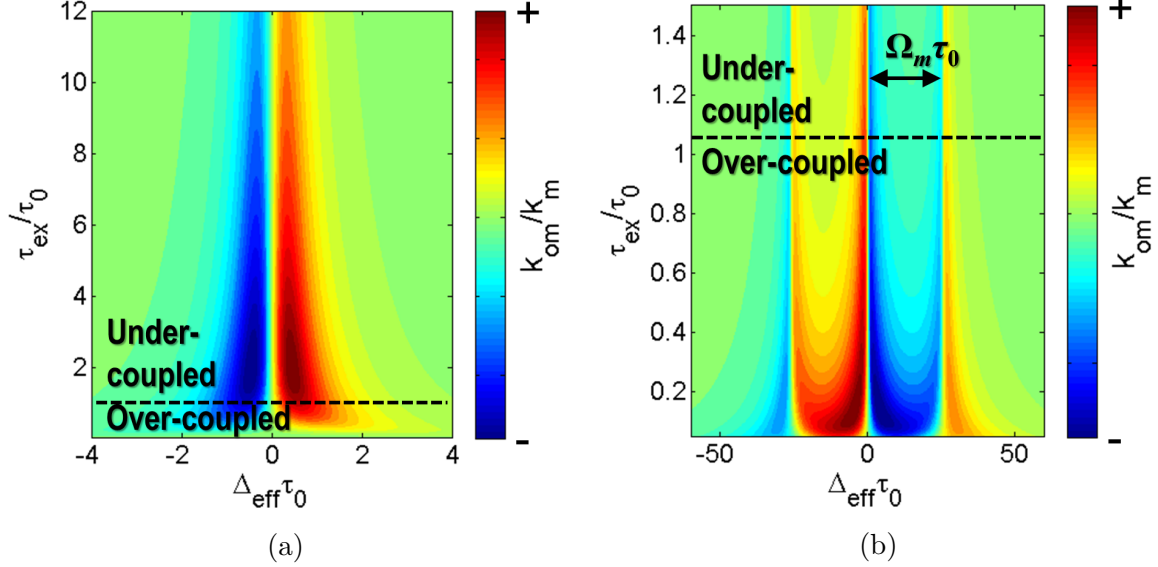


Figure 3.4: Contour plots of the relative optical stiffness k_{om}/k_m with respect to the relative external photon lifetime τ_{ex}/τ_0 and the relative effective detuning $\Delta_{eff}\tau_0$. From left to right on the graphs, detuning goes from the red to blue regimes, and from bottom to top, the coupling changes from over- to under-coupled. (a) An example of a non-sideband-resolved device having mechanical frequency $\Omega_m = 20 \text{ MHz} \times 2\pi$ and $\tau_0^{-1} = 190 \text{ MHz} \times 2\pi$. (b) An example of a sideband-resolved device having mechanical frequency $\Omega_m = 500 \text{ MHz} \times 2\pi$ and $\tau_0^{-1} = 19 \text{ MHz} \times 2\pi$.

one mechanical oscillation ($\kappa \gg \Omega_m$), whereas in the sideband-resolved regime, the photon lifetime is much greater than the time of one mechanical oscillation ($\kappa \ll \Omega_m$). These regimes can also be described graphically, as shown in Figure 3.3. Our devices generally fell into the non-sideband-resolved regime, and we focused on their behavior with the input optical field blue-detuned.

To better understand the dependence of Γ_{eff} and k_{eff} on the optical parameters Δ_{eff} and τ_{ex} , we constructed several graphs in both the non-sideband-resolved and sideband resolved-regimes. In Figure 3.4, we graph the optical stiffness as a function of coupling and effective detuning. For the non-sideband-resolved device, $k_{om} < 0$ when the input optical signal is red-detuned, and $k_{om} > 0$ for blue detuning. This means that red detuning will result in a decreased effective mechanical frequency, while blue detuning will increase the effective mechanical frequency. The magnitude of k_{om} is greatest when undercoupled with $\Delta_{eff}\tau_0 \approx 0.5$.

A more complex picture emerges from the sideband-resolved analysis. Here, there appear to be four different regimes with respect to detuning. When $|\Delta_{eff}| < \Omega_m$, the optical stiffness is positive for red detuning and negative for blue detuning, the opposite of the general detuning dependence for the non-sideband-resolved example. Then, for $|\Delta_{eff}| > \Omega_m$, the sign flips, such that $k_{om} < 0$ for red detuning and $k_{om} > 0$ for blue detuning. The largest magnitude optical stiffness is achieved in the over-coupled regime, where $|\Delta_{eff}| \ll \Omega_m$.

We also calculate the optomechanical damping as a function of coupling and effective detuning, shown in Figure 3.5. In the non-sideband resolved example, we see that the

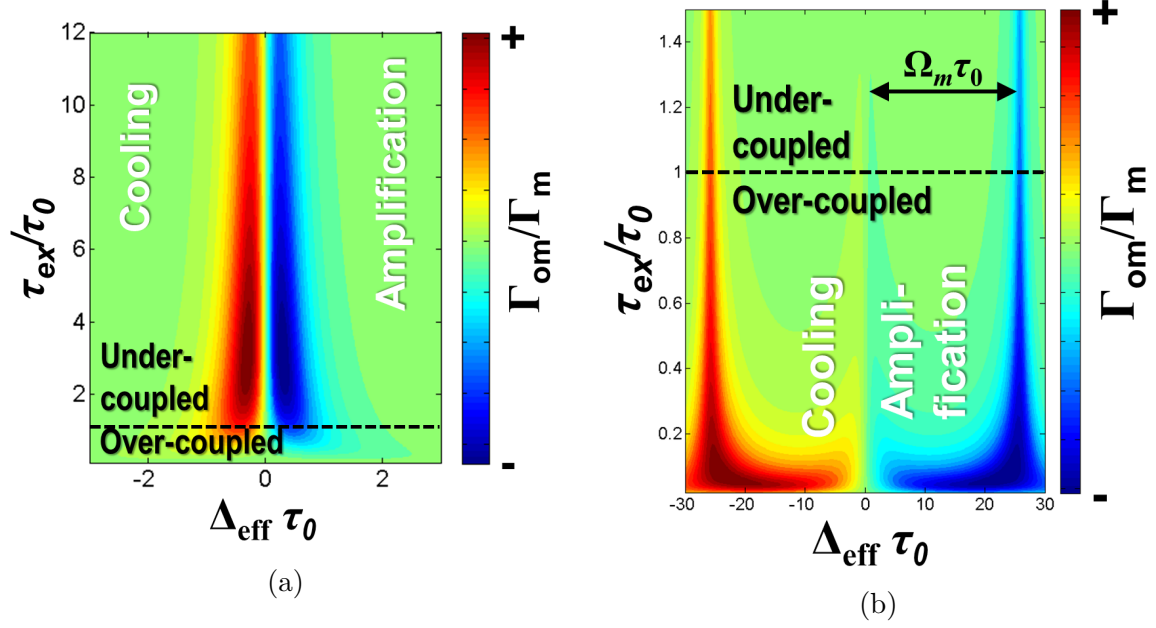


Figure 3.5: Contour plots of the relative optomechanical damping Γ_{om}/Γ_m with respect to the relative external photon lifetime τ_{ex}/τ_0 and the relative effective detuning $\Delta_{eff}\tau_0$. From left to right on the graphs, detuning goes from the cooling to amplification regimes, and from bottom to top, the coupling changes from over- to under-coupled. (a) An example of a non-sideband-resolved device having mechanical frequency $\Omega_m = 20 \text{ MHz} \times 2\pi$ and $\tau_0^{-1} = 190 \text{ MHz} \times 2\pi$. (b) An example of a sideband-resolved device having mechanical frequency $\Omega_m = 500 \text{ MHz} \times 2\pi$ and $\tau_0^{-1} = 19 \text{ MHz} \times 2\pi$.

largest magnitude of optomechanical damping occurs when undercoupled and detuned by about half the optical linewidth, which are the same conditions under which the maximum k_{om} occurred in the non-sideband-resolved analysis. Alternatively, in the sideband-resolved example, we see that the effect of optomechanical coupling on mechanical damping is largest for detuning around Ω_m in the overcoupled regime.

The negative optomechanical damping accessible when blue-detuned leads to some interesting mechanical behavior. Under certain conditions, Γ_{om} can completely cancel out the intrinsic mechanical loss Γ_m , leading to regenerative oscillations. The power at which this occurs is known as the threshold power P_{th} . We find an expression for P_{th} by setting Γ_{eff} from Eq. 3.9a equal to zero and solving for $P_{in} \approx \hbar\omega_0|s_{in}|^2$. The threshold power is thus

$$P_{th} = \Gamma_m \frac{m_{eff}\Omega_m\tau_{ex}\omega_0}{g_{om}^2} (\kappa^2/4 + \Delta_{eff}^2) \left(\frac{\kappa/2}{\kappa^2/4 + (\Omega_m - \Delta_{eff})^2} - \frac{\kappa/2}{\kappa^2/4 + (\Omega_m + \Delta_{eff})^2} \right)^{-1} \quad (3.10)$$

If we assume critical coupling ($\tau_{ex} = \tau_0$), we can further simplify this expression and put it in terms of the intrinsic $Q_{mech} = \Omega_m/\Gamma_m$ and the intrinsic $Q_{opt} = \omega_0\tau_0$. In the limits of non-sideband-resolved ($\kappa \gg \Omega_m$), we set the detuning to $(2\tau_0)^{-1}$, which corresponds to the optimal coupling indicated by Figure 3.5a. For the sideband-resolved regime ($\kappa \ll \Omega_m$), we choose the optimal detuning $\Delta_{eff} = \Omega_m$, as indicated by Figure 3.5b. With these substitutions, we obtain the following expressions:

$$P_{th} \approx \frac{5^3}{2^7} \frac{\Omega_m}{Q_{mech}} \frac{m_{eff}\omega_0^4}{g_{om}^2} \frac{1}{Q_{opt}^3} \quad (\text{non-sideband-resolved}) \quad (3.11a)$$

$$P_{th} \approx \frac{m_{eff}\Omega_m^4\omega_0}{g_{om}^2 Q_{mech}} \quad (\text{sideband-resolved}) \quad (3.11b)$$

From these expressions, we can get a good idea of the dominant parameters contributing to P_{th} . For both regimes, the optomechanical coupling parameter is inverse-quadratically related to the threshold power, so an increase in g_{om} will greatly reduce P_{th} . Also, for the non-sideband-resolved regime, P_{th} is strongly dependent on the intrinsic optical quality factor Q_{opt} . This makes sense intuitively because a higher Q_{opt} means a larger difference in magnitude between the Stokes and Anti-Stokes sidebands (Figure 3.3), so more energy is transferred to the mechanical mode. At the same time, P_{th} is independent of Q_{opt} in the sideband-resolved regime, which again makes sense, as the Anti-Stokes sideband, removed from the optical resonance by $2\Omega_m$ will be zero regardless of Q_{opt} , so the power transferred to the mechanical mode will depend only on the magnitude of the Stokes sideband.

We can experimentally observe P_{th} from the optical signal at the coupling waveguide's through port. The mechanical vibration manifests as modulation of the optical signal at Ω_m , and the linewidth of the modulation peak is approximately the effective damping Γ_{eff} . The maximum power in the detected modulation resonance is proportional to the mechanical modulation amplitude δx . Thus, at low powers (and thus small $|\Gamma_{om}|$), the resonance spectrum will simply be a result of the laser sampling the Brownian motion of the resonator. From this we can extract the intrinsic mechanical properties of the resonator. As the input power increases, the modulation peak will become narrower and grow in magnitude. Above threshold, due to other noise mechanisms in the system not taken into account by this analysis, the peak width will not go to zero while becoming infinitely tall, but we will see the modulation magnitude increase at a much faster rate with respect to P_{in} when it goes above P_{th} . This manifests as a "kink" at P_{th} in a graph of the resonance magnitude with respect to the input power. [45]

As we continue to increase the input power above P_{th} , some other effects become apparent in the output optical signal. One of these is the formation of optomechanical frequency combs. As we described previously, light circulating within the cavity is modulated at Ω_m . A fraction of this modulated light in the cavity will be modulated again, producing modulation sidebands at $2\Omega_m$ and zero. The upper sideband, when further modulated, results in sidebands at $3\Omega_m$ and back at Ω_m . Thus, we detect a frequency comb at the output, with Ω_m spacing between each harmonic, and the power in each harmonic dropping off with increasing frequency.

3.3 Other Effects that Depend on Cavity Power

There are other optical nonlinearities that can contribute to coupling between the optical resonance and displacement. Some of the more significant of these effects are intensity-dependent refractive index (also called the Kerr effect), thermal expansion, the thermo-optic

Table 3.1: Material parameters pertinent to the Kerr effect and thermal effects

	SiO ₂	Si ₃ N ₄	Si
Kerr Coefficient (m ² /W)	3×10^{-20} [43]	2.4×10^{-19} [46]	4×10^{-18} [47]
Approx. Kerr Response Time (fs)	0.08	0.2	2
Coeff. of Thermal Expansion (ppm/K)	0.5	3	2.6
dn/dt (ppm/K)	~ 10 [48]	~ 10 [48]	190 [49]
Thermal Conductivity (W/(m K))	1.4	30	150
Heat Capacity (J/(kg K))	730	710	700
Approx. Thermal Time Constant (μ s)*	0.1	16	12

*Calculated for a resonator having 15 μ m outer radius, 11 μ m inner radius, 1 μ m thickness, 2 μ m anchor length, and 64 μ m² anchor cross section. The anchor for the SiO₂ device is made of Si, and the anchors for Si₃N₄ and Si devices are made of SiO₂.

effect, and the photo-elastic effect. Some material parameters relevant to these effects are shown in Table 3.1.

3.3.1 The Kerr Effect in Optomechanical Resonators

For the Kerr effect, a material's refractive index is $n(I) = n + n_2 I$, where n is the initial refractive index, I is the intensity, and n_2 is the Kerr coefficient. By referring to the expression for power circulating in the cavity given by Eq. 2.11, we obtain a first-order expression for the optical resonance with respect to the field circulating in the resonator, where A_{eff} is the effective cross-sectional area of the optical mode.

$$\omega_0(\psi_0(t)) = \omega_0 \left(1 - \frac{n_2}{n} \frac{|\psi_0(t)|^2}{\tau_{rt} A_{eff}} \right) \quad (3.12)$$

Thus, we can see that, if the field in the resonator changes, the detuning changes. We express this as a perturbation on the detuning $\Delta(t) = \Delta_0 + \delta\Delta(t)$. Substituting this into Eq. 3.1a, we find a new small-signal equation for the optical field:

$$\dot{\delta\psi}(t) = \left(j\Delta_{eff} - \frac{\kappa}{2} \right) \delta\psi(t) - j(g_{om}\delta x(t) - \delta\Delta(t)) \psi_0 \quad (3.13)$$

This indicates that the change in detuning due to the Kerr effect acts as an addition to the optomechanical coupling. It is also important to note that the response time is on the order of $|\omega_0 - E_g/\hbar|^{-1}$, where E_g is the material band gap. [50] This is very fast (see Table 3.1), so it will be able to respond to the mechanical oscillation of a typical microring ($\Omega_m < 1$ GHz). However, the magnitude is small compared to optomechanical coupling. For example, for a typical silicon microring with outer radius of 15 μ m, inner radius of 11 μ m, and thickness 1 μ m, at critical coupling and $\Delta_{eff} = (2\tau_0)^{-1}$, the relative detuning shift caused by the Kerr effect $\delta\Delta/(1/\tau_0)$ is around 20 ppb for an input power equal to the P_{th} from Eq. 3.11a. In order for this to be on the order of $g_{om}\delta x$, δx would have to be about 20 am. This is an unrealistically small value at P_{th} , since the thermal δx alone at room temperature is about 0.1 pm (thermal $\delta x = \sqrt{2k_B T / (m_{eff} \Omega_m^2)}$).

3.3.2 Thermal Effects in Optomechanical Resonators

The thermal effects, thermal expansion and temperature-dependent refractive index (thermo-optic effect), occur when the circulating light absorbed in the resonator is converted to heat, thus raising the temperature of the resonator. Because the response time for these processes is dependent on the amount of time it takes to heat and cool the entire resonator, they are not nearly as fast as the Kerr effect. We can estimate the thermal time constant τ_T from the known material parameters and device dimensions by determining the thermal capacitance of the resonator and thermal resistance of the resonator's anchors to the substrate:

$$\tau_T = R_T C_T \quad (3.14a)$$

$$R_T = L/(\kappa_T A_{\text{anchor}}) \quad (3.14b)$$

$$C_T = m c_p \quad (3.14c)$$

Here, L is the length of the anchor, κ_T is the thermal conductivity of the anchor, A_{anchor} is the cross-sectional area of the anchor, m is the resonator mass, and c_p is the heat capacity of the resonator. Table 3.1 shows the approximate τ_T for a microring resonator with 15 μm outer radius, 11 μm inner radius, 1 μm thickness, 2 μm anchor length, and 64 μm^2 anchor cross section. This is calculated for four different device materials. In each case, τ_T is at least 0.1 μs , which is too long to respond to the mechanical oscillation of a typical microring ($\Omega_m > 10$ MHz). Thus, these thermal effects will only affect the optomechanical resonator's steady-state behavior.

Thermal expansion is described by $L(\delta T) = L_0(1 + \alpha_L \delta T)$, where α_L is the linear coefficient of thermal expansion. This increases the resonator's radius with increasing temperature, thereby changing the optical resonance frequency. The thermo-optic effect is a change in refractive index with respect to temperature described by $n(\delta T) = n + \delta T \left(\frac{dn}{dT} \right)$. By taking both of these effects into account, the first-order expression for ω_0 is as follows:

$$\omega_0(\delta T) = \omega_0 \left(1 - \left(\alpha_L + \frac{1}{n_{\text{eff}}} \frac{dn}{dT} \right) \delta T \right) \quad (3.15)$$

From this we can infer what would occur as a tunable laser is scanned across an optical resonance, as shown in Figure 3.6. [51] As the laser approaches the resonance from $\omega > \omega_0$, more light is coupled into the resonator, raising its temperature and decreasing the resonant frequency. Continuing to scan the laser downward, even more light enters the resonator, and ω_0 continues to decrease. The laser frequency "chases" the temperature-dependent ω_0 until it actually goes below it, at which point less light is coupling into the resonator, and the temperature drops. This causes ω_0 to jump back to its original value. Although this process does not directly affect the optomechanical oscillations, it is important to consider during experimentation. For example, when measuring the optical quality factor with a laser scan, P_{in} must be kept small to minimize heating of the resonator, which distorts the resonance shape. Also, the effective detuning is difficult to exactly determine during blue-detuned optomechanical oscillation measurements, since the optical resonant frequency will shift as the absolute laser frequency is changed.

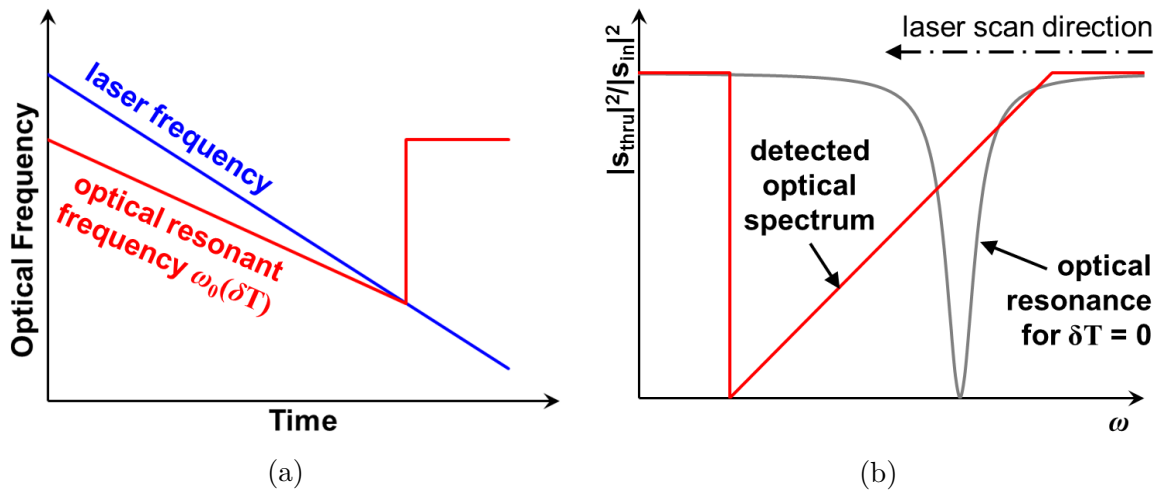


Figure 3.6: Graphs of thermally-induced behavior of an optical resonator as it is interrogated by a tunable laser swept with decreasing frequency, starting blue-detuned from the intrinsic resonance. (a) The optical resonance ω_0 decreases as the laser is swept toward ω_0 , since the optical power coupling into the cavity is increasing, thereby increasing temperature. When the laser frequency drops below the temperature-shifted resonance, the power in the cavity drops, as does the temperature. Consequently, ω_0 returns to its original, intrinsic value. (b) This thermal effect is manifest in the optical spectrum measured at the coupling waveguide's through port. Instead of detecting a Lorentzian lineshape around ω_0 , the resonance shape is distorted. Lowering the optical input power reduces this distortion.

3.3.3 Photoelastic Effects in Optomechanical Resonators

Photoelastic effects are the result of strain-dependent refractive index of a material. The magnitude and direction is described by a photoelastic tensor. Depending on the device material and geometry, and the optical polarization, the magnitude and direction of the resulting electrostrictive forces can vary widely. [52] As of yet, there has been little investigation of how photoelasticity might affect optomechanical devices. However, [52] has studied the effects of both radiation pressure and photoelastic effects in silicon waveguides, and has found that these forces add constructively and can be of the same order of magnitude. Thus, it is possible that, in silicon optomechanical microdisk resonators, electrostrictive forces could add to the radiation pressure force, thereby reducing the effective P_{th} .

3.4 Phase Noise in Cavity Optomechanical Oscillators

When an optomechanical resonator is operating in the amplification regime with $P_{in} > P_{th}$, it is an oscillator, where the mechanical resonance is amplified by the optical field, which is in turn modulated by the mechanical resonance. Thus, the gain in this system is from the optical resonance, and the frequency-selective component is from the mechanical resonance. One of the most important performance metrics of an oscillator is its stability, and one way to quantify this is by measuring the power spectral density of the phase with respect to offset from the carrier frequency Ω_m .

In an ideal oscillator, the power spectral density would be a delta function at Ω_m , but noise in the real world broadens this resonance. This broadening is characterized by normalizing the power at an offset from the carrier frequency by the power in the carrier, and the resultant plot is known as the phase noise spectrum. The shape of the phase noise spectrum indicates the kinds of noise affecting the system. The inherent variations of the oscillator itself contribute to the phase noise, with the magnitude proportional to $1/f^2$, where $f = \Omega/(2\pi)$. The white phase noise “floor” comes from any laser noise or intrinsic Brownian fluctuations in the system. Additional noise detected at low offsets from the carrier is indicative of slow noise processes, such as environmental vibration. The spectrum in dB of all this noise is described by Leeson’s equation [53]:

$$\mathfrak{L}(f_{oc}) = S(f_{oc}) \left(1 + \left(\frac{f_m}{2Q_{mech}f_{oc}} \right)^2 \right) \quad (3.16a)$$

$$S(f_{oc}) = \frac{\zeta}{f_{oc}} + \frac{2Fk_B T}{P_{sig}} \quad (3.16b)$$

Here, f_{oc} is the frequency offset from the carrier frequency $f_m = \Omega_m/(2\pi)$, ζ is a constant indicating the magnitude of additional $1/f$ noise, F is the effective noise factor, and P_{sig} is the carrier power. An example of a phase noise spectrum of this form is graphed in Figure 3.7. The variations in slope indicate what kind of noise dominates at varying offset from the carrier.

This phase noise is, directly, noise in the displacement of the optomechanical resonator, but we detect it indirectly in the modulation at Ω_m of the optical signal coupling out of the

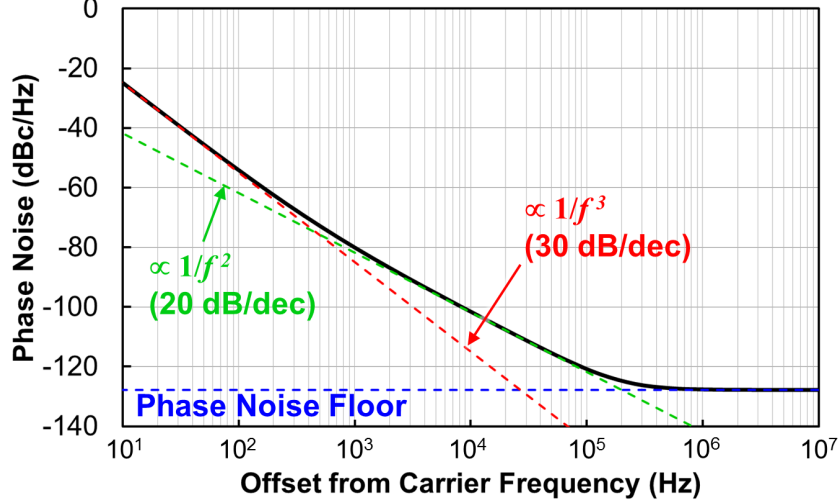


Figure 3.7: The Leeson model for phase noise in an oscillator indicates different noise sources and how they affect the shape of the noise spectrum with respect to the offset from the carrier frequency. In this example, the close-to-carrier slope is 30 dB/decade, indicating some additional $1/f$ noise source, such as vibration. Far from carrier, the noise is white, and the magnitude is set by sources such as thermal fluctuations and laser noise. The $1/f^2$ component comes from variations within the oscillator itself.

resonator. From Eq. 3.16, we see that increasing both Q_{mech} and P_{sig} improves the phase noise. The mechanical quality factor is especially important, as the phase noise is dependent on $1/Q_{mech}^2$. We can increase Q_{mech} with careful device design as well as measurement in low ambient pressure, which reduces the mechanical dissipation due to air. P_{sig} in an optomechanical oscillator is dependent on a variety of parameters due to the optomechanical coupling, including detuning Δ_{eff} , input power, photon lifetime due to coupling to a waveguide (τ_{ex}), optical quality factor Q_{opt} , and the optomechanical coupling parameter g_{om} . [7, 54] Counter-intuitively, an increase in Q_{opt} can lead to a reduction in P_{sig} , because the higher-order optomechanical frequency combs, described in Section 3.2, are filtered out by the narrow optical cavity linewidth, preventing them from scattering light back into the optical carrier mode. [54] However, if Q_{opt} is low, the threshold power for regenerative oscillations will be very high (see Eq. 3.11). Thus, a low-phase-noise optomechanical oscillator must have a high Q_{mech} and a Q_{opt} that is just high enough to achieve regenerative oscillations.

3.5 Summary

The small-signal model for optomechanical coupling presented in this chapter shows the optical field of a mechanically-compliant optical resonator influences the mechanical displacement, and vice versa. We are especially focused on optomechanical behavior when the pump laser is blue-detuned, in which case energy from the optical field is transferred to the motion of the resonator. In this regime, regenerative oscillations, where the gain from the optical field cancels the intrinsic mechanical loss, can occur with enough input power.

This analysis indicates that the threshold power for these oscillations in the non-sideband resolved regime is strongly dependent on the optical quality factor but also depends on the mechanical quality factor and the mechanical and optical resonance frequencies. In Chapter 6 of this work, we will focus on the behavior of optomechanical oscillators with the goal of minimizing phase noise so that such an oscillator could be a stable source for an on-chip, all-optical reference. The phase noise analysis described in this chapter shows that the mechanical quality factor is especially important for achieving this goal.

Chapter 4

Achieving High Optical Q in Integrated Silica Devices

4.1 Factors Affecting Optical Q

As discussed in Chapters 2 and 3, optical quality factor (Q_{opt}) is a key parameter of whispering gallery mode resonators. In optical filters, the minimum achievable bandwidth is limited by the intrinsic Q_{opt} of the resonator. In cavity optomechanical systems, the threshold power for self-oscillation is proportional to the inverse of $(Q_{opt})^3$. In both of these applications, high Q_{opt} can contribute to better performance.

Achieving high optical Q requires minimizing the loss mechanisms in the resonator. The major loss mechanisms affecting Q_{opt} are intrinsic material absorption, nonlinear optical processes, bending loss, and material defects. Material absorption can obviously be minimized by choosing an appropriate optical material. Table 4.1 compares the absorption coefficients of some common microprocessing materials. It is clear that SiO_2 has orders of magnitude lower optical absorption at 1550nm than Si and Si_3N_4 . Additionally, although the absorption coefficient given for lightly-doped Si is quite low, it is very difficult to procure Si of this purity ($2 \times 10^{12} \text{ cm}^{-3}$) in a typical microprocessing environment. [55] As a result, doping in typical Si photonic devices will be higher, and the free carrier absorption will significantly contribute to the material loss in Si resonators.

Table 4.1: Important optical parameters of common microprocessing materials around $\lambda=1550\text{nm}$

	Absorption	Absorption-Limited Q_{opt}	n
Lightly-Doped Si	0.264 dB/m [55]	5.34×10^8	3.48 [55]
Typically-Doped Si	0.496 dB/m*	2.84×10^8	3.48
Si_3N_4	0.055 dB/cm [56]	1.5×10^7	2.00
SiO_2	0.154 dB/km [57]	3.82×10^{11}	1.45

*Theoretical calculation for $\rho = 13 \text{ } \Omega\cdot\text{cm}$ based on [58]

Nonlinear optical processes can also be minimized by material choice. The most significant of these processes to consider for the materials shown in Table 4.1 is two-photon absorption. Because the band gap of Si is 1.11 eV, two-photon absorption plays a big role at wavelengths around 1550 nm (0.8 eV). [59] In addition, the two-photon absorption generates free carriers, which further contribute to the optical loss. As a result, Q_{opt} will effectively decrease as the optical power in the Si cavity increases. However, the band gaps of SiO₂ and Si₃N₄ are much larger, 9 eV and 5 eV, respectively, so two-photon absorption is not a significant effect at infrared wavelengths in these materials.

We can minimize the effect of bending loss in optical whispering gallery mode resonators by choosing a device radius large enough that bending is not the dominant loss mechanism. Although this is not specifically a loss mechanism intrinsic to the material choice, it is important to note that materials with higher indices of refraction can tolerate smaller bending radii. Thus, Si resonators can have much smaller radii than SiO₂ resonators.

Finally, material defects must be addressed in the fabrication process. Material defects include surface roughness and any discontinuities within the film. The roughness of the sidewall is especially important, since a large fraction of the optical mode overlaps with sidewall, and any irregularities it sees will scatter light out of the optical mode. Thus, fabrication processes must be developed to minimize surface roughness and maximize overall film quality.

4.2 Previous High Q_{opt} Resonators

There are several examples in the literature of microfabricated ring/disk resonators with high Q_{opt} . In Si, the highest demonstrated Q_{opt} of 5 million was achieved using a specially-developed etch process for minimal sidewall roughness, and it was measured using a tapered fiber. [2] Typical Si resonators with integrated waveguides have Q_{opt} on the order of 1 million. [1, 60]

The Q_{opt} of Si₃N₄ optical resonators is strongly influenced by film quality. The highest Q_{opt} example is made of thick (up to 910 nm) stoichiometric Si₃N₄ that is annealed at high temperature (around 1200°C) and clad in a thin layer of SiO₂. To address film stress issues associated with the very thick Si₃N₄, the wafer must have stress-relief trenches where the film will preferentially crack to ensure that some parts of the Si₃N₄ film will remain intact for device fabrication. These have Q_{opt} up to 7 million. [5, 56]

Hybrid Si₃N₄/SiO₂ resonators have also demonstrated high Q_{opt} . These devices consist of a very thin (less than 80 nm) layer of stoichiometric Si₃N₄ etch to form a waveguide and embedded in a very thick (about 15 μm) layer of SiO₂. [61] Because most of the mode is in the oxide cladding, and very little of the mode overlaps with the refractive index step at the boundary of the oxide and nitride, very low loss can be achieved. With this structure, a variety of on-chip optical components, including waveguides evanescently coupled to ring resonators, has been demonstrated. However, because the mode confinement is minimal, bending radii must be large. The highest Q_{opt} shown in this type of device is 28 million at a radius of 5 mm and wavelength of 1310 nm. The smallest demonstrated resonator had a radius of 2 mm and Q_{opt} of 7 million at 1550 nm wavelength. [6]

Very high Q_{opt} has been achieved in SiO₂ using a couple of different methods. One

method is the formation of silica microtoroids. [3] To fabricate these, 2 μm thermal SiO_2 is etched in buffered HF to form disks. Then, these disks are undercut using XeF_2 . Finally, to smooth out any sidewall roughness, each released disk is laser melted to form a microtoroid with major radius significantly less than that of the original disk. These devices can have Q_{opt} greater than 100 million for devices with radii on the order of 50 μm .

In the "wedge resonator" method, [4, 62] thick (approx. 10 μm) thermal SiO_2 is etched with buffered HF to form a wedge-shaped sidewall profile. By adjusting the adhesion of the photoresist to the SiO_2 during the etch, the wedge's angle can be made as small as 10°. This confines the optical mode such that it has very little overlap with the etched sidewall, and Q_{opt} from about 20 million up to 875 million has been demonstrated in devices with radii between 0.1 and 4mm.

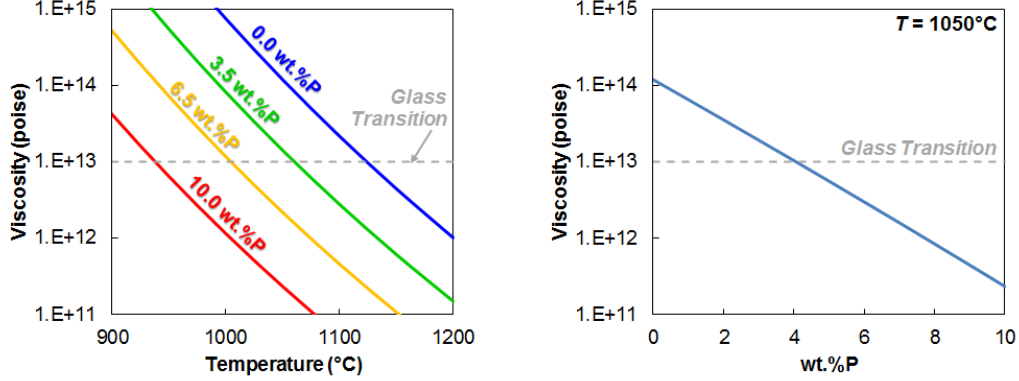
4.3 Doped SiO_2 as an Optical Resonator Material

Based on the intrinsic material properties as well as the experimentally-demonstrated resonators, it is clear that SiO_2 has one of the highest potential Q_{opt} among common micro-fabrication materials. However, previous examples of SiO_2 resonators require non-standard, non-wafer-scale processing techniques. In addition, these methods make integrating on-chip, evanescently-coupled waveguides very challenging, since the lithographically-defined radii are much larger than the final radii. We want to develop a wafer-scale process for high- Q_{opt} SiO_2 resonators that can be integrated with on-chip waveguides.

Having chosen the material, the challenge is to make the sidewalls smooth enough to achieve the desired high Q_{opt} . Without special treatment, HF-etched SiO_2 disks have Q_{opt} on the order of 10^5 , demonstrating that even a chemical etch leaves an imperfect surface. [3] Melting, as demonstrated by the laser-melted silica microtoroids, is an effective method for reducing this surface roughness, but the localized heating process results in significant dimensional changes. To integrate with on-chip waveguides, we looked for a way of melting SiO_2 that did not result in large dimensional changes. However, melting pure silica requires an anneal temperature above 1660°C to reach the softening point. [63] Not only is this temperature too high to be feasible in a standard microprocessing environment, it is also well above the melting point of the Si substrate (1410°C).

The solution to this high-temperature issue is to use doped SiO_2 , which lowers the temperature required for smoothing to a realistic value. Phosphosilicate glass (PSG) is a commonly-used microprocessing material, and, because of its phosphorus content, it has a much lower melting point than pure SiO_2 . Figure 4.1b shows the theoretical viscosity of PSG at a temperature of 1050°C with respect to the phosphorus content in the film, using the equations in [63]. For reference, the glass transition point, defined as a viscosity of 10^{13} poise, is also marked on the graph. The actual point at which a material can "flow" does not have a standard definition, but has been experimentally demonstrated at higher temperatures (lower viscosities) than the theoretical glass transition point. For example, the theoretical glass transition temperature of PSG with approximately 7 wt.%P is 995°C, [63] and 7 wt.%P PSG has been shown to flow around 1050°C. [64]

Of course, adding impurities to SiO_2 may add some optical absorption, but it is not clear from the literature how much it should add. Previous studies of optical loss in phosphorus-



(a) PSG viscosity as a function of temperature at varying phosphorus content (b) PSG viscosity at 1050 °C as a function of phosphorus content

Figure 4.1: The theoretical effect of phosphorus content on silica viscosity. (Calculated from C.R. Hammond, *Physics and Chemistry of Glasses* **19**(3), pp. 41-42, 1978.)

and boron-doped optical *fibers* does not show significant difference in absorption for wavelengths greater than 3 μm , [65] and for wavelengths around 1.5 μm , losses on the order of 1 dB/km have been measured, [66] which is about ten times lossier than the loss of pure SiO_2 but still many orders of magnitude better than lightly-doped Si, as shown in Table 4.1. Thus, doped silica is a promising material for high Q_{opt} resonators.

4.4 Fabrication Process Development

The general fabrication process for our doped silica optical resonators is fairly simple. Starting with a plain Si wafer, we deposited approximately 6 wt.%P phosphosilicate glass in an LPCVD furnace followed by a densification anneal in N_2 . As a part of process development, we tried variations of time and temperature in the densification process. We then patterned the resonators in photoresist and dry etched them. The sidewalls were then smoothed by reflow at high temperature in nitrogen, and the resonators were finally released by timed etch in XeF_2 gas, which etches the underlying Si isotropically. Of course, achieving high Q_{opt} required special attention to the details of this process, which we will describe in the following sections.

We can characterize these resonators by looking at the signal through a tapered optical fiber evanescently coupled to them, a technique similar to [3]. Because the tapered fiber is mounted on an external micropositioning stage, this technique enables precise control over the coupling distance, and the evolution of resonances from the overcoupled through the undercoupled regimes can be observed. To see the resonances, we step the wavelength of a tunable laser at the input, and the optical resonances manifest as “dips” in the power measured through the tapered fiber. To determine the intrinsic Q_{opt} , we measure the loaded Q_{opt} at different tapered fiber positions. As we move the tapered fiber away, and it becomes increasingly undercoupled, the loaded Q_{opt} becomes more and more dominated by the intrinsic Q_{opt} . By following this evolution of a resonance, we can determine the intrinsic Q_{opt} .

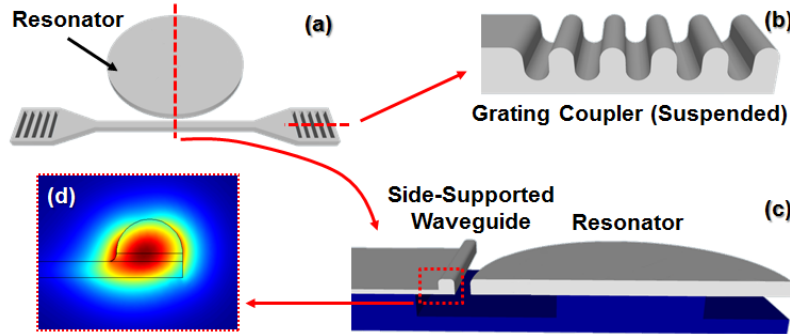


Figure 4.2: Concept of PSG resonator with integrated, side-supported waveguide and grating coupler, including (a) overview of device, (b) cross-section of vertical grating coupler, (c) cross section showing side-supported waveguide coupling to resonator, and (d) finite element model of the optical mode in the side-supported waveguide

at the most undercoupled point.

One important factor to consider in order to get the most accurate Q_{opt} measurement is thermal nonlinearity, described in Section 3.3.2. If too much power is injected into the resonator, it will heat up, and the resonance wavelength will increase as the laser scans from the blue side of the resonance. [67] This distorts the apparent shape of the resonance and will give an inaccurate Q_{opt} value. Consequently, the laser power should be kept low enough that the effect of the thermal nonlinearity is negligible.

We can also probe these resonators with integrated on-chip waveguides. Coupling light into such waveguides can be accomplished via either edge coupling or vertical grating couplers. Using finite-difference time-domain (FDTD) modeling, we designed vertical grating couplers for a 900 nm-thick PSG film, where the grating was defined by a partial etch of the PSG. Details on this design will be given in Section 6.2.3. The partial etch depth chosen for the grating design was also used to define a “side-supported” waveguide to couple to the resonator. Because, like the resonators, the waveguides are made of silica, the optical mode must not overlap with the silicon, or light will leak into the substrate. To anchor the waveguide to the substrate far from the optical mode, we used a continuous “side support,” shown in Figure 4.2c. The partial etch depth chosen for the grating was 613 nm, which left 287 nm PSG as the waveguide’s side-support thickness. We used finite-element modeling to simulate the optical mode for this side-supported structure (Figure 4.2d), and we found that the optical mode for this design remained confined to the waveguide, with little of the optical field escaping into the side support.

Including these waveguides with the resonators requires some additional fabrication steps, shown in Figure 4.3. For smaller resonators, we also include in the resonator an anchor to the substrate so that we can sufficiently undercut the waveguide without detaching the resonator. Unlike the tapered-fiber measurement technique, this particular structure does not have a tunable coupling distance between the waveguide and the resonator. Instead, we fabricated an array of devices with varying coupling distance and measured each one to observe the resonances from overcoupled to undercoupled regimes.

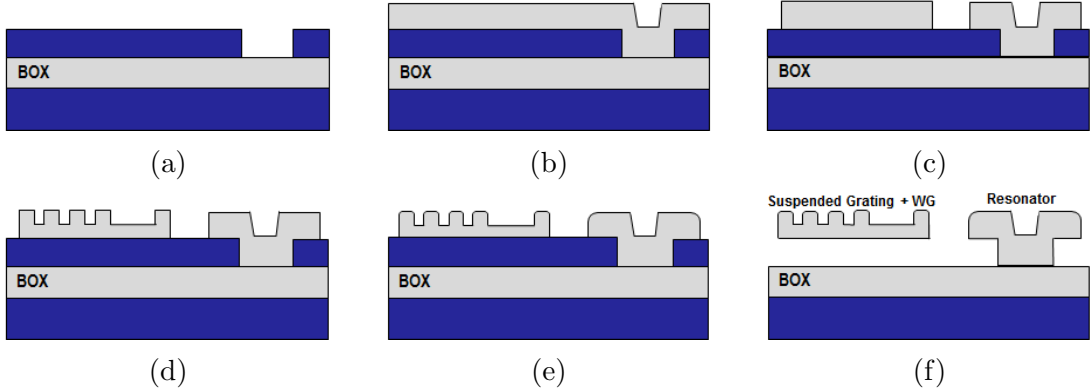


Figure 4.3: Fabrication process flow for PSG resonator with integrated waveguides and grating couplers, starting with an SOI wafer (a) Etch anchor vias through Si device layer (b) Deposit LPCVD PSG (c) Define in photoresist and fully etch devices (d) Define in photoresist and partially etch to form gratings and side-supported waveguides (e) Reflow PSG in N_2 (f) Release in XeF_2

4.4.1 Initial Results

By optimizing the process flow, we were able to greatly exceed the Q_{opt} of unaltered, wet-etched SiO_2 devices. Some of the important steps of the fabrication process for reducing sidewall roughness and increasing film quality are densification conditions, photoresist treatment, device etch, film thickness, reflow time, and reflow temperature.

We varied the densification time from 0.5 to 2 hours and temperature from $900^\circ C$ to $1050^\circ C$, but saw no correlation between densification conditions and device Q_{opt} . With regards to photoresist treatment, standing wave effects during exposure can induce line edge roughness in the photoresist mask, which can contribute to the sidewall roughness of the resonator. To reduce this roughness, the photoresist was reflowed prior to hard bake in a process similar to [68].

Another important factor in minimizing the final sidewall roughness of the resonator is the device etch itself. Starting with a smoother surface before the PSG reflow process makes it so that a less aggressive reflow is required. We found that the chemistry of the reactive ion etch was especially important. Devices etched in CHF_3 , CF_4 , and Ar had visibly more sidewall roughness than those etched in C_4F_8 , H_2 , and He, as shown in Figures 4.4a and 4.4b. This difference can be attributed to the degree of physical (sputter) etching in the process. The Ar in the first etch chemistry causes sputtering to be the dominant process, [69] and, as a result, photoresist can be knocked off and redeposited on the sidewalls. This results in micromasking during the etch, which increases sidewall roughness. Even for the more chemically-dominated etch, there is still some remaining sidewall roughness (Figure 4.4b). However, we see that the sidewall roughness is visibly reduced after reflow, as shown in Figure 4.4c.

An important aspect to note regarding the reflow process is the degree to which it induces dimensional change. If the lithographically-defined device dimensions are significantly altered by the reflow process, it will be challenging to integrate waveguides on-chip with

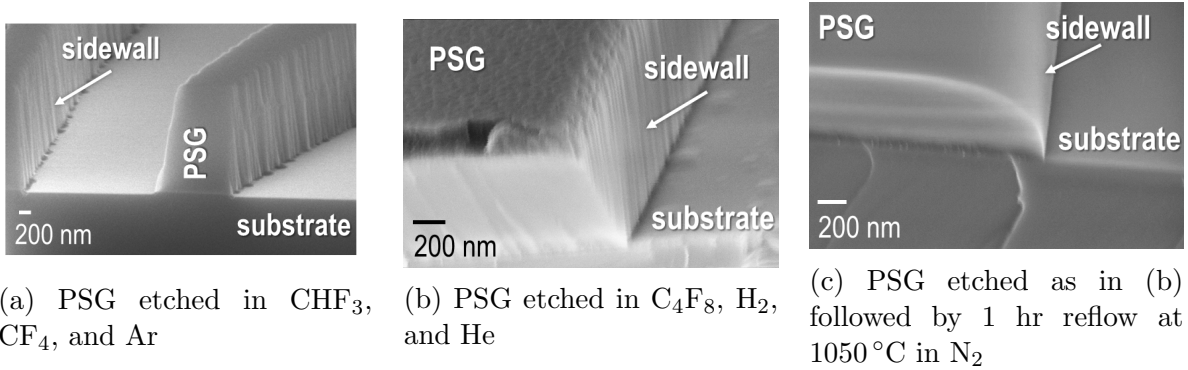


Figure 4.4: SEMs of cross-sections of etched PSG

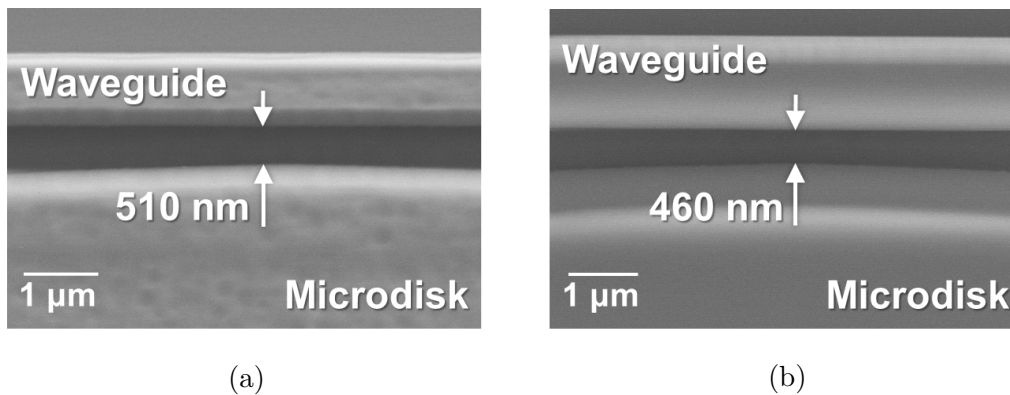


Figure 4.5: The reflow process has minimal effect on lithographically-defined dimensions. (a) Prior to reflow, the gap between the waveguide and resonator is about 510 nm. (b) Following a 4 hr reflow at 1050°C , the gap reduces to about 460 nm.

the resonators. Fortunately, we see minimal dimensional changes; on average, feature edges expanded by approximately 30 nm. For example, Figure 4.5 shows an etched gap of 510 nm prior to reflow, which shrinks to 460 nm after reflowing for 4 hr at 1050°C .

The final three variables in the fabrication process flow, film thickness, reflow time, and reflow temperature, were optimized by fabricating a number of combinations and measuring the Q_{opt} of the resultant $50\ \mu\text{m}$ disk devices. The results are summarized in Figure 4.6. We see that, to a point, Q_{opt} is improved in thicker films reflowed for longer times at higher temperatures. For example, the highest Q_{opt} we achieve with this process is about 5.6 million for a $2\ \mu\text{m}$ thick resonator reflowed for 4 hours at 1050°C , but for a reflow time of 8 hours at the same temperature, the Q_{opt} is only 3.2 million.

The highest Q_{opt} resonance, measured with a tapered fiber, is shown in Figure 4.7. It is clearly a resonance doublet, which forms in optical resonators when there is light in both a clockwise and counter-clockwise mode. The scattering into the backward propagating mode couples what would otherwise be degenerate modes, causing the modes to split. [70] The measured doublet is an indication that, despite the high Q_{opt} , there is still some defect within the resonator that significantly scatters light into the counter-propagating mode.

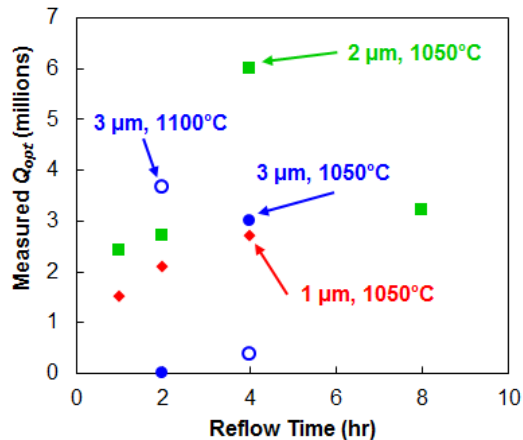


Figure 4.6: Measured Q_{opt} for varying thickness, reflow time, and reflow temperature

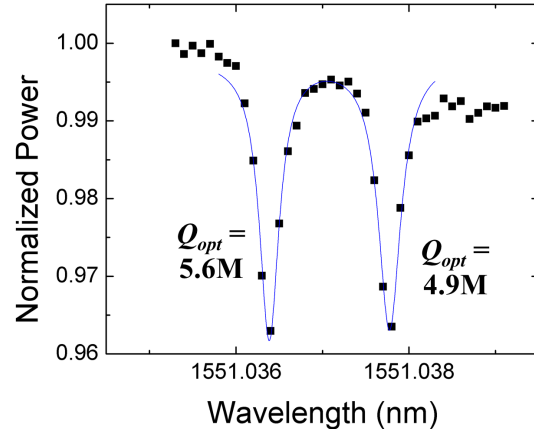


Figure 4.7: Doublet resonance from 2 μm thick, 50 μm radius disk reflowed for 4 hr at 1050 $^{\circ}\text{C}$. Measured via tapered fiber using a stepwise laser scan. Data is fit to a Lorentzian to determine the Q_{opt} .

4.4.2 Bubble Formation from Aggressive Reflow Conditions

The remaining defects in the optical resonator were made more clear when we investigated why there is a degradation of Q_{opt} for devices reflowed at higher temperature or for a longer time. We cleaved samples and examined their cross-sections under SEM. Samples that were reflowed for longer times or at higher temperature had visible “bubbles” within the PSG film, as shown in Figure 4.8. The presence of these large (on the order of 10 nm) bubbles could explain why the Q_{opt} degraded so much for more aggressive reflow conditions. In addition, the fact that the bubbles continue to enlarge with increasingly aggressive reflow conditions implies that there may also be very small bubbles, smaller than could be seen under SEM, in the 2 μm devices with the high Q_{opt} . This could help explain the optical resonance doublets and suggest an avenue for continuing to improve Q_{opt} .

To develop a way to eliminate these bubbles, we need to determine their origin. Potential explanations include an imperfect interface between the substrate and the PSG, phosphorus compounds precipitating out of the PSG, and the presence of defects in the initially deposited film.

To address the possibility that the bubbles originate at the interface with the Si substrate, we looked at the cross-section of a sample that was deposited in multiple steps. Specifically, we deposited 1 μm PSG, densified for 1 hr at 1050 $^{\circ}\text{C}$, then repeated the 1 μm deposition followed by a 2 hr densification at 1050 $^{\circ}\text{C}$ to get a total of 2 μm PSG. After etching the devices, we reflow for 8 hours at 1050 $^{\circ}\text{C}$. If the bubbles originate at the substrate surface, there should have been one group of bubbles, and they would probably be close to the substrate. However, as shown in the cross-section in Figure 4.8c, we saw two separate layers of bubbles that correspond to the two separate PSG deposition steps. This implies that the bubbles are intrinsic to the PSG itself, and do not originate from the substrate surface.

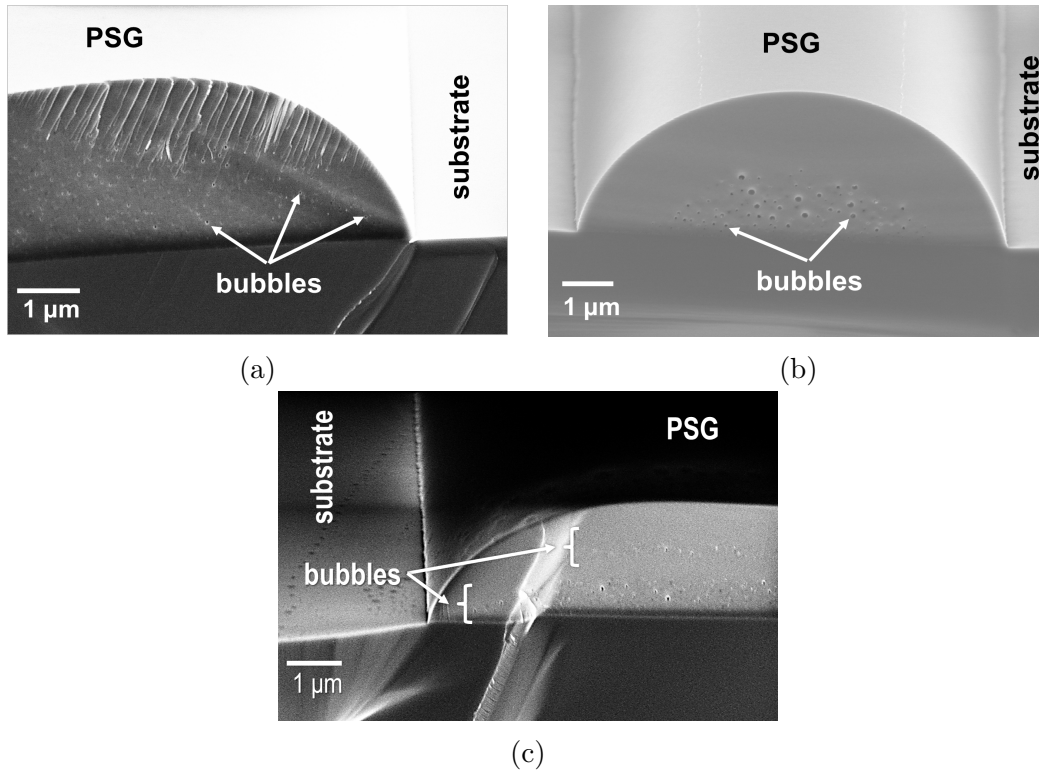


Figure 4.8: SEMs of cleaved PSG samples. (a) Cross-section of a 2 μm thick PSG film after 8 hr reflow at 1050°C. Bubbles are numerous but less than 10 nm in diameter. (b) Cross-section of a 3 μm thick PSG film after 4 hr reflow at 1100°C. Bubbles are larger than 10 nm in diameter. (c) Cross-section of a 2 μm thick PSG film that was deposited in two deposition/densification steps. After etch, PSG was reflowed 8 hours at 1050°C. Bubbles appear in two distinct groups.

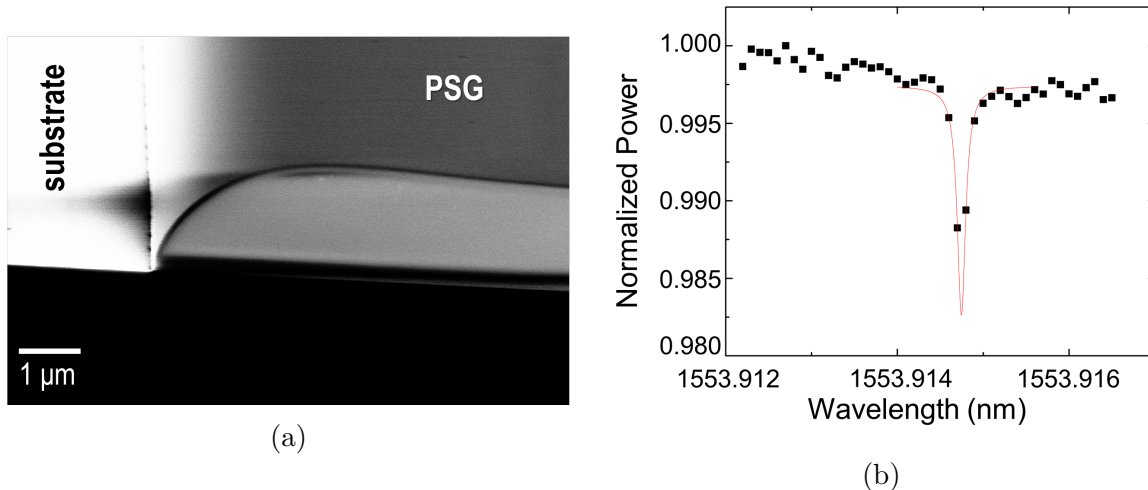


Figure 4.9: Results from “oxidized” PSG process. (a) SEM cross-section of 2 μm thick PSG film annealed in N_2 , O_2 , and H_2O followed by device etch and 4 hr reflow at 1050°C . Bubbles could not be found under SEM. (b) Stepwise laser scan at 0.1 μm resolution of a resonance in 50 μm radius disk. Lorentzian fit of data indicates $Q_{opt} = 13.2$ million, but the number of points is too low to get a good fit of the resonance.

4.4.3 Results from Post-Deposition Anneal Modification

We again deposited a 2 μm PSG film, but, in addition to a 1 hr densification at 900°C in N_2 , we put the unpatterned PSG film through 15 min of dry oxidation followed by 100 min of wet oxidation, both at 900°C . Because of the thick 2 μm PSG film, very little of the O_2 or H_2O could diffuse through to the substrate surface; theoretically, only about 55 nm thermal oxide should have formed at the Si-PSG interface from this step.

After etching the PSG to form the optical resonators, we reflowed them for 4 hr at 1050°C . A cross-section of the resultant film is shown in Figure 4.9a. Under SEM, the film quality appeared excellent, with no sign of bubbles.

As we do not precisely know the origins of the bubbles, it is difficult to say how the oxidation process reduced them. Based on where they form, they seem to originate in the PSG film itself, and we see them after long and high-temperature reflows because, perhaps, defects in the initially-deposited PSG film are magnified or agglomerated by the reflow process. If the defects are silicon-rich areas in the deposited film, it makes sense that “oxidizing” the PSG would neutralize such defects. Another possibility is that the bubbles are simply a result of porosity in the deposited PSG film, and the O_2 and steam environments during the oxidation step enable increased migration of the molecules in the PSG film, so the bubbles could quickly move to the surface and escape. This theory is supported by the fact that a steam or oxygen environment can enhance PSG reflow. [71] (Of course, reflowing in steam or O_2 after the device is etched would unfortunately result in the formation of thermal oxide on the exposed silicon, which would prevent device release.) There is some precedent for “oxidation” of an oxide film increasing Q_{opt} ; it was found that to achieve the highest Q_{opt} in wedge resonators, an additional dry oxidation step was required. [4]

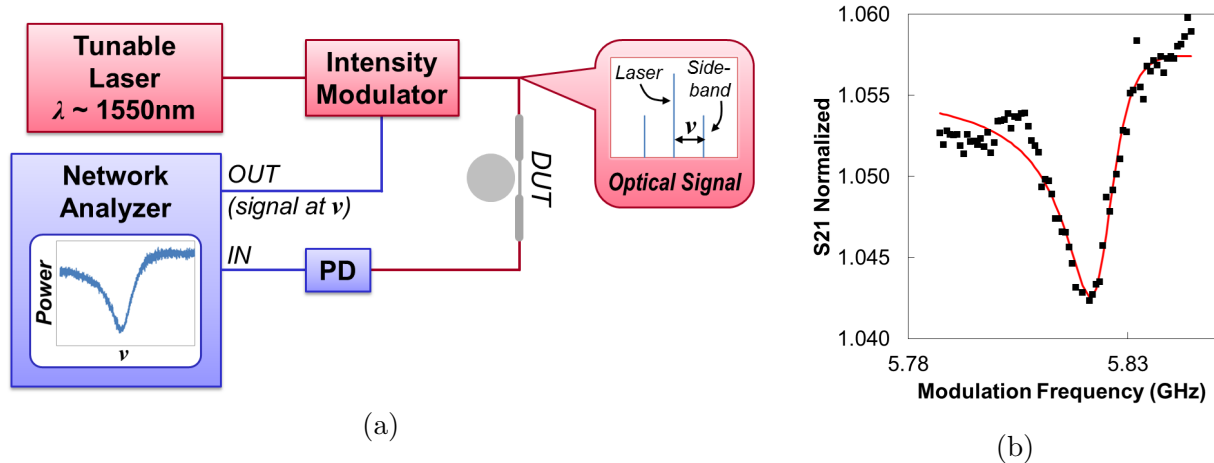


Figure 4.10: Measuring Q_{opt} with network analyzer and modulator. (a) Network analyzer measurement schematic. Optical resonance is probed by sidebands created by the modulator. Sidebands are scanned across resonance by changing modulation frequency ν . (b) Data from network analyzer measurement. Fit indicates $Q_{opt} = 14.7$ million.

Tapered Fiber Characterization

Following release in XeF_2 , we characterized the intrinsic Q_{opt} using the tapered fiber. At the best resolution of the tunable laser (0.1 pm), the highest Q_{opt} resonances were too narrow to be effectively captured by a stepwise scan, as shown in Figure 4.9b. However, this measurement did show two important things: the Q_{opt} of the “oxidized” PSG is higher than previously measured PSG, and the resonances are *NOT* doublets. The fact that the resonances were not split indicates that little light was being scattered into the counter-propagating mode. Thus, the film quality was improved by the oxidation step, which drastically reduced, or perhaps totally eliminated, the bubbles.

To more accurately characterize the high Q_{opt} of these resonators, we modified our characterization technique as shown in Figure 4.10a. Instead of stepping the HP 81682A tunable laser wavelength internally, we modulated the intensity of the laser with an EOspace AZ-AV1-40-PFA-PFA-S modulator while the laser wavelength was fixed close to the resonance we wanted to measure. The generated sidebands were swept across the resonance by changing the modulation frequency via an Agilent E8361A network analyzer. The output signal was detected with a Nortel PP-10G photodiode and sent back into the network analyzer input. The resolution of this scan is limited by the network analyzer, not the tunable laser. This technique is based on modulation spectroscopy, which has been used in several other studies of optical resonators. [25, 43, 72]

We then measured the high Q_{opt} resonance from Figure 4.9b using this new technique, and fit the magnitude data from the network analyzer to more precisely determine the Q_{opt} , as shown in Figure 4.10b. The resonance had a Q_{opt} of 14.7 million, more than twice as high as the previous best Q_{opt} in PSG.

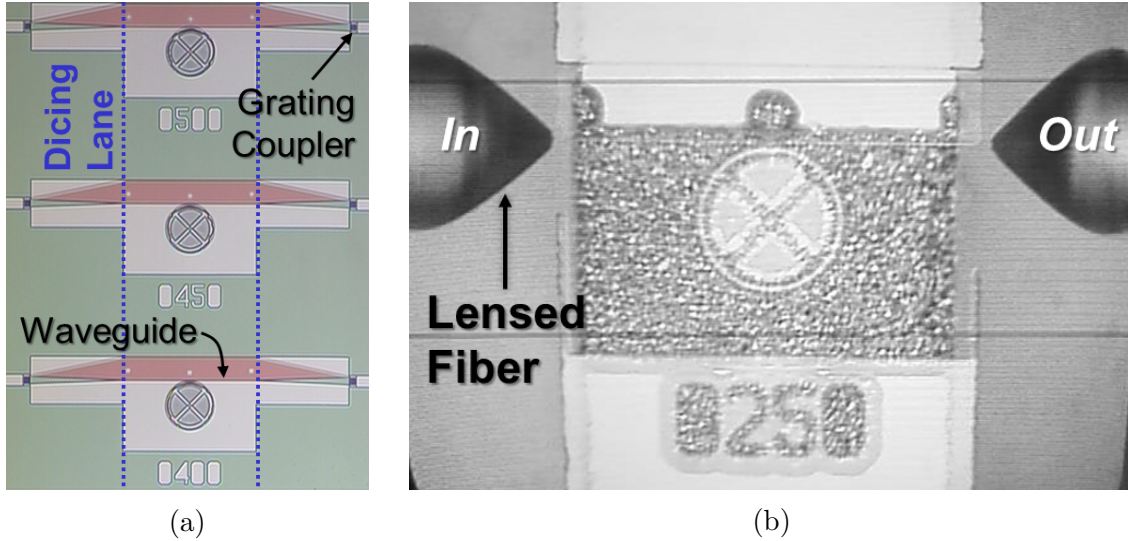


Figure 4.11: Characterizing high Q_{opt} resonators with integrated, side-supported waveguides. Note that the resonators pictured here are spoke-supported rings instead of disks. These are useful as optomechanical devices and will be described in detail in Chapter 6. (a) We fabricated arrays of waveguide and resonators with varying spacing. To enable edge coupling, we dice perpendicular to the waveguides. (b) We coupled into the diced facets of the side-supported waveguides using lensed fibers mounted on separate micropositioning stages. Insertion loss was around 11 dB.

Integrated Waveguide Characterization

We also measured the Q_{opt} of resonators from this same fabrication process using integrated waveguides. We fabricated an array pairs of side-supported waveguides and ring resonators with lithographically-defined coupling distance varying from 250 nm to 2 μm . Before releasing in XeF_2 , we diced perpendicular to the waveguides to form facets for edge coupling to the waveguides, as shown in Figure 4.11a. Edge coupling was accomplished via two lensed fibers mounted on two separate micropositioning stages, as shown in Figure 4.11b. Typical fiber-to-fiber insertion loss was on the order of 11 dB.

The highest loaded Q_{opt} measured using the integrated waveguides is 4 million at a coupling distance of 400 nm. This resonance has a low enough Q_{opt} that we can get a good fit with a stepwise laser scan, shown in Figure 4.12.

The intrinsic Q_{opt} for the integrated waveguide device is lower than the stand-alone device measured via tapered fiber at least in part because it is a spoke-supported ring instead of a disk, and, although we designed the ring width to minimize interaction between the optical mode and the spokes, some small fraction of the light may have been scattered, reducing Q_{opt} . We will describe the design process for a spoke supported ring, which is a convenient geometry for optomechanical devices, in Chapter 6. Despite the lower Q_{opt} , this measurement shows that on-chip PSG waveguides can be integrated with high Q_{opt} reflowed PSG resonators.

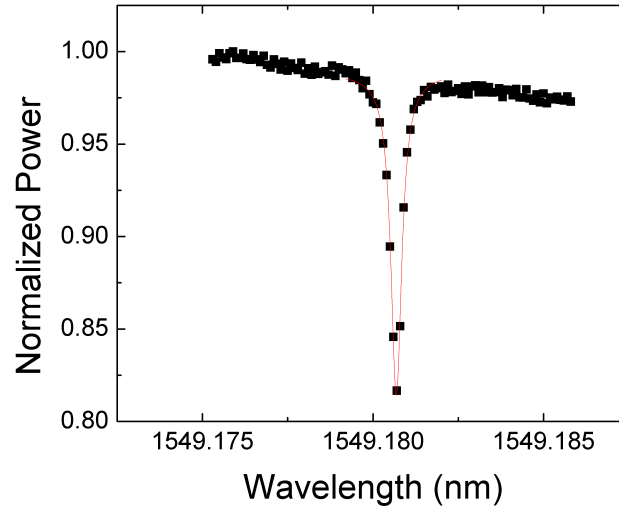


Figure 4.12: Measurement of Q_{opt} of a 50 μm radius spoke-supported ring, where the ring-waveguide spacing is 400 nm. The resonance was scanned via a tunable laser stepped at a resolution of 0.1 pm. The Lorentzian fit of the data yields a loaded Q_{opt} of 4 million.

4.5 Comparison to Previous Work and Implications

The high Q_{opt} PSG resonator compares favorably with the previous work outlined near the beginning of the chapter. The optical Q s of all these devices are graphed in Figure 4.13 with respect to device radius. Although higher Q_{opt} has been demonstrated in millimeter-scale devices, for devices less than 100 μm in radius, which take up less space and have larger free spectral range, the reflowed PSG optical resonator Q_{opt} is only exceeded by that of the silica microtoroid and silica “wedge” resonators, but the reflowed PSG resonator has several added benefits. First, the fabrication process is wafer scale and composed of conventional microprocessing steps. Also, the resonator’s lithographically-defined dimensions are not changed significantly by the smoothing process, so on-chip evanescently-coupled waveguides can be easily integrated with the resonator. Thus, reflowed PSG resonators are a viable platform for implementing resonators with $Q_{opt} > 10$ million in on-chip integrated devices.

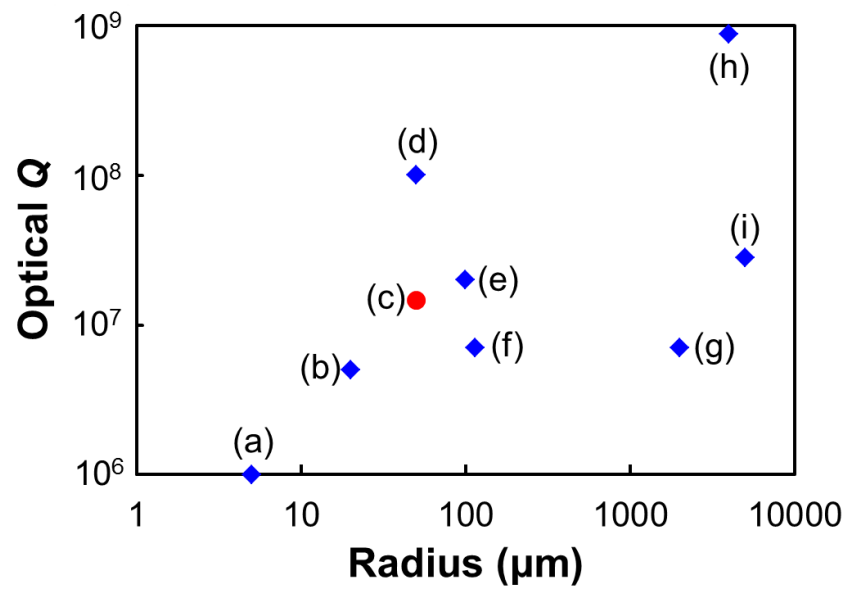


Figure 4.13: Q_{opt} of notable optical disk and ring resonators with respect to device radius. (a) Si disk from [1] (b) Si disk from [2] (c) The high- Q_{opt} reflowed PSG from this work (d) SiO₂ microtoroid from [3] (e) SiO₂ wedge resonator from [4] (f) Thick stoichiometric Si₃N₄ resonator from [5] (g) SiO₂/Si₃N₄ hybrid ring resonator from [6] (h) SiO₂ wedge resonator from [4] (i) SiO₂/Si₃N₄ hybrid ring resonator from [6]

Chapter 5

A Silica MEMS-Actuated Tunable-Bandwidth Filter

Optical tunable-bandwidth filters are a key component in optical communication networks. In a wavelength-division-multiplexed system, a tunable filter can be useful for amplified spontaneous emission (ASE) noise filtering, optical filter optimization to maximize the optical signal-to-noise ratio, dynamic bandwidth allocation, reconfigurable channel routing, and performance monitoring. [73, 74] For these applications, one of the key parameters is the minimum achievable bandwidth. Performance monitoring, in particular, has enhanced sensitivity with a narrower bandwidth. [74] With these applications in mind, our goal was to develop a tunable-bandwidth filter with a very low minimum bandwidth of less than 1 GHz (8 pm).

5.1 Previous Tunable-Bandwidth Filters

On-chip tunable-bandwidth optical filters have generally been implemented by changing the coupling between an optical resonator and a waveguide. As described in Section 2.2.3, the coupling can be tuned by changing several device parameters. The simplest parameters to dynamically tune are the propagation constant of the waveguide and the coupling distance between the waveguide and the resonator, as diagrammed in Figure 5.1. Tuning the propagation constant is used in a Mach-Zehnder Interferometer (MZI) geometry, where one arm of the MZI is the waveguide, which couples to the resonator in two different places. The other arm of the MZI is the resonator itself between the two coupling points. Coupling, and therefore bandwidth, is tuned by changing the relative phase between these two arms, and this is accomplished by tuning the propagation constant in the waveguide. The coupling constant can also be tuned by simply moving the waveguide relative to the resonator. The minimum bandwidth in both of these devices is limited by the intrinsic optical quality factor of the resonator.

The propagation constant of a coupling waveguide can be modified by changing the index of refraction n . Techniques for tuning n include carrier injection and temperature control. Thermal tuning of the coupling has been demonstrated in several silicon devices, [17, 18, 38] and the device with the lowest minimum bandwidth had a tuning range of 12.5 to 87.4

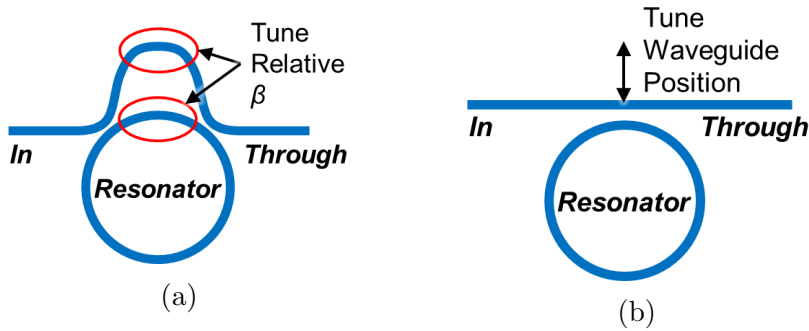


Figure 5.1: There are two main methods by which bandwidth tuning in optical filters has been accomplished. (a) In MZI-based tuning, a waveguide couples to the resonator in two places, and the relative phase between these two coupling points is changed by changing the propagation constant in the waveguide between the two points. This tunes the effective coupling constant between the waveguide and the resonator, thereby tuning the bandwidth. (b) In positional tuning, the distance between the waveguide and the resonator is changed. This changes the coupling constant, thus changing the bandwidth of the optical filter.

GHz. [38]

Changing the coupling distance between the waveguide and the resonator will also change the effective bandwidth of the filter. Thus, MEMS electrostatic actuators have also been successfully demonstrated as a technique for tuning bandwidth. The best-performing device using this technique had a tuning range of 2.8 to 78.4 GHz. [16]

To bring about a lower minimum bandwidth than these devices, we utilized the process we developed for achieving high optical Q in phosphosilicate glass (PSG) resonators described in Chapter 2. Silica, as an insulator, is not susceptible to carrier injection as a means to tune the refractive index. In addition, its low thermo-optic response and low thermal conductivity (see Table 3.1) mean that much more power would be required to change the refractive index than is required in silicon. As a result, we chose to tune the bandwidth by changing the waveguide-resonator gap.

5.2 Device Design

Having PSG as the device material introduces some challenges when designing a tunable filter. Because of the low index of refraction, all optical components must be suspended so light does not escape into the substrate. In addition, since PSG is not electrically conductive, the MEMS must be implemented in a different material. To address these constraints, we developed the device layout shown in Figure 5.2. Here, the optical resonator and waveguides are suspended in air, and the waveguide is attached laterally to a MEMS comb drive actuator, which is implemented in thick silicon below the PSG layer. This device, having a single waveguide coupling to the resonator, is a notch filter. However, other filter architectures can be implemented by adding a second coupling waveguide.

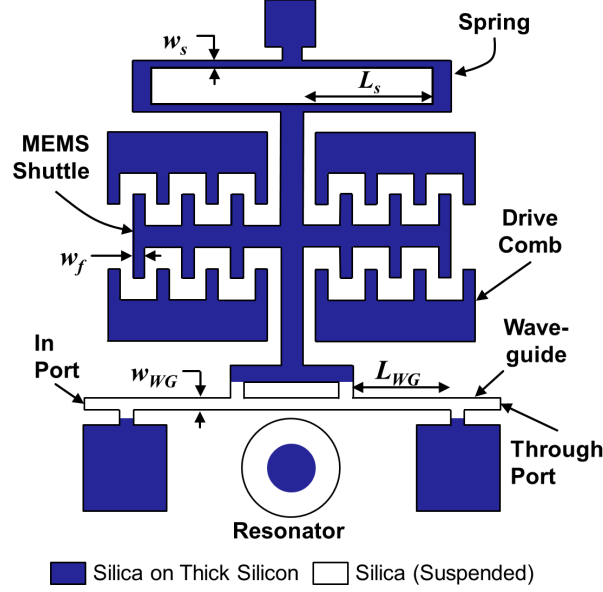


Figure 5.2: Schematic of silica tunable-bandwidth filter concept. The waveguide and resonator are suspended in air, while the MEMS actuator is implemented in silicon underneath the silica layer. The waveguide is “anchored” by lateral connections to the MEMS, and the resonator is anchored in its center.

5.2.1 MEMS Design

The design of the MEMS structure is focused on the expected waveguide displacement with respect to applied bias. We aimed for a total displacement of $2\ \mu\text{m}$ with a bias of less than 100V. The compliance of the structure was dependent on both the MEMS spring and the waveguide. The applied force as a function of bias voltage was adjusted by the number of fingers on the comb.

The spring constant of the single-folded spring is approximately equivalent to a parallel combination of two series of four cantilevers having half the length of the spring L_s , as follows [75]:

$$k_c(L_c) = \frac{1}{4} E h_c \left(\frac{w_c}{L_c} \right)^3 \quad (5.1a)$$

$$k_s = 2 \times \frac{k_c(L_s/2)}{4} = E_s h_s \left(\frac{w_s}{L_s} \right)^3 \quad (5.1b)$$

Here, E is the modulus of elasticity for the spring, the spring thickness orthogonal to the plane of motion $h_s = h_c$, the spring width in the plane of motion $w_s = w_c$, and the spring length (Figure 5.2) $L_s = 2L_c$. For our design, E_s is the modulus of elasticity of silicon.

The waveguide, which is in parallel with the single-folded spring, is, approximately, a parallel combination of two series of two cantilevers having half the length of the bending part of the waveguide L_{WG} , as shown in Figure 5.2. Assuming the waveguide length change is small, the waveguide spring constant and the total MEMS spring constant are expressed

as:

$$k_{WG} = 2 \times \frac{k_c(L_{WG}/2)}{2} = 2E_{WG}h_{WG} \left(\frac{w_{WG}}{L_{WG}} \right)^3 \quad (5.2a)$$

$$k_{\text{tot}} = k_s + k_{WG} \quad (5.2b)$$

For our design, the Young's modulus of the waveguide E_{WG} is that of PSG. The electrostatic force from the comb fingers, neglecting fringing fields, is as follows [76, 77]:

$$F_{\text{comb}}(V) = \frac{N\epsilon_0 h_s}{d} V^2 \quad (5.3)$$

Here, N is the number of fingers on the drive comb, and d is the size of the gap between the drive and shuttle comb fingers. There is also a small parallel-plate component to the force between the tips of the comb fingers and the base of the opposing comb. This is, approximately, as a function of the displacement:

$$F_p(V, x) = \frac{(N-1)\epsilon_0 h_s w_f}{(x_0 - x)^2} V^2 \quad (5.4)$$

where w_f is the width of a comb finger, and x_0 is the initial distance between the end of the shuttle comb finger and the base of the drive comb fingers, assuming both sets of combs have the same length.

The displacement of the MEMS shuttle as a function of applied bias voltage is found by setting the force from the springs equal to the electrostatic force. For this device, displacement is found by solving the following equation:

$$\left(E_s h_s \left(\frac{w_s}{L_s} \right)^3 + 2E_{WG} h_{WG} \left(\frac{w_{WG}}{L_{WG}} \right)^3 \right) x = \left(\frac{N}{d} + \frac{(N-1)w_f}{2(x_0 - x)^2} \right) \epsilon_0 h_s V^2 \quad (5.5)$$

This neglects any fringing fields contributing to the electrostatic force, and it assumes that the springs behave purely linearly with respect to displacement. In addition, we have neglected the fact that the single-folded spring is composed not only of thick silicon but also of a 1 μm layer of PSG. Based on Eq. 5.5, if we neglect the electrostatic force due to the tips of the comb fingers, the displacement is quadratically related to the applied voltage. Figure 5.3 shows the theoretical displacement with and without the parallel-plate electrostatic force. At small displacements, the two theoretical curves are about the same. However, including the electrostatic force from the comb finger ends indicates a ‘‘pull-in’’ behavior; when the displacement exceeds $2/3$ of the initial gap, the parallel-plate electrostatic force is larger than and growing much faster than the force from the springs, so the shuttle combs are pulled completely into the drive combs.

5.2.2 Optical Design

Some optimization was required to achieve optical performance suitable for the target application. For the optical resonator, a 50 μm radius was chosen in order to have a free

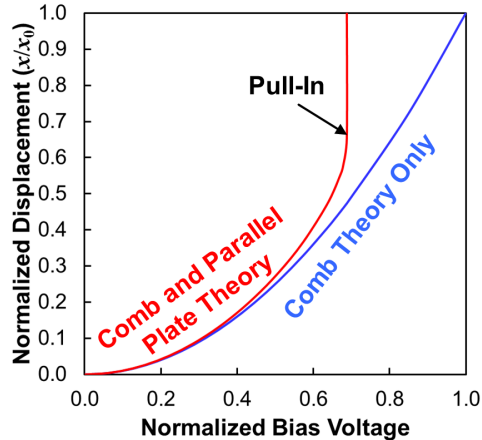


Figure 5.3: Theoretical MEMS displacement with respect to applied voltage between the MEMS shuttle and drive electrodes. One curve shows the displacement while taking into account only the electrostatic force due to the sides of the comb fingers, while the other curve also includes the electrostatic force due to parallel-plate attraction between the comb finger tips and the base of the opposing comb. For small displacements, these two graphs match.

spectral range of about 5 nm, which is a common channel spacing for coarse optical WDM systems.

Integrating the optical components with the MEMS actuator introduces some additional constraints on the waveguide. The design of the waveguide is especially important, as it is both the means of coupling light into the resonator and one of the MEMS springs. Its width and suspended length are important both for the MEMS spring constant, and its width affects the coupling to the optical resonator and the propagation loss in the waveguide. In addition, the optical components must be far removed from the silicon to minimize optical loss, so somehow it must be connected in a low-loss manner to the silicon MEMS.

We chose a waveguide width of 1 μm . A narrower waveguide than this would lead to increases in propagation loss along the waveguide, as the waveguide width would be less than the wavelength of light in PSG ($n \approx 1.45$). As a result, a large fraction of the optical mode in the waveguide would overlap with the surface, amplifying the effect of any scattering sites (such as waveguide connection points). Increasing the waveguide width above 1 μm would lead to an increase in the waveguide spring constant, and it would decrease the coupling constant c_m between the waveguide and the resonator, as plotted in Figure 5.4. A smaller c_m means a shorter critical coupling distance, which can limit the degree to which we can overcouple to the resonator. A 1 μm waveguide width is a good compromise between all these factors.

For an attachment point having minimal loss, we used an adiabatic taper at an angle of approximately 4.3° out to a total width of 2.5 μm (Figure 5.5). According to beam propagation method (BPM) simulation, each tapered attachment should have about 0.07 dB loss.

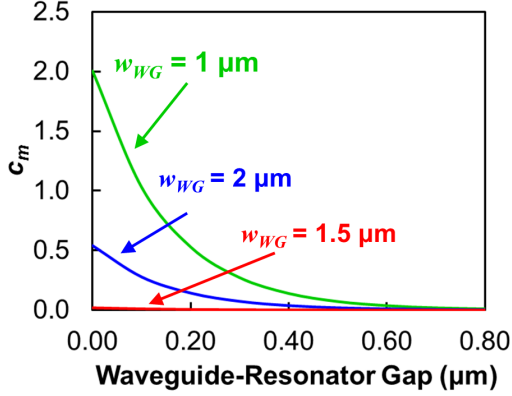


Figure 5.4: The coupling constant c_m between waveguides of varying width and a microdisk resonator with a $50 \mu\text{m}$ radius, as calculated using Eq. 2.20.

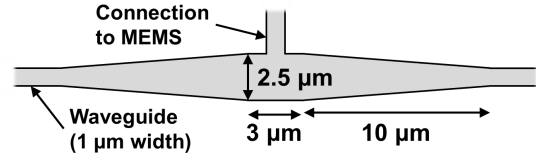


Figure 5.5: Optimized adiabatically-tapered junction for attaching a $1 \mu\text{m}$ -wide suspended waveguide to an anchor or the MEMS actuator. Beam propagation method simulations predict approximately 0.07 dB loss per junction.

5.2.3 Fabrication Process Flow

The tunable-filter was fabricated on an SOI wafer with a thick device layer ($\sim 25 \mu\text{m}$). The optical components were defined in a layer of PSG deposited on top, and the MEMS comb drive was constructed in the SOI device layer. To enable fully-released optical devices while keeping silicon in the MEMS comb drive, we used a modified SCREAM process combined with the PSG reflow technique described in Chapter 4, which is shown in Figure 5.6. [78, 79] The crucial step in this process is shown in Figure 5.6c, in which the region containing optical components is protected by photoresist while a deep silicon etch defines the MEMS comb drive in the SOI device layer. This leaves the optical resonator sitting on a field of silicon, which is exposed in the processing step of Figure 5.6e and etched away the release (Figure 5.6f). Simultaneously, the silicon in the MEMS device is protected by thermal oxide so it is not removed during the release.

Because LPCVD SiO_2 is inherently compressively strained, some additional accommodations may be necessary to keep the waveguide in approximately the same plane as the resonator. If it is out of plane, the minimum coupling distance will be limited by that out-of-plane bending, and if the out-of-plane gap is too large, it may be too far away to couple to the optical resonator at all. One way to address this issue is to lithographically define the waveguide as a lateral curve. This will predispose the waveguide to bend in-plane as a result of the compressive stress instead of bowing up or down.

Figure 5.7 presents some SEMs of the fabricated device. These show that a thick, thermal-oxide protected silicon layer remains in the MEMS comb drive while the waveguide and resonator are successfully released. The PSG components appear nicely smoothed by the reflow process. Also, it is clear that the compressively-stressed waveguide is bowing out of alignment with the resonator, but the amount of bow in this case is not greater than the thickness of the microdisk, so it should not make a significant performance difference.

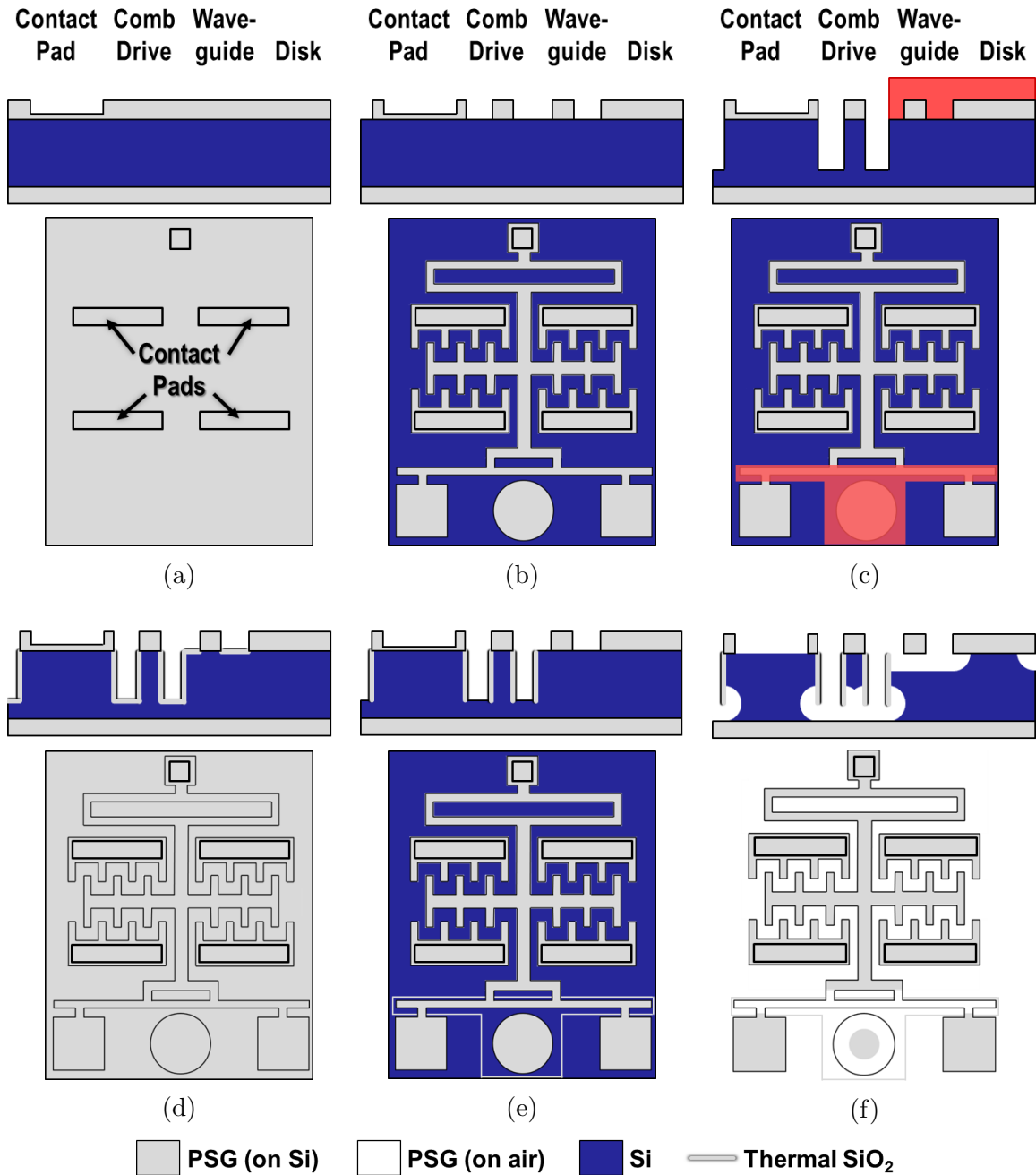


Figure 5.6: Cross sections and top views of the fabrication process for MEMS-actuated PSG tunable-bandwidth filter. Cross sections are not of a specific cut across the device, but rather show representative components. The process begins with an SOI wafer with a thick ($\sim 25 \mu\text{m}$) device layer, on which we deposit $1 \mu\text{m}$ LPCVD PSG. (a) The PSG is partially etched to form contact pads. (b) We define and etch both optical and MEMS components in PSG. (c) While protecting optical components with photoresist, we etch most of the way into the SOI device layer. (d) All exposed Si surfaces are thermally oxidized. (e) We reactively etch away the thermal oxide from all horizontal surfaces. (f) The device is released by isotropically etching Si in XeF_2 .

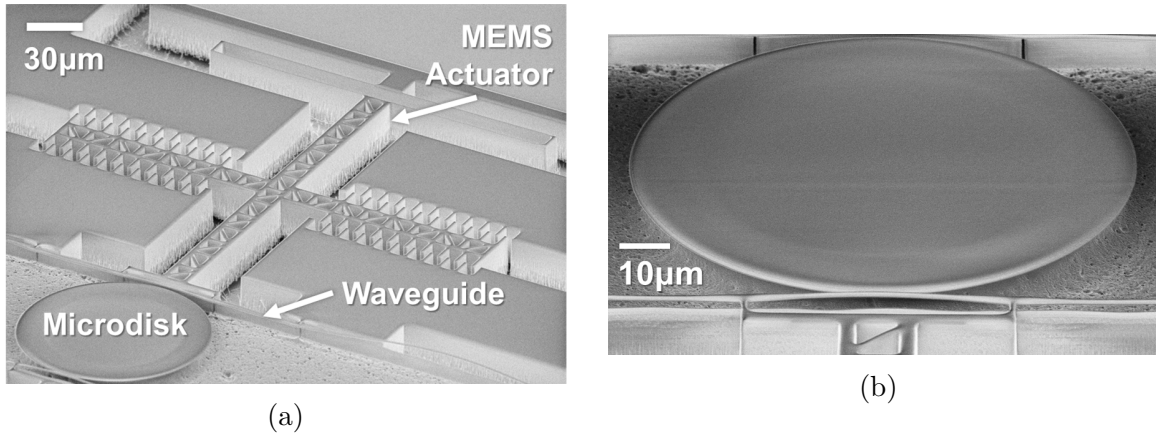


Figure 5.7: SEMs of the fabricated tunable-bandwidth filter. (a) A perspective view, including the MEMS actuator as well as the waveguide and optical resonator. The waveguide and resonator are suspended in air while the comb drive still has a thick layer of silicon below the PSG layer. (b) A zoomed-in view of the waveguide coupling to the resonator. The PSG has been smoothed by the reflow process. Some compressive stress in the PSG has caused the waveguide to bow upwards by about 1 μm .

5.3 Measurement

Devices were optically characterized using the edge-coupling technique described in Chapter 4. To characterize tuning, we applied DC bias between the drive combs and the MEMS shuttle and scanned the tunable laser stepwise across optical resonances at each bias value. A schematic of the characterization setup is presented in Figure 5.8.

5.3.1 MEMS Characterization

To measure the actuation of the MEMS comb drive, high-magnification images were taken of the comb drive position as a function of applied voltage. Then, by comparing to known dimensions in the image, we were able to estimate the displacement of the comb drive. These values are graphed in Figure 5.9. The measured displacement clearly corresponds to the theory presented in Section 5.2.1, with pull-in occurring at about the expected voltage. The small discrepancies between experiment and theory can be explained by variations in Young's modulus from the theoretical value, dimensional differences in the fabricated device, and nonlinear behavior of the springs at large deformation. For the purposes of bandwidth tuning, the required positional range to go from fully overcoupled to fully undercoupled was expected to be less than 2 μm , so the expected actuation voltage would be less than 30 V.

5.3.2 Optical Measurements

The optical resonances were characterized at the through port with varying bias on the MEMS. For the device with the performance presented here, the waveguide was a straight waveguide that had buckled laterally away from the resonator due to the compressive stress in the film. Thus, with zero MEMS bias, the waveguide was too far away to couple to any

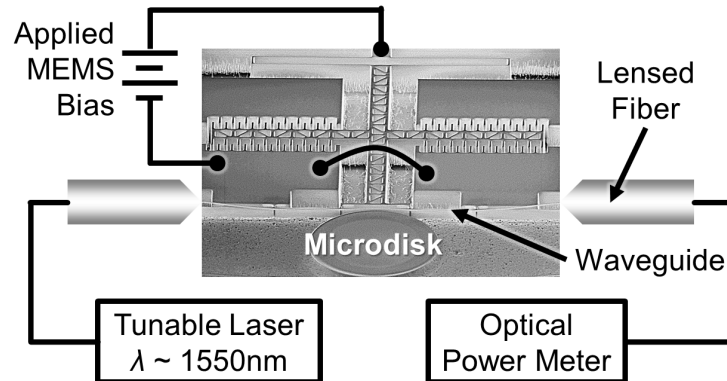


Figure 5.8: The tunable-bandwidth filter is characterized optically with lensed fibers coupled to the ends of the waveguide. A tunable laser scans its wavelength stepwise across the optical resonance to determine the optical quality factor. The waveguide position is tuned by changing the DC bias between the MEMS shuttle and the drive combs.

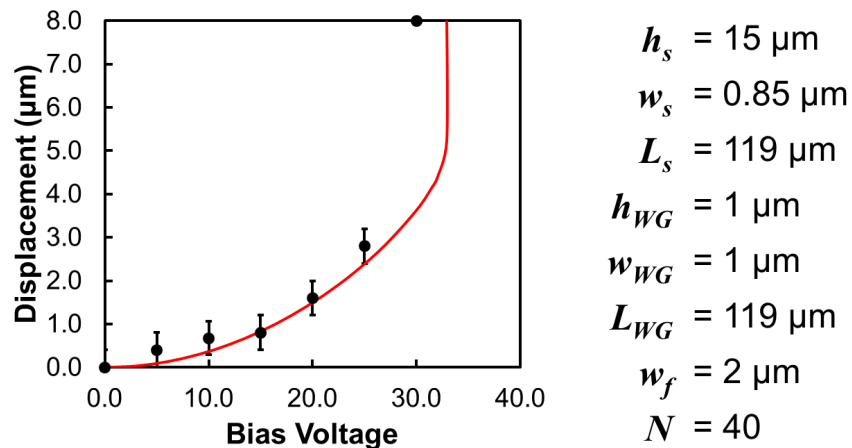


Figure 5.9: Experimental measurements of the displacement with respect to voltage of a MEMS comb drive actuator designed for the tunable-bandwidth filter. The theoretical displacement curve (red line) is calculated from the theory presented in Section 5.2.1. The values used for the theoretical calculation are shown to the right. Of course, due to fabrication variation, these values may not exactly correspond to those of the fabricated device.

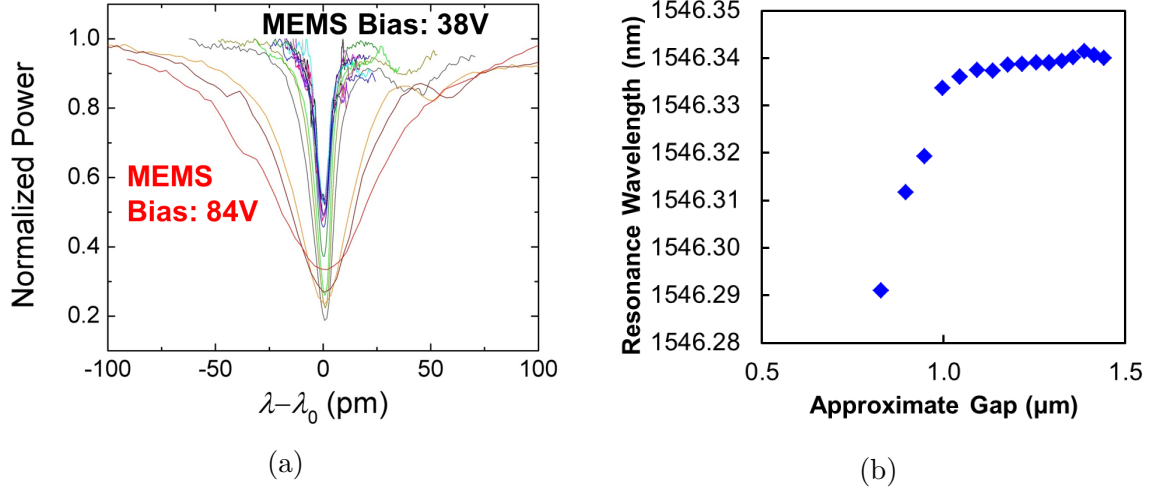


Figure 5.10: Measured optical resonance changes in a MEMS-actuated PSG tunable-bandwidth optical notch filter. (a) Spectra of a single optical resonance as the waveguide-resonator coupling gap is tuned. The widest resonance was for an applied bias of 84 V, and the narrowest was for an applied bias of 38 V. A larger bias results in a smaller coupling gap. For the narrower resonances, a resonance doublet is discernable. (b) The resonance wavelength shifted as the waveguide was moved. For smaller coupling gaps, the resonance wavelength was shorter. As the waveguide was moved away, the resonance wavelength increased, approaching the unloaded λ_0 of the cavity. The coupling gap here was approximated by fitting to the theory presented in Section 2.2.3.

optical resonances. Increasing the bias pulled the waveguide closer to the resonator, and we observed coupling from the undercoupled to overcoupled regimes. The resonance was a doublet, indicating that some scattering site within the resonator scattered some of the light into the counter-propagating mode, as described in Section 4.4.1.

The measured intrinsic quality factor was 8×10^5 , and the loaded Q_{opt} with the waveguide at its closest measured position was 2×10^4 . This corresponded to a 3 dB-bandwidth tuning range of 0.8 GHz to 8.5 GHz (7 pm to 68 pm). The resonance spectra as the bias was changed are shown in Figure 5.10a. As described in Section 2.2.3, we did observe a resonance shift due to the presence of the optical waveguide, shown in Figure 5.10b.

The measured loaded Q_{opt} and normalized power at the resonance wavelength are graphed in Figure 5.11 with respect to both the applied voltage and approximate displacement. The displacement was approximated by fitting the theory presented in Section 2.2.3 to the data, where an additional, constant loss mechanism τ_{other} was included to approximate other loss mechanisms, such as scattering in the coupling region. The other fit parameters were the initial gap between the waveguide and the resonator g_0 and the ratio between displacement and V^2 (this disregards parallel-plate effects). The approximate best fit was found for $\tau_{other} = 5$ ns, $g_0 = 1.6$ μm , and a displacement ratio of 0.11 nm/ V^2 . The resultant fit of the loaded Q_{opt} is not very good, in this case, because this was a resonance doublet. Thus, while the two adjacent resonances overlapped too much to be differentiated, a Lorentzian fit of the data had to include both resonances simultaneously, yielding an artificially low

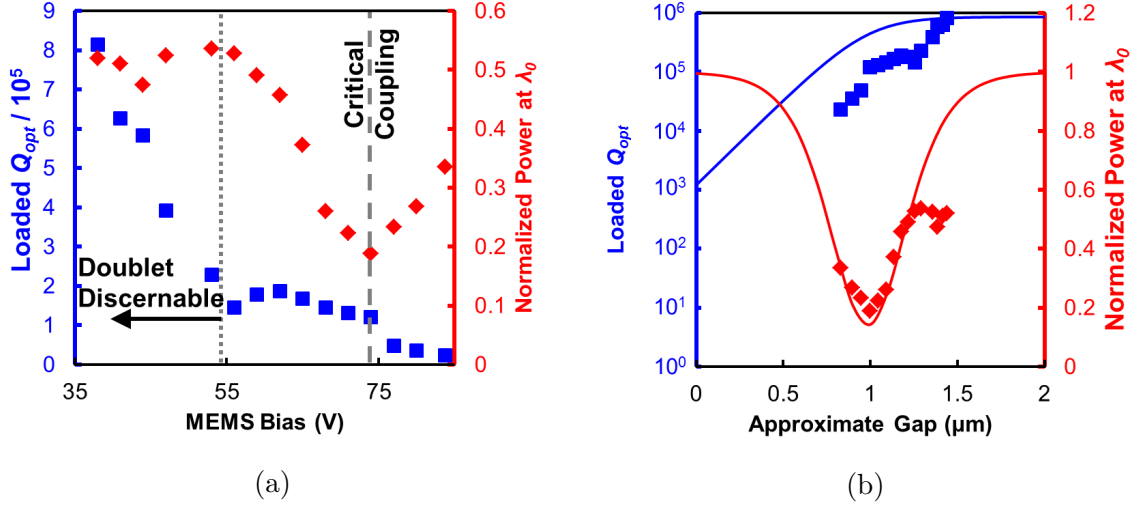


Figure 5.11: Tracking of the measured loaded Q_{opt} and normalized minimum power in an optical resonance as the waveguide position was tuned. (a) Filter behavior with respect to the DC bias applied between the MEMS shuttle and the drive comb. Below a bias of about 55 V, the doublet resonance was undercoupled enough that the two resonances could be differentiated; for larger biasing, the resonances overlapped too much to distinguish between them. As a result, the Lorentzian fit of the data fits both resonances simultaneously and yields an artificially low Q_{opt} . (b) Tuning behavior with respect to the approximate gap between the waveguide and resonator, obtained by fitting to the theory presented in Section 2.2.3. The quality factor data does not appear to fit well because the measured Q_{opt} , when the two resonances of the doublet were indistinguishable, was artificially low. Also, for larger coupling gaps, the normalized power does not fit well. This is likely a consequence of the compressive stress in the waveguide, which causes the relationship between displacement and voltage to deviate from theory at the extremes of the positional tuning range.

Q_{opt} . A camera could not be used to determine a more exact displacement value because the displacement was too small to determine precisely. Based on these graphs, it is clear that the waveguide positional tuning enabled coupling to the resonator from the overcoupled regime all the way to the undercoupled regime.

5.4 Comparison to Previous Work and Outlook

The tunable bandwidth filter presented in this work demonstrated a tuning range of 0.8 to 8.5 GHz, and the lower end of this range is less than one third of what has previously been demonstrated. [16] This narrow bandwidth was enabled by the high- Q_{opt} PSG resonator, which we measured to have an intrinsic Q_{opt} of approximately 8×10^5 . As presented in Chapter 4, PSG resonators are capable of much higher Q_{opt} up to 15 million, which would correspond to a minimum bandwidth of 13 MHz (0.1 pm), but the additional processing necessary to fabricate the MEMS actuator degraded the resonator Q_{opt} in this case. Thus, with some additional process refinement, it is possible to achieve an even smaller minimum bandwidth.

With the fabrication process presented in this chapter, further functionality could be added to the tunable filter. Adding a second tunable waveguide coupling to the resonator would enable not only tunable notch filtering, but also tunable band-pass filtering. Simultaneously tuning the optical resonance wavelength is another desirable function. In silicon, this can be done via carrier injection and thermal tuning, but the insulating properties of PSG inhibits these techniques. Resonance tuning in PSG could instead be accomplished using MEMS actuators. This has been previously accomplished by adding another ring or disk close above the main optical cavity and using MEMS actuators to change the gap between the two structures, thus tuning the optical resonator's effective index. [1] The fabrication technique we have demonstrated makes these and other functionalities possible, making it a good platform for integrating MEMS with high- Q_{opt} phosphosilicate glass photonic circuits.

Chapter 6

Single-Material Optomechanical Oscillators

As described in Chapter 3, the interaction between optical and mechanical resonant modes is enhanced when implemented in high- Q cavities. The two main mechanisms that can couple these two modes are the optical gradient force, in which the optical and mechanical modes are in different structures, and the radiation pressure force, in which the optical cavity also resonates mechanically. We will be focusing on radiation-pressure (RP) induced cavity optomechanics.

Though it is a relatively new field of study, cavity optomechanical devices have already shown potential for applications in quantum studies, [80] sensing, [11, 39] and optical signal manipulation. [72, 81] When RP-induced cavity optomechanical systems are driven in the amplification (blue-detuned) regime, with input power above the threshold for self-oscillation, the optical gain cancels out the intrinsic mechanical loss. This phenomenon can be exploited to create all-optical reference oscillators, [7, 82] the application we focused on. As stability is a crucial feature of a reference oscillator, we aimed to produce low-phase-noise optomechanical oscillators.

6.1 Previous Work

As discussed in Chapter 3, high Q_{opt} is important for achieving low threshold power P_{th} in cavity optomechanical systems, but it can degrade the phase noise if the Q_{opt} is too high. Another important parameter to consider is the mechanical quality factor Q_{mech} , which is the dominant parameter with regards to phase noise. The key performance metrics of several examples of RP-induced optomechanical devices are presented in Table 6.1, with the more notable examples described in the following text. Note that, to date, most studies of optomechanical devices have been in the cooling (red-detuned) or subthreshold regimes, so few devices have reported phase noise performance.

One structure that couples radiation pressure from an optical mode with mechanical motion is the photonic crystal “zipper” cavity. [42] In this case, two parallel, suspended photonic crystal Si_3N_4 beams form a photonic crystal optical cavity. When optical power builds up within the cavity, it exerts radiation pressure on the beams, changing the distance between

Table 6.1: Key performance metrics of integrated radiation-pressure-induced cavity optomechanical devices

Ref.	Structure	Material	Q_{opt}	Q_{mech}	$\Omega_{mech}/2\pi$	P_{th}	Phase Noise @ 1 kHz
[7]	microtoroid	SiO ₂	5.5×10^6	2×10^3 @ atm	217 MHz	250 μ W	-60 dBc/Hz
[25]	ring- microtoroid	SiO ₂	5×10^7	3×10^4 @ vac	38 MHz	*	N/A
[42]	photonic crystal	Si ₃ N ₄	$10^4 - 10^5$	50 - 150	8 - 140 MHz	*	N/A
[83]	disk	GaAs	1×10^5	10 - 10^3 @ atm	100 MHz - 1 GHz	*	N/A
[84]	ring	Si	5×10^5	4×10^3 @ atm	1.35 GHz	*	N/A
[8]	ring	Si ₃ N ₄	3×10^5	2×10^3 @ atm	42 MHz	*	-85 dBc/Hz
[85]	disk	Si	3.5×10^5	3.3×10^3 @ atm	1.29 GHz	3.56 μ W	N/A
[86]	disk	Si	7×10^4	4.4×10^3 @ atm	1.47 GHz	*	N/A
[87]	disk	GaP	2.8×10^5	500	500 MHz	approx. 100 μ W	N/A

*Not explicitly measured

them and thereby changing the optical resonant wavelength of the cavity. This structure has the advantages of small effective mass and large optomechanical coupling constant (meaning very small movements result in very large shifts in the optical mode), which contribute to low P_{th} . The Q_{opt} of this device ranges from 10^4 to 10^5 , and the Q_{mech} is an unremarkable 50-150 in air at a $\Omega_{mech}/2\pi$ around 8 MHz. With regards to fabrication, this device has the disadvantage that the photonic crystal and gap between the beams require very small critical dimensions around 60-250 nm. Thus, e-beam lithography is required. This device has not been demonstrated as a optomechanical oscillator, but given the very low Q_{mech} , its phase noise is likely very poor.

Optomechanical oscillations have also been demonstrated in silica microtoroids, described in Chapter 4. This type of device can achieve ultra-high $Q_{opt} > 10^8$, but the demonstrated Q_{mech} is typically on the order of 2000 in air. The resultant phase noise of such devices has been shown to be about -60 dBc/Hz at a $\Omega_m/2\pi$ around 54 MHz. [7]

In silicon, cavity optomechanical devices have generally been implemented in microring/disk structures. To date, none have been thoroughly studied in the blue-detuned amplification regime, but existing demonstrations offer some promise, especially in high-frequency applications. One example has a reasonably high Q_{opt} of 0.5 million and a mechanical frequency over a GHz. The measured Q_{mech} is 4000, measured in air. [84] This is a reasonably high Q_{mech} for a measurement at atmosphere, implying it is possible that the Q_{mech} , and therefore the phase noise performance, under vacuum may be quite good. However, we know of no existing examples of RP-induced optomechanical oscillators characterized in vacuum.

Silicon nitride has proven to be a useful optomechanical material, with several examples of Si_3N_4 microrings and disks in the literature. [8, 72, 88] In particular, [8] explores the use of a Si_3N_4 spoke-supported ring as an optomechanical oscillator. Outside of our devices, to be described later in the chapter, this has had the best reported phase noise performance among optomechanical oscillators, with a phase noise power of -85 dBc/Hz at 1 kHz offset from a 42 MHz carrier (Q_{mech} of 2000 measured in air). The $Q_{opt} > 3 \times 10^5$ is sufficiently high for achieving parametric amplification.

Optomechanical devices have also been fabricated in various other materials, including GaAs and GaP disks. [83, 87] These show some promise for high-frequency applications, but to-date demonstrated devices have had $Q_{mech} < 1000$, so their phase noise performance may be degraded, though that has not yet been characterized. For details, see Table 6.1.

6.2 Device Design

We investigated the different factors that affect phase noise performance in optomechanical oscillators (OMOs) in order to optimize OMO performance. Based on the theory outlined in Chapter 3, OMO phase noise is shaped by the Q_{mech} , so we aimed for higher Q_{mech} . Mechanical losses that contribute to Q_{mech} include environmental factors, device geometry, and intrinsic material properties. [89] Most environmental factors, such as air damping, can be addressed in the measurement set-up. Geometry design and intrinsic material properties will be discussed in the next sections.

Another important device characteristic is the threshold power for optomechanical oscillation P_{th} , which is proportional to $1/(Q_{opt})^3$. Because of this strong dependence on Q_{opt} , if

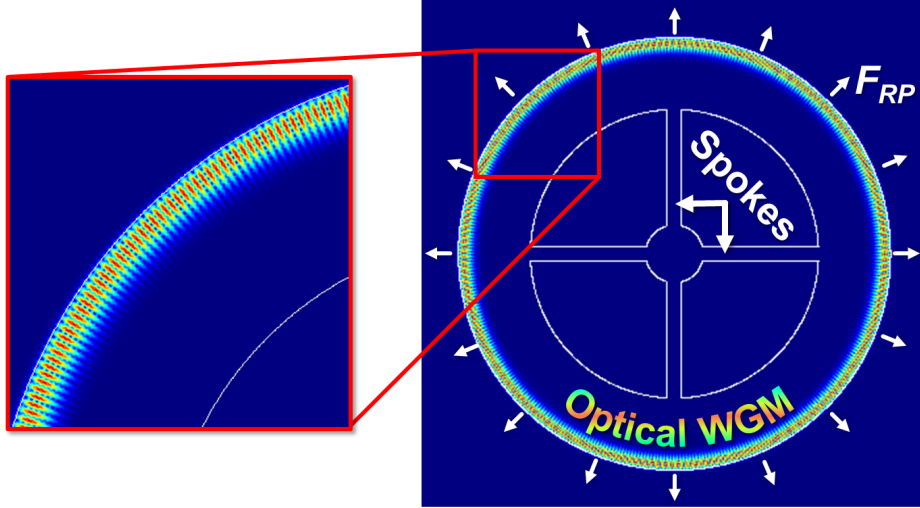


Figure 6.1: FEM simulation of one of the optical whispering-gallery modes of a spoke-supported ring. Ring shape is indicated with white lines, and color shading shows relative electric field magnitude. Since the optical mode is radially symmetric, radiation pressure force F_{RP} is also radially symmetric.

it is too low, P_{th} will be inaccessibly high. At the same time, a very high Q_{opt} can degrade phase noise performance, as discussed in Chapter 3. Knowing this, we considered both device geometry and various materials to find the right balance between the constraints on Q_{opt} .

6.2.1 Geometry

The resonator geometry we chose was the “spoke-supported ring,” shown in Figure 6.1. Rings are well-known as an optical resonator geometry, and this same geometry has been successfully used to create mechanical-only resonators with high Q . [90] Optically, for rings having width $\gg \lambda$, the modes are essentially only confined by the outer edge of the ring. Thus, they are whispering gallery modes, described in Chapter 2, and we can tune the free spectral range and optical bending loss by changing the radius.

Mechanically, spoke-supported rings support a wide range of modes, including out-of-plane modes. For the purposes of an optomechanical resonator, however, the important mechanical modes are those that are most strongly coupled to the radiation pressure force of the optical mode. The radiation pressure force pushes symmetrically outward in the \hat{r} direction, as shown in Figure 6.1, most strongly selecting modes that uniformly change the device radius without out-of-plane motion. Some of these modes are shown in Figure 6.2. Because the optomechanical oscillator’s $P_{th} \propto (Q_{mech})^{-1}$, the fundamental mode, also known as the breathing mode, is most likely to self-excite, since its Ω_m is much less than next lowest frequency, in the second-order mode (Figure 6.2b). In a ring mechanical resonator, the radially-symmetric modes are defined by the following two equations [91]:

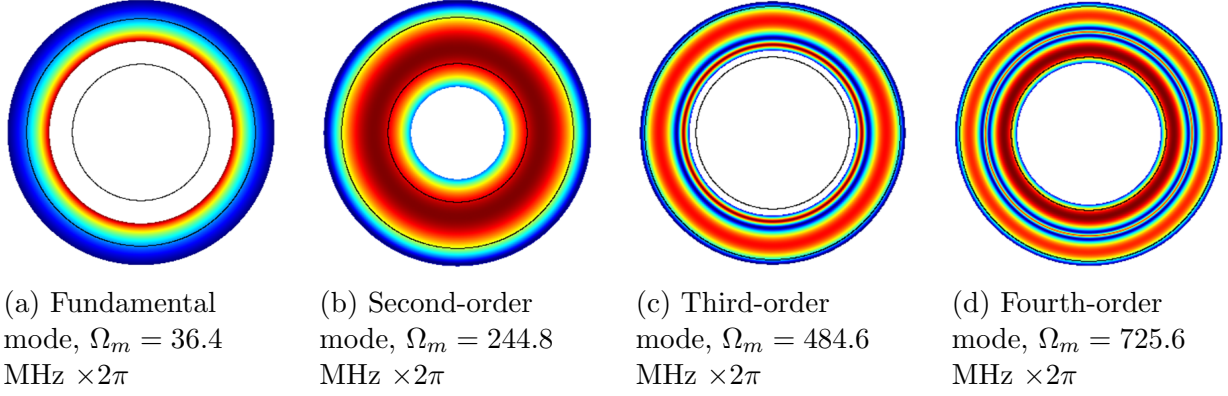


Figure 6.2: FEM simulation of some mechanical eigenmodes of a Si ring having $R_o = 50$ μm and $R_i = 30$ μm . Initial ring shape is indicated with black lines, and color shading indicates stress in device.

$$\frac{pr_o Y_0(pr_o) - (1 - \nu)Y_1(pr_o)}{pr_o J_0(pr_o) - (1 - \nu)J_1(pr_o)} = \frac{pr_i Y_0(pr_i) - (1 - \nu)Y_1(pr_i)}{pr_i J_0(pr_i) - (1 - \nu)J_1(pr_i)} \quad (6.1a)$$

$$\Omega_m = p \sqrt{\frac{E}{(1 - \nu^2)\rho}} \quad (6.1b)$$

Here, r_o is the ring's outer radius, r_i is the ring's inner radius, E is the Young's modulus of the ring material, ν is the Poisson's ratio, ρ is the material density, J_ℓ are Bessel functions of the first kind, and Y_ℓ are Bessel functions of the second kind. Of course, the presence of the spokes in the ring perturbs the mode somewhat, so the actual spoke-supported ring Ω_m will be somewhat different than predicted by Eq. 6.1. By modifying the spoke design, we can minimize this perturbation and reduce anchor loss to maximize Q_{mech} . Loss to the anchor is minimized by designing the spokes to be an odd multiple of one quarter of the acoustic wavelength. [90] The quarter-wavelength spoke length is dependent on the Young's modulus E , the material density ρ , and the mechanical frequency $f_0 = \Omega_m/2\pi$:

$$L_{\text{spoke}} = \frac{m\sqrt{E/\rho}}{4f_0} \quad m = 1, 3, 5... \quad (6.2)$$

Since, in reality, the ends of the spoke are not perfectly clamped, this is only an approximation of the best spoke length for a ring. We can use this number as a starting point for finite-element modeling to determine the best spoke length.

However, the fundamental radially-symmetric mode's frequency is too low to fit a quarter-wavelength support within the inner radius of a ring. Instead, we used FEM to see how changing the spoke width and length affects the fundamental mode shape and frequency, as shown in Figure 6.3. From this, we can see that longer, thinner spokes result in a less-perturbed fundamental mode than shorter or thicker ones.

Unlike the fundamental mode, the second-order radially-symmetric mode's frequency is high enough that a quarter-wavelength support does fit within the inner radius of a ring.

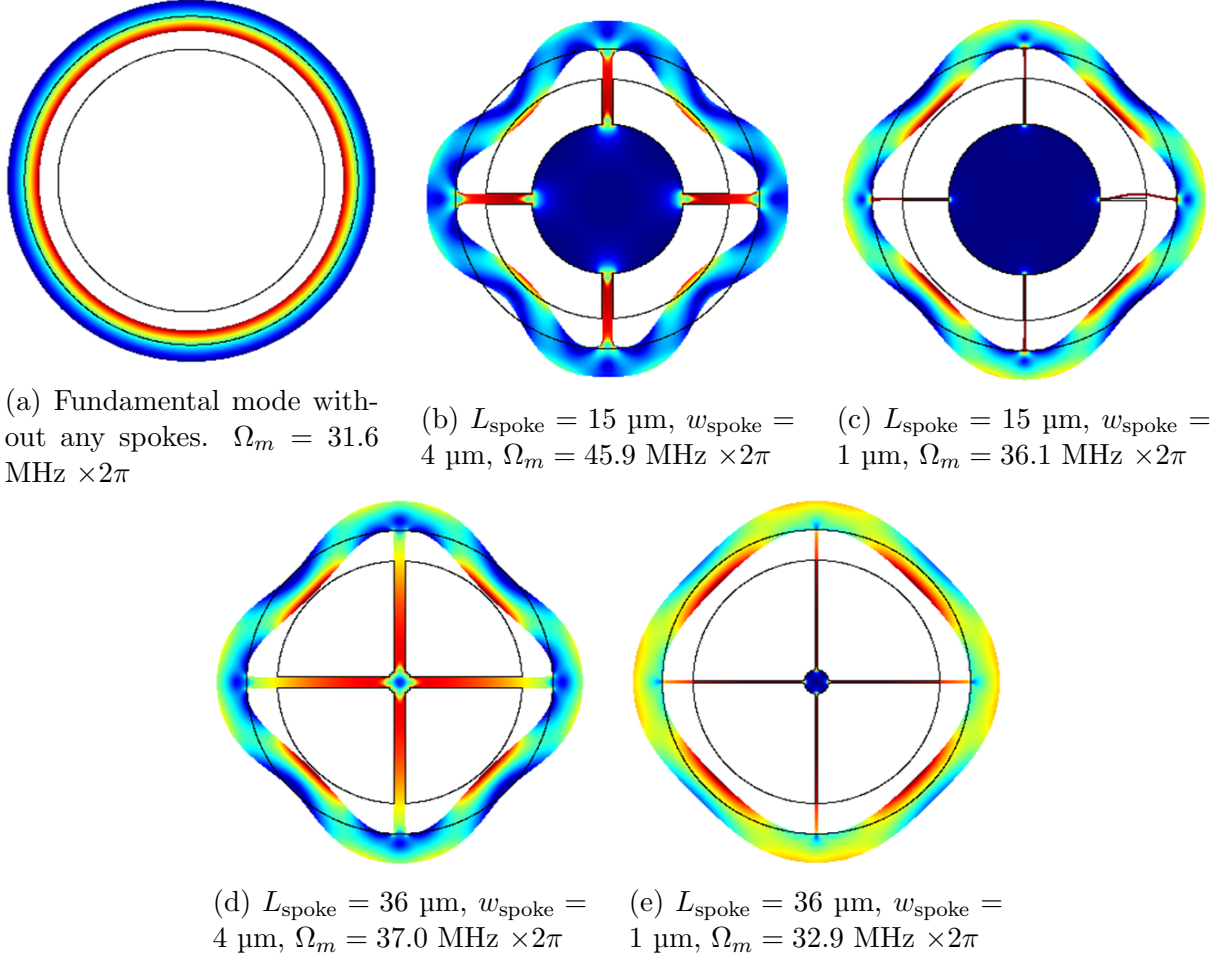


Figure 6.3: FEM simulation of the fundamental radially-symmetric mode of a Si spoke-supported ring having $R_o = 50 \text{ } \mu\text{m}$ and $R_i = 40 \text{ } \mu\text{m}$. Initial ring shape is indicated with black lines, and color shading indicates stress in device. The amount of perturbation of a ring's mode can be quantified by comparing its mechanical frequency to that of the ring without spokes.

Figure 6.4 shows the dramatic effect on the second-order mode of a quarter-wavelength support compared to a long, thin support, which is the ideal support for the fundamental mode. Based on this, it is clear that each device must be designed specifically for the target mode to maximize Q_{mech} .

A couple of other things to consider for minimizing loss in the spoke-supported ring geometry are the number of spokes and the anchor design. If we compare the simulated film stress at the center of a four-spoke and two-spoke ring, shown in Figure 6.5, we see that the four-spoke design does a much better job of cancelling out the forces at the center than the two-spoke design. This means that less acoustic energy will be able to leak from the central anchor in a four-spoke device. We will later experimentally demonstrate that this difference is important, as four-spoke rings consistently have higher Q_{mech} than do two-spoke rings.

Regarding anchors, ideally, the ring's anchor would be small and placed directly at the

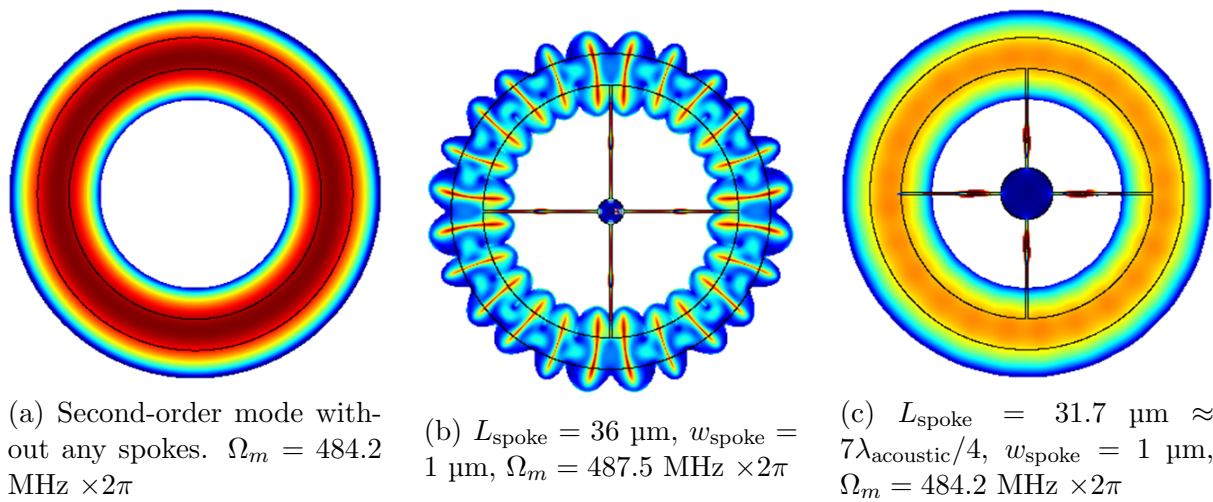


Figure 6.4: FEM simulation of the second-order radially-symmetric mechanical mode of a Si spoke-supported ring having $R_o = 50 \text{ }\mu\text{m}$ and $R_i = 40 \text{ }\mu\text{m}$. Initial ring shape is indicated with black lines, and color shading indicates stress in device. The amount of perturbation of a ring's mode can be quantified by comparing its mechanical frequency to that of the ring without spokes.

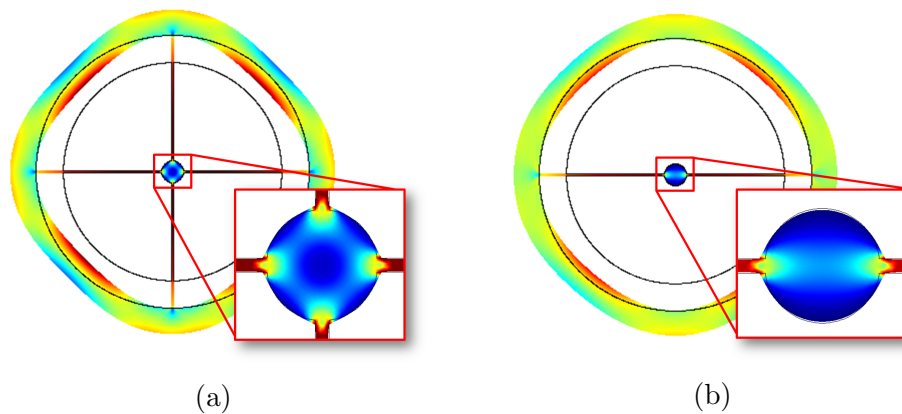


Figure 6.5: Comparison of stress exerted on center anchor by four- and two-spoke resonators

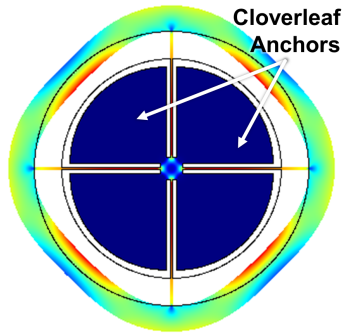


Figure 6.6: FEM simulation of the fundamental radially-symmetric mechanical mode of a Si spoke-supported ring having $R_o = 50 \mu\text{m}$ and $R_i = 40 \mu\text{m}$, and anchored as via a “cloverleaf” anchor design. Initial ring shape is indicated with black lines, and color shading indicates stress in device.

zero-stress node at the center (Figure 6.5a) for minimum acoustic loss to the anchor. However, for some fabrication processes, we did not include an anchor, instead relying on a timed release. This requires an anchor modification so that some sacrificial material still remains to keep the ring attached, but released. We chose a cloverleaf anchor design, simulated in Figure 6.6.

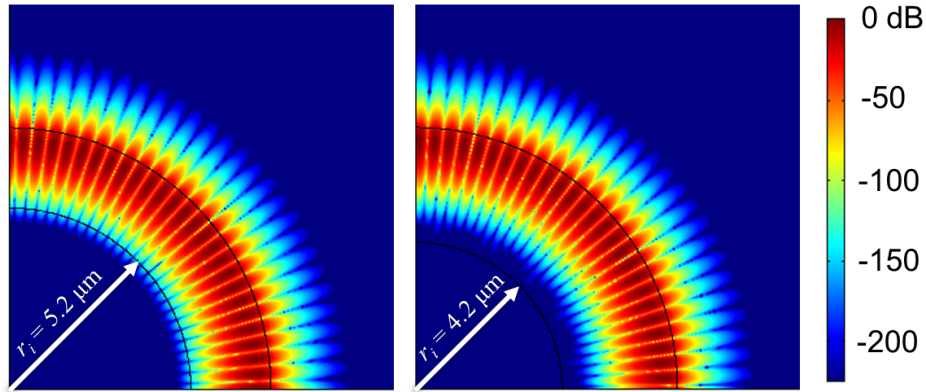
Now, we started out assuming that the optical mode was only confined by the outer edge of the ring, but it requires careful design to ensure that the optical mode does not overlap the inner edge of the ring, as well. If the ring is too narrow, the spokes attached to the inside of the ring will scatter the light, degrading the Q_{opt} , but if the ring is too wide, the mechanical frequency will increase, approaching that of a disk, thereby increasing the threshold power for optomechanical oscillation. In addition, a too-wide ring will eliminate the area available in the center for cloverleaf anchors, which are necessary for a timed release of the device. We used finite-element modeling (Figure 6.7a) to choose a ring width just wide enough to avoid scattering off the inner ring edge and spokes. Figure 6.7b shows the chosen ring widths with respect to outer radius.

6.2.2 Materials

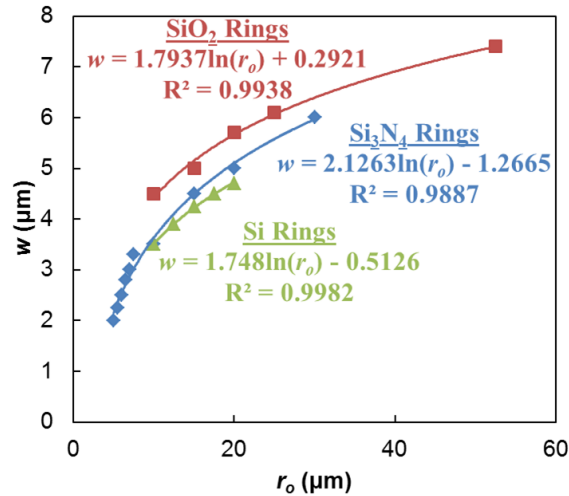
Device material choice has an effect on both mechanical and optical Q , so we looked at a range of materials with different optical and mechanical characteristics. Specifically, we chose phosphosilicate glass (PSG), silicon, and stoichiometric Si_3N_4 . Optical characteristics of these materials are already listed in Table 4.1, and important mechanical properties are shown in Table 6.2.

For optomechanical oscillators, both intrinsic optical material loss and index of refraction are important. If the optical absorption of a material is too high, the Q_{opt} will be degraded, and the threshold power for self-oscillation will be very high. Consequently, polycrystalline materials, though possessing high Q_{mech} , are not a viable option for OMOs, since the many crystal grain boundaries scatter light out of the optical mode and degrade Q_{opt} significantly.

Index of refraction is important when considering device size, and therefore, mechanical



(a) Two FEM simulations of optical WGM in a Si_3N_4 ring with outer radius $r_o = 7.5 \mu\text{m}$. On the left, the inner radius is $r_i = 5.2 \mu\text{m}$, and the optical mode clearly overlaps with the inner edge of the ring. The chosen design is on the right, where $r_i = 4.2 \mu\text{m}$, and the optical mode is well-separated from the inner edge of the ring, minimizing scattering.



(b) Designed ring widths in SiO_2 , Si_3N_4 , and Si with respect to outer radius, as chosen using FEM simulation. The points are the actual designs, and lines are logarithmic fits of these designs.

Figure 6.7: Choosing optical ring widths using finite-element modeling

Table 6.2: Important material parameters of SiO₂, Si, and Si₃N₄

	SiO ₂	Si	Si ₃ N ₄
Young's Modulus E (GPa)	70	170	250
Density ρ (kg/m ³)	2200	2330	3100
Poisson's Ratio ν	0.17	0.28	0.23
Linear Coefficient of Thermal Expansion α_L (ppm/K)	0.5	2.6	3
Heat Capacity c_p (J/(kg K))	730	700	710
Thermal Conductivity κ (W/(m K))	1.4	150	30

frequency Ω_m . A high index of refraction means that the optical mode will be more confined, so bending loss will be small for smaller radii of curvature than for a material with a low index of refraction. Of course, for a mechanical disk or ring resonator, a smaller radius results in a higher frequency. Thus, in OMOs, a material's refractive index places a constraint on the achievable Ω_m .

Mechanically, material loss can come from surface, bulk, and thermal effects. [92] Within each of these categories, there are a large number of potential material-specific loss mechanisms. Loss mechanisms at the surface can be both morphological (such as roughness [89] and contamination [93]) and atomic-scale (such as termination of the atomic lattice [93]). Bulk effects can include, but are not limited to, material defects, phonon-phonon scattering, and tunneling of atoms. [93] Thermoelastic dissipation (TED) is a result of stress-induced temperature differences, which result in energy loss due to heat flow, and it is dependent on the resonator material's thermal and mechanical properties, as well as the device geometry and mechanical frequency. [94] Since the interplay between each of these loss mechanisms is complex and dependent on both intrinsic material properties and device design, material-limited quality factors have generally been determined empirically.

PSG, as described in Chapter 4, can achieve high Q_{opt} , up to about 15 million, so very low optomechanical P_{th} is achievable. However, it has a low refractive index, so PSG cannot achieve Ω_m as high as other, higher-index materials. (In higher-index materials, the ring can be made smaller without incurring as much optical loss, so a higher Ω_m is possible.) In addition, silica, as an amorphous solid, is known to undergo atomic tunneling, which contributes to the degradation of Q_{mech} . [95]

In contrast, single-crystal Si has been demonstrated to have very high Q_{mech} (4×10^4 at 150 MHz) in disk modes. [96] Si also has a high refractive index, which means it could have high Ω_m in disk/ring mechanical modes. It also can have reasonably low optical loss with low doping (see Table 4.1), but its small band gap of 1.11 eV makes two-photon absorption a significant optical loss mechanism at infrared wavelengths and high optical powers. Thus, if a Si OMO requires a lot of power to reach oscillation, two-photon absorption will become an important optical loss mechanism.

Si₃N₄ has a large band gap (5 eV), so two-photon absorption at infrared wavelengths is not a problem, but its intrinsic material absorption is somewhat higher than silicon's. At

the same time, its refractive index falls between that of PSG and that of Si, so its minimum bending radius is larger than that of silicon but smaller than that of PSG. Thus, the Ω_m that can be achieved in a Si_3N_4 disk/ring will fall somewhere between the other materials. Finally, the tensile strain inherent to stoichiometric Si_3N_4 has enabled very high Q_{mech} (approx. 100k at 10 MHz) in clamp-clamp beam mechanical resonator architectures, [97] but it is not clear whether this low phononic loss would translate to high Q_{mech} in ring/disk resonators. Thus, Si_3N_4 is, in many ways, a middle ground between PSG and Si with regards to the parameters contributing to OMO phase noise.

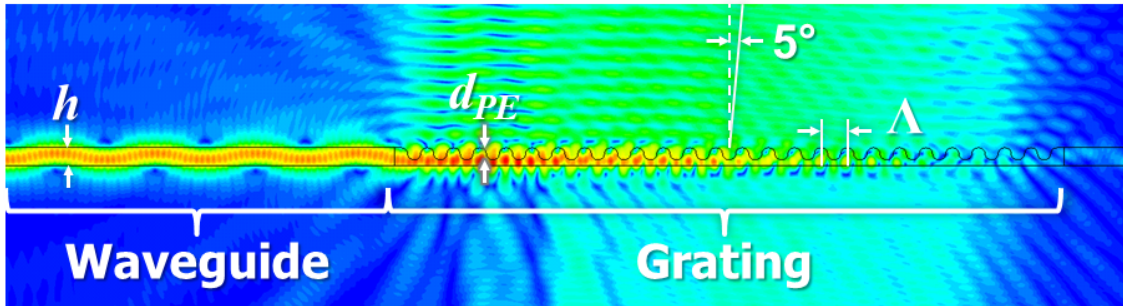
6.2.3 Layout

The layout of the devices depended on the desired method of measurement. For a tapered-fiber measurement, in which evanescent coupling to the resonator is accomplished via an optical fiber mounted on a separate micropositioning stage, the layout was simply a resonator with enough space around it to accommodate the tapered fiber. This will be referred to as a “stand-alone” device.

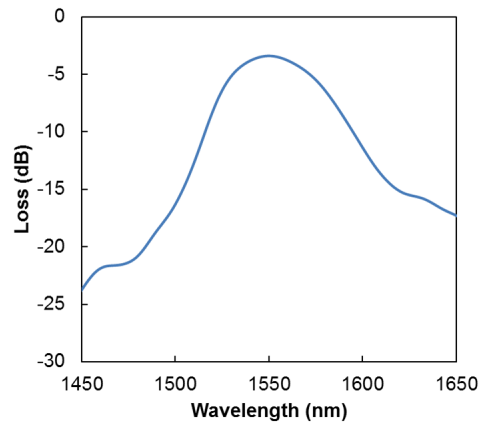
For the PSG devices, we also included layouts with integrated, side-supported waveguides, shown in Figure 4.2. The side-supported waveguides were fixed with respect to the resonators, so in order to have the right coupling distance between the waveguide and resonator, we made an array of these with varying coupling distance (see Figure 4.11a). Thus, we could “tune” the correct coupling distance by measuring various devices with different waveguide-resonator gaps and choosing the best one. For these devices, light could be coupled to the waveguide either by edge coupling or grating coupling.

For edge coupling, we simply diced perpendicular to the waveguides to form facets, and the input and output facets were coupled to lensed fibers mounted on two separate micropositioning stages (see Figure 4.11b). Edge coupling has the advantage of low insertion loss (~ 11 dB), and easier packaging for measurement in vacuum than grating couplers. However, the alignment must be more accurate and precise than for vertical grating couplers, requiring very stable stages.

Unlike edge couplers, vertical grating couplers do not require as much alignment accuracy, and they can be accessed on a wafer scale. However, creating an efficient grating coupler in PSG is particularly challenging because of the low index of refraction. In addition, during the reflow process, the grating will also be smoothed and rounded, changing the characteristics of the grating. We performed FDTD simulations to determine the best grating period Λ , film thickness h , etch depth d_{PE} , and input angle for a first-order grating coupler with the electric field polarized parallel to the grating. The simulations were performed with the cross-sectional geometry approximating the post-reflow grating shape. The best design for an optical wavelength of 1550 nm, simulated in Figure 6.8a, had $\Lambda = 1.355 \mu\text{m}$, $h = 900$ nm, $d_{PE} = 613$ nm, and an input angle of about 5° . The simulation predicts a coupling loss of about 3.4 dB, and the grating spectrum is shown in Figure 6.8b.



(a) Contour plot on a log scale of simulated electric field in grating coupler and waveguide.



(b) Simulated grating loss with respect to input wavelength.

Figure 6.8: Two-dimensional FDTD simulation of final grating design at $\lambda = 1550$ nm. Here, $h = 900$ nm, $d_{PE} = 613$ nm, $\Lambda = 1.355$ μ m, and the angle of incidence is 5° .

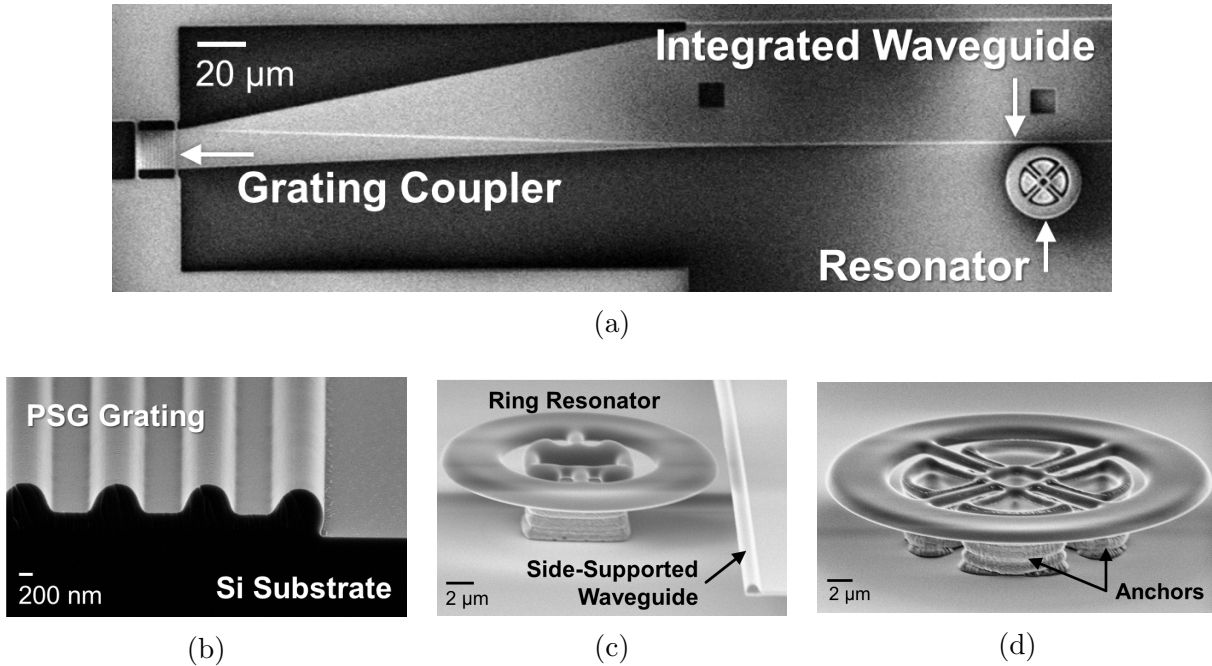


Figure 6.9: SEMs of fabricated PSG optomechanical devices. (a) A wide-angle view showing PSG resonator with integrated waveguide tapering to vertical grating coupler. (b) Cross-section of grating coupler, showing post-reflow shape of grating. (c) An anchored PSG resonator coupling to side-supported waveguide. (d) An anchored PSG stand-alone resonator.

6.3 Fabrication

The fabrication process for these devices was fairly simple, with only slight variations for each material type. The full fabrication process for PSG devices, including anchors, gratings, and side-supported waveguides, is described in Chapter 4 and shown in Figure 4.3. Some SEM images of the resultant devices are shown in Figure 6.9.

For silicon devices, we did not include integrated waveguides, so the process was similar but simpler than that of the PSG devices, and is shown in Figure 6.10. The main differences were the sacrificial layer, the device material, the sidewall treatment, and the release. The single-crystal Si devices were fabricated using SOI wafers with a couple of different device layer thicknesses. Poly-Si anchors were not fabricated in all Si devices; for those devices a timed release was necessary. Thinner devices (220 nm thick) were reactive-ion etched in HBr and Cl_2 transformer-coupled plasma with no additional sidewall treatment, but thicker devices ($> 1 \mu\text{m}$) also underwent a polishing process that consisted of three cycles of RCA cleaning, as outlined in [98]. Details on the results of this polishing process will be presented in Section 6.4.2. Devices were released either in HF followed by CPD or in vapor-phase HF. SEMs of the fabricated Si devices are shown in Figure 6.11.

For the stoichiometric Si_3N_4 devices, the sacrificial layer was at least 2 μm of low-pressure chemical-vapor-deposited (LPCVD) SiO_2 . The device material was approximately 400 nm LPCVD stoichiometric Si_3N_4 . The devices were reactive-ion etched with either CH_3F , O_2 , and Ar or CHF_3 and O_2 , both of which resulted in comparable device performance. Details

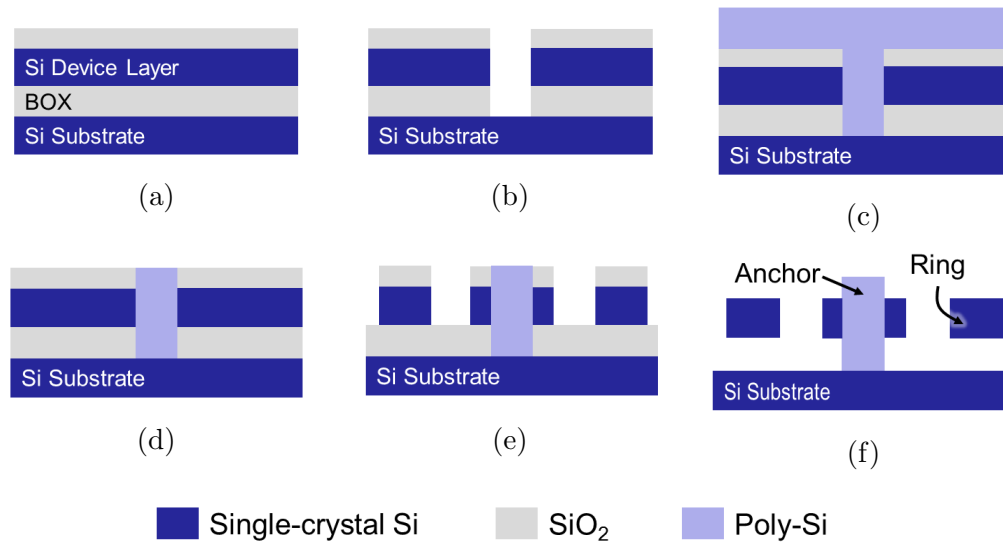


Figure 6.10: Fabrication process for stand-alone Si optomechanical resonators (a) Start with an SOI wafer and deposit SiO_2 hard mask (b) Pattern and etch anchors down to Si substrate (c) Deposit thick poly-Si to fill anchor holes (d) Blanket etch poly-Si down to SiO_2 layer, leaving anchor filled (e) In photoresist, pattern the device layer and etch through SiO_2 and Si device layer (f) Release in vapor-phase HF or in HF followed by CPD

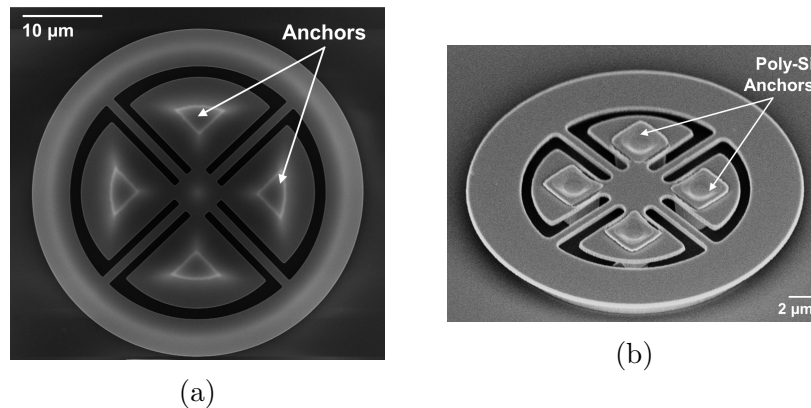


Figure 6.11: SEMs of stand-alone Si devices. (a) Top view of released thin (220 nm), 20 μm radius device. The small triangles in the middle of the “clover leaves” indicated where there is still sacrificial oxide attached to the underside following timed release. (b) Perspective view of released thick ($\approx 1 \mu\text{m}$), 15 μm radius device. This device is anchored with poly-Si.

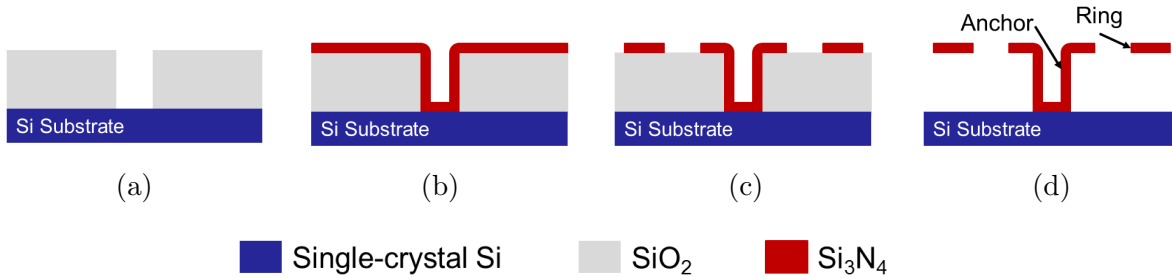


Figure 6.12: Fabrication process for stand-alone stoichiometric Si_3N_4 optomechanical resonators (a) Start with a plain Si wafer and deposit at least $2\ \mu\text{m}$ SiO_2 sacrificial layer, then pattern and etch anchors down to Si substrate (b) Deposit about $400\ \text{nm}$ Si_3N_4 (c) Pattern photoresist and RIE the Si_3N_4 device layer (d) Release in buffered HF followed by CPD

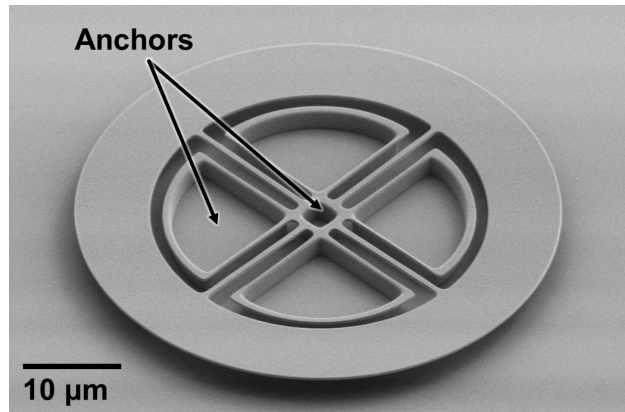


Figure 6.13: SEM of fabricated Si_3N_4 stand-alone resonator having $r_o = 25\ \mu\text{m}$, $r_i = 17\ \mu\text{m}$, and $L_{\text{spoke}} = 14.5\ \mu\text{m}$.

on these etch recipes are given in Appendix B. No additional processing was applied to reduce optical loss. Finally, the devices were released in buffered HF followed by a critical-point dry (CPD) to minimize stiction to the substrate. A fabricated device is shown in Figure 6.13.

6.4 Measurement

We characterized these devices using a variety of different techniques to determine their key parameters as optomechanical oscillators. Specifically, we measured intrinsic Q_{opt} , intrinsic Q_{mech} , threshold power P_{th} , and phase noise. In addition, we investigated the generation of higher-order optomechanical harmonics.

As previously mentioned, we measured all of our stand-alone devices using a tapered fiber mounted on a separate micropositioning stage (see Figure 6.14a). This measurement technique was compatible with measurements in both atmosphere and vacuum.

For the PSG devices with integrated waveguides, we measured using both edge and grat-

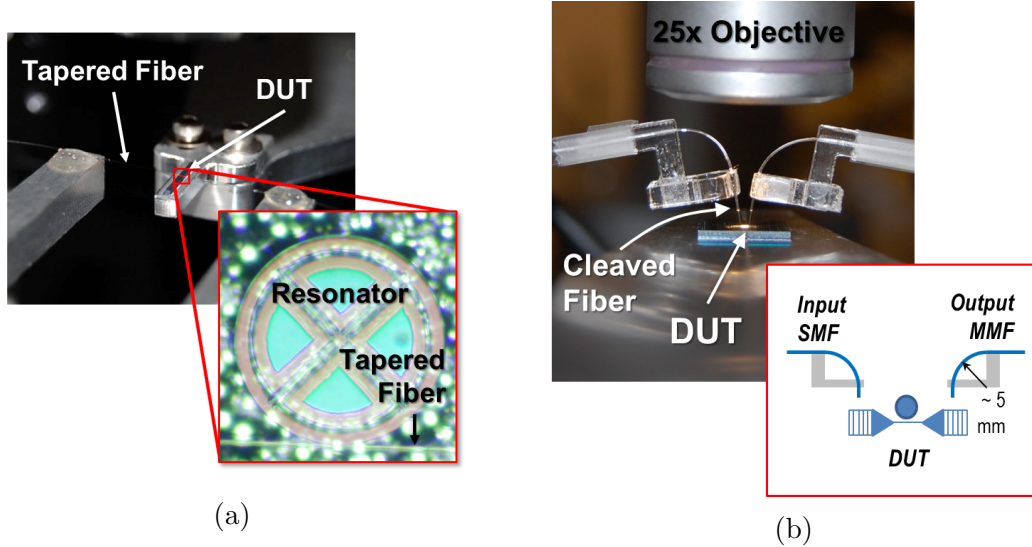


Figure 6.14: Optomechanical device measurement setups (a) Measuring stand-alone devices with a tapered fiber. Tapered fiber, mounted on a separate micropositioning stage, is stretched across the sample and aligned to the resonator. (b) Measuring devices with integrated waveguides and grating couplers. Cleaved ClearCurve[®] fibers are mounted on custom fixtures and tightly curved (radius of curvature ≈ 5 mm) so they can couple to gratings at the correct angle while fitting under the microscope objective.

ing coupling. Edge coupling, described in Section 6.2.3 of this chapter as well as in Chapter 4, was used for devices that were thicker than 900 nm, since thicker gratings exhibited much higher loss in both simulation and experiment.

Coupling to vertical grating couplers required some additional setup engineering in order to fit the input and output fibers under a microscope objective. A typical single-mode fiber has about 0.1 dB attenuation per 360° turn at a 50 mm radius for a wavelength of 1550 nm, but we wanted to be able to fit the input and output fibers under a microscope objective. As an example, a MicroZoom 25x long-working-distance objective has a working distance of 12.9 mm, which would require a radius of curvature of the optical fiber of less than that in order to fit under the objective. This would introduce a significant amount of loss. As a result, we used Corning's ClearCurve[®] optical fibers, which can tolerate curvature down to 5 mm with only 0.1 dB attenuation per 360° turn at a wavelength of 1550 nm. Using custom-made fixtures, we were able to fit the input and output cleaved fibers under the microscope objective, as shown in Figure 6.14b. With this arrangement, the fiber-to-fiber insertion loss we measured was typically about 15 dB.

The procedure we used for measuring intrinsic Q_{opt} is described in Section 4.4.

For combined optical and mechanical measurements, we added some components to our measurement setup, as shown in Figure 6.15. The optomechanical modulation of the optical signal was observed by taking the output optical signal, detecting it with a photodiode, and running the photodiode signal into an electrical spectrum analyzer (ESA).

Having added these components, we were able to measure the mechanical characteristics Ω_m and intrinsic Q_{mech} as well as the optomechanical characteristics P_{th} and phase noise

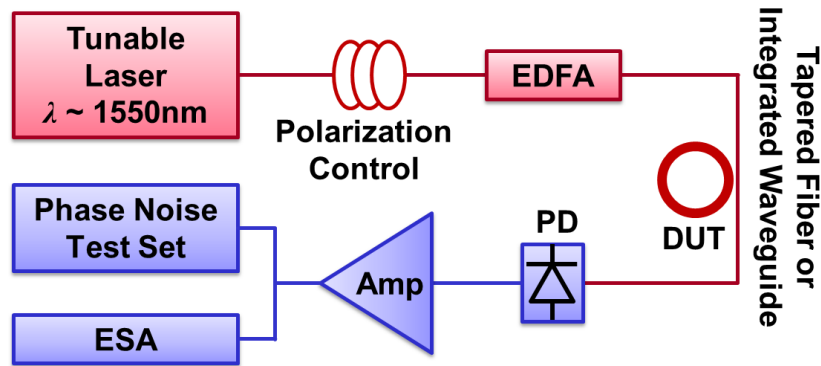


Figure 6.15: Measurement setup for optomechanical measurements. After coupling to the device under test (DUT) via either a tapered fiber or integrated waveguide, the optical signal is detected at the photodiode. The photodiode signal is amplified and sent either to an electrical spectrum analyzer (ESA) or the phase noise test set. Mechanical motion of the DUT is transduced to a modulation on the optical signal, which is seen as a resonance on the ESA. For devices with especially high threshold power P_{th} , an erbium-doped fiber amplifier (EDFA) is used to get enough power into the resonator to achieve self-oscillation.

performance. The mechanical characteristics were measured with low optical power to ensure that the device was not self-oscillating. In the self-oscillation regime, the effective Q_{mech} appears much higher than the device's intrinsic Q_{mech} because of dynamical backaction effects, but we wanted to know the purely mechanical characteristics of the device. With low enough input power, the resonances that are seen on the ESA are simply the optically-sensed Brownian motion of the device, and they should represent the intrinsic mechanical characteristics.

As input power is increased, the magnitude and effective Q_{mech} of the excited resonance slowly increase until the threshold power P_{th} is reached, at which point the rate of increase abruptly increases. By measuring the magnitude of the resonance peak power with respect to input power, we can find P_{th} for optomechanical oscillation, similar to finding the threshold voltage of a diode.

To measure phase noise, we send the signal from the photodetector into a phase noise test set instead of the ESA. The phase noise test set determines the amount of power in the signal with respect to frequency offset from the carrier. To do this, it first generates a very low noise reference signal with the frequency matched to the device resonance via a phase-locked loop. It beats this reference signal with the device resonance and detects the phase with a double-balanced mixer. Above 1 kHz offset, it sends the mixer's output to an ESA to construct the phase noise plot, while below 1 kHz offset, it uses an internal FFT analyzer to obtain a higher resolution phase noise spectrum. Phase noise is not only influenced by the intrinsic properties of the device, but also by the input power, laser detuning from the optical resonance, and coupling distance. For each phase noise measurement, we optimized these parameters to achieve the best possible phase noise for that device.

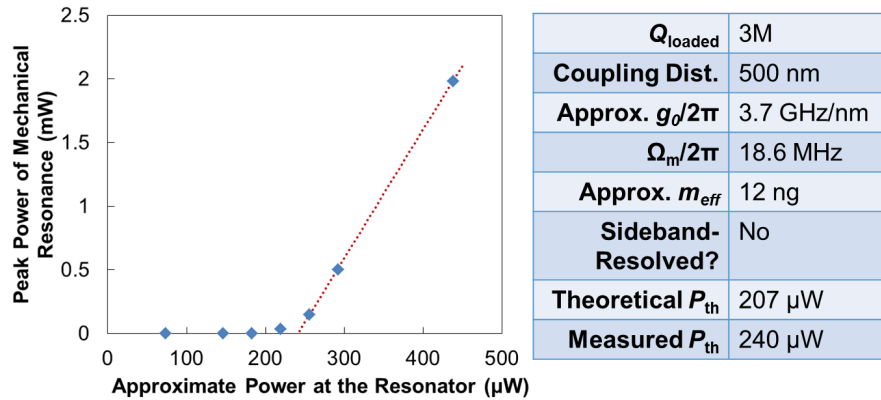


Figure 6.16: Example of a measurement of threshold power P_{th} in air of a two-spoke PSG resonator with $r_o = 52.5 \mu\text{m}$. Coupling to resonator was achieved via an integrated waveguide with edge-coupled lensed fibers. Based on the change in the mechanical resonance amplitude seen on the ESA with respect to input optical power, we estimate P_{th} to be about 240 μW , which is close to the theoretical approximation of P_{th} .

6.4.1 PSG Optomechanical Resonator Measurements

PSG optomechanical oscillators were measured as stand-alone devices and with integrated, side-supported waveguides. The stand-alone devices were measured in both air and vacuum. Measurements of the best intrinsic Q_{opt} are discussed in detail in Chapter 4. In summary, the highest demonstrated Q_{opt} in PSG is about 15 million in a 2 μm thick device with a 50 μm radius, but there are many different optical modes within a free spectral range, so we were able to investigate various Q_{opt} 's when measuring optomechanical performance within the same device.

Two- and four-spoke-supported rings with outer radii ranging from 10 to 50 μm were fabricated. The Q_{opt} of the smaller devices began to be limited by bending loss, and, as expected, each device size had a different fundamental Ω_m . For phase noise measurements and vacuum measurements, we focused on the largest devices. The observed threshold power P_{th} of these devices generally matched that predicted by Eq. 3.10. (All measured devices were in the non-sideband resolved regime.) An example of a P_{th} measurement in air via an integrated waveguide is shown in Figure 6.16.

In the PSG devices, the Q_{mech} of the fundamental radially-symmetric mode in air was consistently around 1000, but this increased when the devices were placed in vacuum, since the air damping was reduced. Thus, the effect of Q_{mech} on the phase noise of a single device could be shown. [82] Phase noise of a stand-alone PSG resonator in both air and vacuum is shown in Figure 6.17. We see that reducing the ambient pressure from 760 torr to 25 torr increases Q_{mech} from 1200 to 7200 and decreases phase noise at 1 kHz offset from the 18.6 MHz carrier from -80 dBc/Hz to -87 dBc/Hz, both of which are much better than the previously-reported best phase noise of -60 dBc/Hz at an offset of 1 kHz from a 54 MHz carrier in an SiO₂ OMO. [7]

As we continued to increase the input power, we began to see higher order harmonics

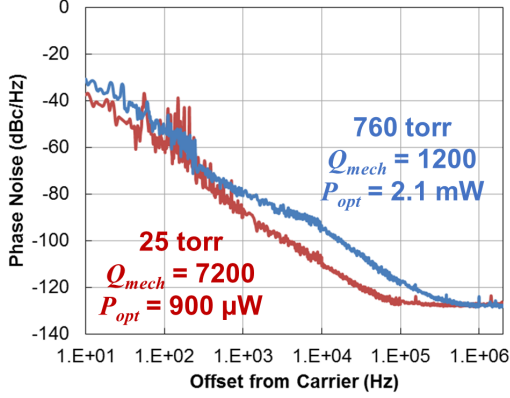


Figure 6.17: Phase noise measurements in air and vacuum of a four-spoke PSG ring with $r_o = 52.5 \mu\text{m}$. The mechanical mode that self-excited in these device was the fundamental radially-symmetric mode, which had $\Omega_m/2\pi = 18.6 \text{ MHz}$. After reducing air damping, Q_{mech} increased from 1200 to 7200 and phase noise improved by 7 dBc/Hz. P_{opt} for these measurements was chosen to optimize the phase noise.

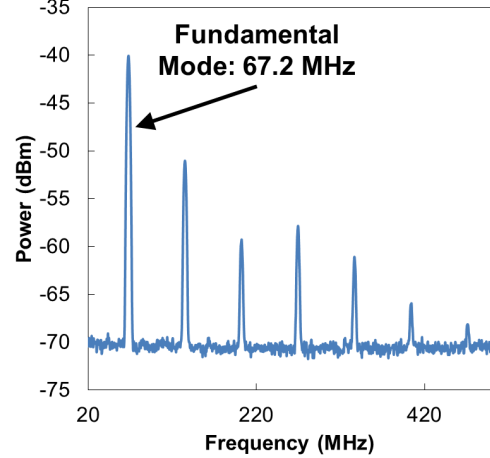


Figure 6.18: Measured higher-order harmonics of the 67.2 MHz fundamental frequency in a two-spoke PSG device with $r_o = 15 \mu\text{m}$. This device was measured in air with an integrated waveguide and vertical grating couplers. To excite harmonics out to 500 MHz, the power at the device was approx. 30 mW.

in the signal from the photodetector. (These are explained in Section 3.2.) An example of these with harmonics out to about 500 MHz is shown in Figure 6.18.

6.4.2 Silicon Optomechanical Resonator Measurements

Stand-alone, single-crystal silicon optomechanical oscillators were characterized in both air and vacuum using tapered-fiber coupling. A wide range of resonator sizes and thicknesses were fabricated, including two- and four-spoke resonators with radii from $5 \mu\text{m}$ to $25 \mu\text{m}$. Device thickness varied from 220 nm to $2.5 \mu\text{m}$. The 220 nm devices were anchored with SiO_2 following a timed release in HF, while the thick resonators were anchored with poly-Si, as shown in Figure 6.10.

The Q_{opt} of the Si devices varied significantly, depending on the etch conditions and additional sidewall treatment. We did not attempt to maximize the Q_{opt} of the Si devices since we were aiming for the best phase noise performance. As a result, the Q_{opt} merely had to be high enough to enable self-oscillation at reasonable powers (usually, $Q_{opt} \approx 1 \times 10^5$ was enough); higher Q_{opt} was found to degrade the phase noise performance, as described in Chapter 3.

For 220 nm-thick devices reactive-ion etched in HBr and Cl_2 transformer-coupled plasma, the best measured Q_{opt} was 2.1×10^5 . This etch was also used for devices approximately $1 \mu\text{m}$ thick, but without further treatment, the best measured Q_{opt} was only 7.9×10^4 . The reason for this degraded Q_{opt} compared to the thinner devices was the fact that the effects of micromasking from mask redeposition during the etch become more significant for longer

Table 6.3: Summary of best results for Si devices

r_o (μm)	15	17.5	20	25
r_i (μm)	10.75	13	15.5	17
Thickness (μm)	0.22	0.22	0.22	~ 1
Q_{opt}	9.4×10^4	1.1×10^5	2.1×10^5	2.4×10^5
$\Omega_m/2\pi$ (MHz)	104	87	77.3	62
Q_{mech} in air				1940
in vac	14500	17000	13600	10400
Phase Noise @ 1kHz offset (dBc/Hz)	-93	-79	-97	N/A

etches. To reduce the sidewall roughness, we used a cycled wet chemical smoothing process in which the Si was repeatedly oxidized, then the thin oxide layer was removed. Specifically, we used three RCA cleaning cycles to smooth the silicon, similar to the process demonstrated in [98]. Following this smoothing process, the best measured Q_{opt} was 2.4×10^5 .

With the low Q_{opt} of these devices, the P_{th} was expected to be relatively high. For example, the theoretical minimum P_{th} for the $r_o = 17.5 \mu\text{m}$ device shown in Table 6.3, based on Eq. 3.10, is about 1 mW (see Figure 6.19). However, we observe regenerative optomechanical oscillations at input powers as low as 75 μW , less than one tenth of the predicted value. This implies that some additional effects are contributing to the coupling between the optical and mechanical modes. Based on the discussion in Section 3.3.3, a likely cause is the photoelastic effect, in which strain in a material changes the refractive index. In silicon waveguides, the magnitude of this effect has been shown to be on the order of that of radiation pressure. [52]

A summary of the best measured OMO characteristics with respect to device geometry is shown in Table 6.3. Generally, Si had much higher Q_{mech} and better phase noise performance than PSG, with the best device's phase noise spectra measured in vacuum at two different optical resonances shown in Figure 6.20. The best phase noise was found from optimizing input power, detuning, and coupling. In addition, the Si devices achieved higher Ω_m compared to PSG, since we were able to make smaller devices without overly degrading Q_{opt} .

6.4.3 Si₃N₄ Optomechanical Resonator Measurements

In stoichiometric Si₃N₄, we made resonators with radii ranging from 5 μm to 25 μm . Device thickness was about 400 nm. We also varied the number of spokes from one to four.

We did not attempt to maximize the Q_{opt} of the Si₃N₄ devices since we were aiming for the best phase noise performance. As a result, the Q_{opt} merely had to be high enough to enable self-oscillation at reasonable powers (generally, $Q_{opt} \approx 1 \times 10^5$ was sufficient); higher Q_{opt} was found to degrade the phase noise performance, as described in Chapter 3. The

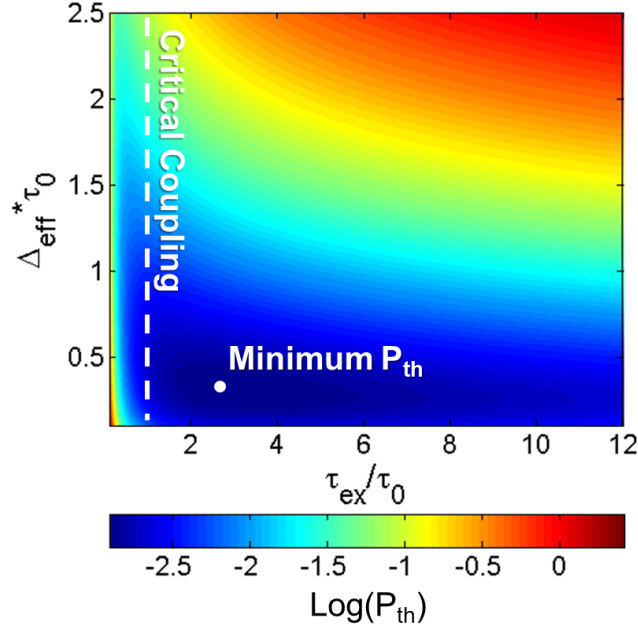


Figure 6.19: Theoretical calculation of P_{th} with respect to photon lifetime due to coupling to the waveguide τ_{ex} and effective detuning from the optical resonance. This calculation is for a 220 nm thick silicon optomechanical resonator with $r_o = 17.5 \mu\text{m}$, $r_i = 13 \mu\text{m}$, $Q_{opt} = 1.1 \times 10^5$, $\Omega_m/2\pi = 87 \text{ MHz}$, and $Q_{mech} = 1.7 \times 10^4$.

typical Q_{opt} of the Si_3N_4 resonators was around 1×10^5 , with little variation with respect to outer radius r_o for radii greater than $7.5 \mu\text{m}$. This indicates that sidewall roughness was not the dominant loss mechanism for our Si_3N_4 resonators. If sidewall roughness were the dominant loss mechanism, we would see a dramatic decrease in Q_{opt} as r_o decreased, since a greater proportion of the optical mode would overlap with the rough sidewall. Based on other demonstrations of Si_3N_4 optical resonators with $Q_{opt} > 1$ million, [5, 56] the dominant loss mechanism is likely hydrogen on the surface, which can be reduced by long anneals at temperatures above 1200°C , [99] which we did not include in our fabrication process.

In Si_3N_4 , we made spoke-supported rings with one, two, and four spokes to see how the perturbation from the spokes contributes to mechanical loss. As shown in Figure 6.3, adding spokes to a ring perturbs the mode shape such that it is no longer perfectly radially symmetric. From FEM simulation, we can see that fewer spokes results in a visibly less-perturbed mode (see Figure 6.5). On the other hand, as discussed in Section 6.2.1, FEM simulation suggests that four spokes cancel out forces at the center anchor better than two spokes. To determine whether mode perturbation or force at the center anchor is a larger loss mechanism, we measured the Q_{mech} of identically-sized Si_3N_4 devices on the same die having various spoke numbers. We found, as shown in Figure 6.21, that two-spoke devices consistently had lower Q_{mech} than four-spoke devices. The one-spoke devices had very low yield, as they tended to easily tilt and stick to the substrate, but the single device that we were able to measure had $r_o = 15 \mu\text{m}$ and a Q_{mech} that was 7% less than the corresponding four-spoke Q_{mech} . These comparisons imply that force cancellation at the center anchor

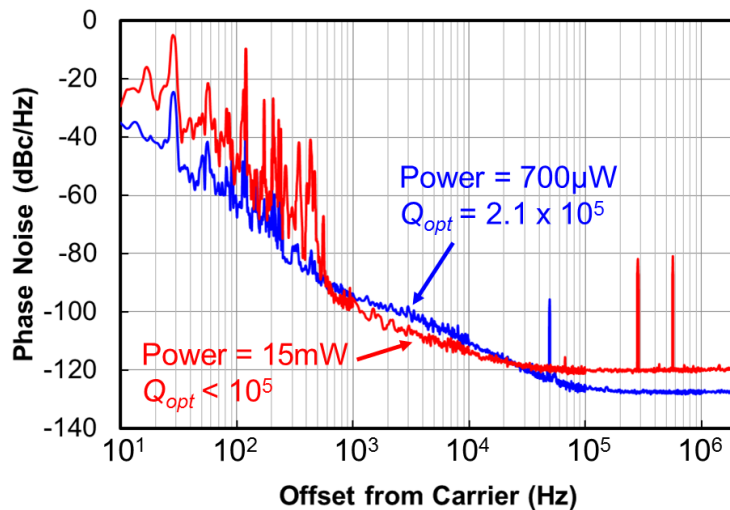


Figure 6.20: Phase noise measurements in vacuum of a four-spoke Si ring with $r_o = 20 \mu\text{m}$ pumped at two different optical resonances. One resonance had $Q_{opt} = 2.1 \times 10^5$ and the other had a $Q_{opt} < 10^5$. The mechanical mode was the fundamental radially-symmetric mode, $\Omega_m/2\pi = 77.3 \text{ MHz}$. The intrinsic Q_{mech} was 1.36×10^4 . The measurement at lower Q_{opt} has more close-to-carrier “technical” noise, but for medium offsets, the phase noise is improved (-97 dBc/Hz) with respect to the higher- Q_{opt} measurement (-94 dBc/Hz), as expected. P_{opt} for this measurement was chosen to optimize the phase noise. Clearly, Q_{opt} also greatly affects the amount of power needed for regenerative oscillations, since the lower- Q_{opt} measurement required 15 mW of optical power, whereas the higher- Q_{opt} measurement required only $700 \mu\text{W}$.

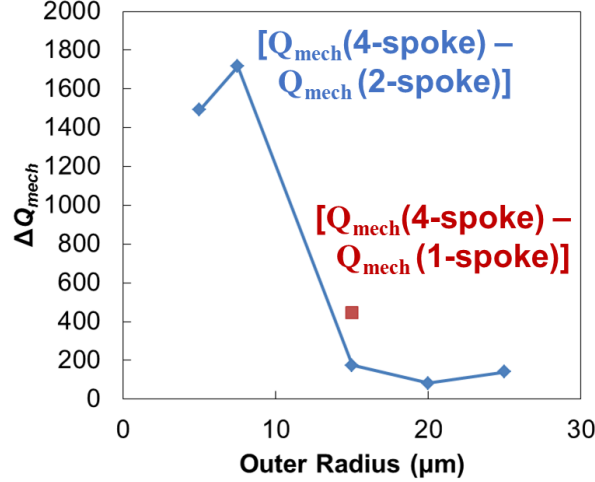


Figure 6.21: A comparison of Q_{mech} in one- and two-spoke Si_3N_4 resonators to that of four-spoke resonators. Graphed here is the difference between the four-spoke Q_{mech} and the two-spoke Q_{mech} with respect to device outer radius. Only one single-spoke resonator survived the fabrication process without sticking to the substrate, and that single point is also graphed. Data indicates that four-spoke resonators have consistently higher Q_{mech} than two-spoke resonators, and the single-spoke resonators also supports the trend that fewer spokes degrades Q_{mech} . In addition, the difference in Q_{mech} between four- and two-spoke resonators decreases as device radius increases.

has more of an effect on the Q_{mech} of the device than does the shape of the mechanical resonance. The trend in Figure 6.21 also implies that as the device radius increases, the effect of imbalanced spokes decreases.

With the lower Q_{opt} of the Si_3N_4 devices, the P_{th} was expected to be relatively high. For example, the theoretical minimum P_{th} in air for the $r_o = 25 \mu\text{m}$ device shown in Table 6.4, based on Eq. 3.10, is about 53 mW. However, we begin to see regenerative optomechanical oscillations at input powers lower than 15 mW, less than one third of the predicted value. This implies that some additional effects are contributing to the coupling between the optical and mechanical modes. Based on the discussion in Section 3.3.3, a potential contributor is the photoelastic effect, in which strain in a material changes its refractive index. However, to our knowledge, photoelastic effects have not yet been quantified in Si_3N_4 , so it is unclear whether they would be large enough to significantly contribute to the optomechanical coupling in these devices.

The best measured performance metrics of the Si_3N_4 devices are shown in Table 6.4. The best OMO we measured had a Q_{mech} in vacuum of about 10^4 at a Ω_m of 74 MHz $\times 2\pi$, [82] and its phase noise spectrum and a Lorentzian fit of the high- Q_{mech} Brownian motion is shown in Figure 6.22. The mechanical mode that self-excited in these device was the fundamental radially-symmetric mode. After reducing air damping, Q_{mech} increased from 1800 to 10400 and phase noise improved by about 7 dBc/Hz, to -102 dBc/Hz. P_{opt} for these measurements was chosen to optimize the phase noise. We further investigated the optical harmonics generated with increased input power, and an example of these with

Table 6.4: Summary of best results for Si₃N₄ devices

r_o (μm)	5	7.5	15	20	25
r_i (μm)	3	4.2	11	15	17
No. of Spokes	4	4	4	4	4
Q_{opt}	1.4×10^4	1.3×10^5			1.5×10^5
$\Omega_m/2\pi$ (MHz)	429	279	118	94	74
Q_{mech} in air					1800
in vac	3270	2490	7300	5800	10400

harmonics out to 2 GHz is shown in Figure 6.23. For this device, an optical power at the device of approximately 5.5 mW generated visible harmonics out to 1 GHz. Even more harmonics became visible with higher input power; for a power at the device of 32 mW, harmonics out to about 3 GHz are visible.

6.5 Device Performance Comparison

The phase noise of the best PSG, Si, Si₃N₄ OMOs is graphed in Figure 6.24, with the raw data shown in Figure 6.24a. To fairly compare the devices, phase noise was scaled to a frequency of 10 MHz. This scaling assumes the phase noise is dependent on frequency $f = \Omega_m/2\pi$ as described by Leeson's equation [82]:

$$\mathfrak{L}(f, f_{oc}) \approx 10 \log \left(C_1 \left(1 + C_2 \frac{f^2}{(f_{oc})^2} \right) \right) \quad (6.3a)$$

$$\mathfrak{L}(f_{norm}, f_{oc}) - \mathfrak{L}(f_{raw}, f_{oc}) \approx 20 \log(f_{norm}/f_{raw}) \quad (6.3b)$$

where C_1 and C_2 are constants defined in Chapter 3, f_{oc} is the offset from the carrier frequency, f_{norm} is the frequency to which the phase noise is being scaled, and f_{raw} is the original carrier frequency.

The data scaled to 10 MHz is shown in Figure 6.24b. Included in the graph is the previously-reported OMO phase noise from the literature. Based on this plot, it is clear that the PSG device has the worst performance of our devices, the Si device is much better, and the Si₃N₄ device is even better than the Si device. In addition, comparing to the previous work, the PSG ring phase noise is comparable to the SiO₂ microtoroid and slightly higher than the the Si₃N₄ ring from [8].

This, where the Si₃N₄ device has better phase noise than both silicon and PSG, does not intuitively match the phase noise theory we presented in Section 3.4. Based on Leeson's equation, Q_{mech} is the important parameter for improving phase noise. It has also been predicted that higher Q_{opt} degrades phase noise. [54] However, it is the *silicon* device of this group that has the highest $Q_{mech} = 13600$ and the lowest $Q_{opt} < 10^5$ (for this particular

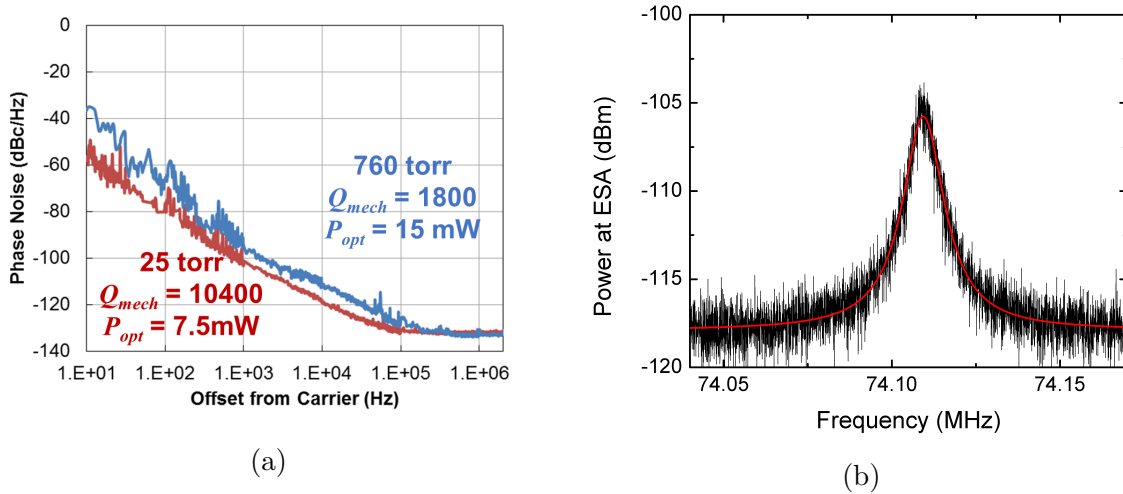


Figure 6.22: Phase noise and Q_{mech} measurements of the best measured Si_3N_4 optomechanical oscillator. This device had $r_o = 25 \mu\text{m}$ and $\Omega_m/2\pi = 74 \text{ MHz}$ for the fundamental radially-symmetric mode. (a) Phase noise measurements in air and vacuum of a four-spoke Si_3N_4 ring resonator. The mechanical mode that self-excited in these device was the fundamental radially-symmetric mode. After reducing air damping, Q_{mech} increased from 1800 to 10400 and phase noise improved by about 7 dBc/Hz. P_{opt} for these measurements was chosen to optimize the phase noise. (b) Brownian motion measurement in vacuum of the Si_3N_4 ring. A Lorentzian fit of the data indicates the intrinsic $Q_{mech} = 10400 \text{ MHz}$.

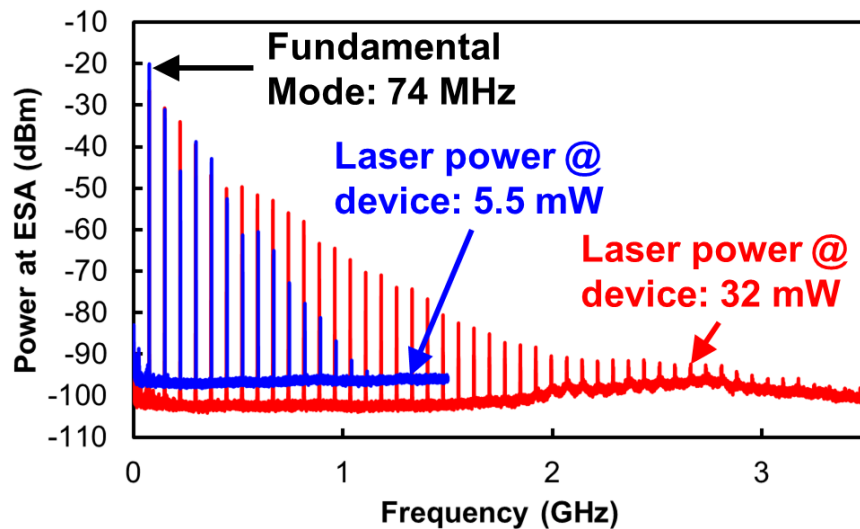
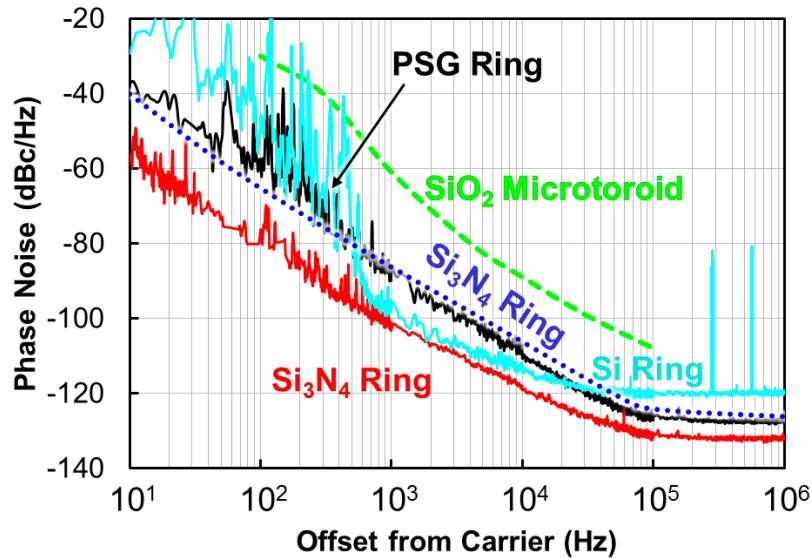
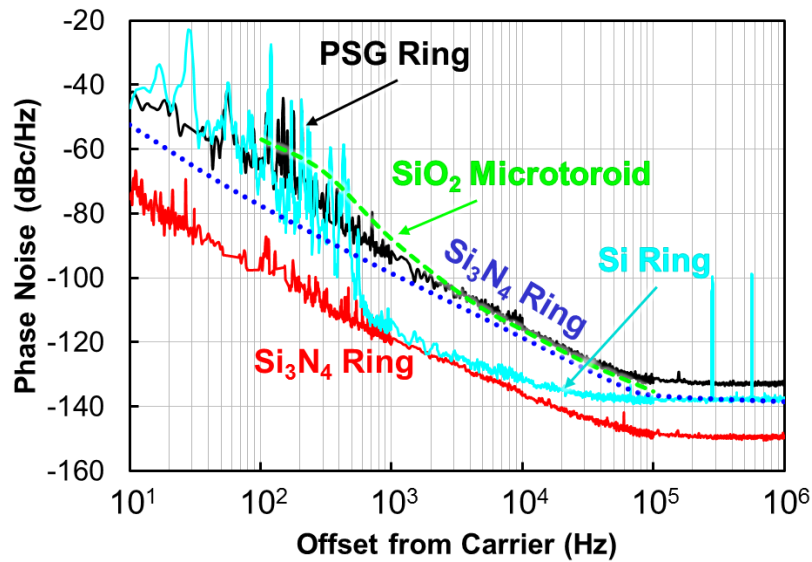


Figure 6.23: Measured optomechanical frequency comb of the 74 MHz fundamental frequency in a four-spoke Si_3N_4 device with $r_o = 25 \mu\text{m}$, measured in vacuum. The interval between each “comb” is 74 MHz. To excite harmonics out to 1 GHz, the power at the device was approximately 5.5 mW. Even more harmonics become visible with higher input power; for a power at the device of 32 mW, harmonics out to about 3 GHz are visible above the noise.



(a)



(b)

Figure 6.24: A comparison of the phase noise of the best single-material devices presented in this chapter and the phase noise of previously-reported optomechanical oscillators. The phase noise in dashed lines is the approximate spectrum of the two reported OMOs in the literature. The SiO_2 microtoroid (green dashed line) was measured in air and had $Q_{mech} = 2000$, $\Omega_m = 217 \text{ MHz} \times 2\pi$. [7] The previously-reported Si_3N_4 ring OMO (blue dotted line) was measured in air at a laser power of 32 mW and had $Q_{mech} = 2000$ and $\Omega_m = 42 \text{ MHz} \times 2\pi$. [8] The performance metrics of the other resonators are listed in Figures 6.17, 6.20, and 6.22. (a) Raw phase noise data for these devices. (b) Phase noise of all devices scaled to 10 MHz.

measurement), yet it has worse phase noise than the Si_3N_4 device. This is due to the smaller carrier signal in the silicon device; the phase noise spectrum is the noise-to-signal ratio, so a smaller carrier signal results in larger phase noise. The carrier signal in silicon is disproportionately small because the threshold power is disproportionately low, as described in Section 6.4.2. Thus, for input powers above the very low threshold, much of the excess power is lost to nonlinear processes, such as scattering into the higher-order optomechanical frequency comb modes, and the carrier signal power remains small.

The Si_3N_4 device also has better performance than the previously-demonstrated nitride OMO. This can be attributed to its much higher Q_{mech} . This high Q_{mech} was achieved through device design and vacuum measurement, and the resultant phase noise is the best to date reported in a single-material cavity optomechanical oscillator. Based on Leeson's equations, as discussed in Chapter 3, the phase noise should approximately depend on the Q_{mech} as follows:

$$\mathfrak{L}(f_{oc}, Q_{mech}) \approx 10 \log \left(C_1 \left(1 + \frac{1}{(Q_{mech})^2} \frac{f^2}{(2f_{oc})^2} \right) \right) \quad (6.4a)$$

$$\mathfrak{L}(f_{oc}, Q_{mech1}) - \mathfrak{L}(f_{oc}, Q_{mech2}) \approx 20 \log(Q_{mech2}/Q_{mech1}) \quad (6.4b)$$

For example, we compare [8] to the Si_3N_4 device measured in vacuum. Based on Eq. 6.4b, all else being equal, the higher- Q_{mech} (10400) device should have phase noise about 14 dBc/Hz lower than the lower- Q_{mech} device (2000). The measured difference between the two is about 20 dBc/Hz, so simply measuring at low ambient pressure does not fully explain the superior performance of our device. Other likely contributors to this difference include device design and Q_{opt} . It should also be noted that our Si_3N_4 device required 7.5 mW, much less than the 32 mW used in [8].

These investigations indicate that, while designing devices for high Q_{mech} is very important for improving phase noise, material choice is perhaps just as important. The comparatively poor performance of our PSG devices makes sense due to its low Q_{mech} , but the clear superiority of the Si_3N_4 OMO to silicon is unexpected if we only consider the mechanical quality factors. The intrinsic optical nonlinearities of the device material here are also important to take into account. We showed that both Si_3N_4 and Si OMOs have empirically stronger coupling between the optical and mechanical modes than is predicted by theory, indicating that other material properties may contribute to optomechanical oscillation. Silicon showed the most deviation from radiation-pressure-driven cavity optomechanical theory, which drove the power in the carrier signal down. This makes Si_3N_4 the best choice of these three materials for a low phase noise optomechanical oscillator.

6.6 Outlook

Optomechanical oscillators with good phase noise performance have the potential to act as reference oscillators in all-optical devices. However, additional functionality, such as electrostatic frequency tuning [100] and electrical read-out, could be added if electrodes were included. Also, the best Q_{mech} demonstrated here is still much lower than has been demon-

strated in polysilicon electrostatic spoke-supported ring resonators (6.8×10^4 at 24 MHz), [90] so there may be room for improvement in Q_{mech} .

Although a silicon OMO seems to be the logical choice for gaining electrical functionality and higher Q_{mech} , our investigations above show that simply using silicon as the OMO material results in low carrier power. One alternative way to simultaneously add electrical functionality and increase Q_{mech} would be to mechanically couple an optomechanical resonator to a high- Q_{mech} electrostatic resonator. In this way, electrical input/output could be accessed through the electrostatic resonator. Additionally, the mechanical energy in the system would be shared between the lower- Q_{mech} optomechanical resonator and the high- Q_{mech} resonator, thereby “boosting” the effective Q_{mech} of the system above that of the optomechanical resonator alone. [101] This possible avenue of improvement is currently being investigated.

Chapter 7

Conclusion

Optical dielectric microdisk and ring resonators are circular structures that store light only at specific wavelengths in whispering-gallery modes that circulate around the outer edge of the device. The modes of these resonators can be accessed by bringing a waveguide into close proximity with the outer edge of the disk, such that some of the evanescent fields of the waveguide and disk overlap, and light transfers between them. The characteristic parameters of these devices are the quality factor, the resonance wavelengths, and the spacing between resonances (free spectral range). The quality factor indicates the lossiness of the resonator, with a high quality factor resulting in narrow resonance linewidth. A device with a very low quality factor is essentially not wavelength-selective, and merely acts as a scattering site to any waveguide coupling to it. The absolute resonance wavelengths are dependent on the optical path length around the resonator, making these very sensitive to size changes and variations in the refractive index. Coupling to a waveguide is another mechanism that affects the system characteristics. As an additional avenue through which light escapes from the resonator, it changes the effective quality factor, and thus the optical resonance linewidth. The magnitude of this effect depends on the optical and geometrical characteristics of the waveguide as well as its distance from the resonator. Taking advantage of these characteristics has resulted in many interesting applications, including various sensors, dynamically-tunable optical filters, lasers, and optical delay lines.

Additional phenomena become apparent in high optical quality factor resonators that are free to vibrate. Because of the resonator's sensitivity to optical path length changes, a mechanical resonance strongly interacts with the optical resonances. The study of optomechanical coupling in on-chip cavities has resulted in some new sensors, optical mixers, and tools for studying quantum squeezed states.

In this work, we investigated a variety of on-chip microdisk and microring resonators with high optical and mechanical quality factors. The focus was specifically on applications in optical communication and all-optical frequency references.

A new method was demonstrated for wafer-scale fabrication of high optical quality factor silica resonators. By heating phosphosilicate glass enough for it to flow, we smoothed the resonator surfaces, significantly reducing optical loss. This process yielded a maximum optical quality factor of about 15 million. Unlike previous methods for achieving ultra-high optical quality factor, our phosphosilicate glass devices can easily be integrated with on-chip waveguides, as reflowing does not significantly change device dimensions.

A platform for integrating low-loss silica optical components with MEMS actuators was developed. This technique implemented silicon MEMS actuators in silicon and connected them to reflowed phosphosilicate glass waveguides that were free to move. With these actuators, we were able to tune the coupling between a waveguide and resonator from the overcoupled to the undercoupled regimes. This device can act as a tunable-bandwidth notch filter with a tuning range from 0.8 to 8.5 GHz. Because of the low-loss nature of silica, the minimum bandwidth we demonstrated is the lowest among on-chip tunable filters. This fabrication process provides a platform for the creation of other MEMS-tuned, low-loss optical devices.

Finally, we presented a study of optomechanical oscillator performance in three different materials, phosphosilicate glass, silicon, and stoichiometric silicon nitride. We used similar, spoke-supported ring geometries in all devices, and we focused on their phase noise performance, which is a key metric for a reference oscillator. We found that, similar to electrical oscillators, a high mechanical quality factor was important for achieving low phase noise, but other factors were also important. A high optical quality factor determined how much input power was required to reach the regenerative oscillation regime, but if it was too high, it degraded the phase noise performance. We also discovered that material choice affected the phase noise; although the silicon optomechanical oscillators had the best mechanical quality factors, the phase noise-to-signal ratio was not the best, since the carrier power was low. This was likely due to nonlinear optical effects in silicon, such as the photoelastic effect. The best device we measured was a silicon nitride optomechanical oscillator, which had a mechanical quality factor of about 10^4 and the best phase noise, to our knowledge, in a single-material optomechanical oscillator.

Bibliography

- [1] H. Miao, K. Srinivasan, and V. Aksyuk, “Integrated MEMS tunable high quality factor optical cavity for optomechanical transduction,” in *Lasers and Electro-Optics (CLEO) and Quantum Electronics and Laser Science Conference (QELS), 2010 Conference on*, pp. 1–2, IEEE, 2010.
- [2] M. Borselli, T. Johnson, and O. Painter, “Beyond the Rayleigh scattering limit in high-Q silicon microdisks: theory and experiment,” *Opt. Express*, vol. 13, pp. 1515–1530, Mar 2005.
- [3] D. Armani, T. Kippenberg, S. Spillane, and K. Vahala, “Ultra-high-Q toroid microcavity on a chip,” *Nature*, vol. 421, no. 6926, pp. 925–928, 2003.
- [4] H. Lee, T. Chen, J. Li, K. Y. Yang, S. Jeon, O. Painter, and K. J. Vahala, “Chemically etched ultrahigh- q wedge-resonator on a silicon chip,” *Nature Photonics*, vol. 6, no. 6, pp. 369–373, 2012.
- [5] K. Luke, A. Dutt, C. B. Poitras, and M. Lipson, “Overcoming Si_3N_4 film stress limitations for high quality factor ring resonators,” *arXiv preprint arXiv:1306.2994*, 2013.
- [6] M.-C. Tien, J. F. Bauters, M. J. R. Heck, D. T. Spencer, D. J. Blumenthal, and J. E. Bowers, “Ultra-high quality factor planar Si_3N_4 ring resonators on si substrates,” *Opt. Express*, vol. 19, pp. 13551–13556, Jul 2011.
- [7] M. Hossein-Zadeh, H. Rokhsari, A. Hajimiri, and K. J. Vahala, “Characterization of a radiation-pressure-driven micromechanical oscillator,” *Physical Review A*, vol. 74, no. 2, p. 023813, 2006.
- [8] S. Tallur, S. Sridaran, and S. A. Bhave, “A monolithic radiation-pressure driven, low phase noise silicon nitride opto-mechanical oscillator,” *Optics Express*, vol. 19, no. 24, pp. 24522–24529, 2011.
- [9] “Introduction to LIGO & gravitational waves.” <http://www.ligo.org/science/GW-Enhance.php>. Accessed: 2013-12-04.
- [10] A. M. Lakhani, K. Yu, and M. C. Wu, “Lasing in subwavelength semiconductor nanopatches,” *Semiconductor Science and Technology*, vol. 26, no. 1, p. 014013, 2011.

- [11] K. Srinivasan, H. Miao, M. T. Rakher, M. Davanco, and V. Aksyuk, “Optomechanical transduction of an integrated silicon cantilever probe using a microdisk resonator,” *Nano letters*, vol. 11, no. 2, pp. 791–797, 2011.
- [12] M. Sumetsky, R. Windeler, Y. Dulashko, and X. Fan, “Optical liquid ring resonator sensor,” *Optics Express*, vol. 15, no. 22, pp. 14376–14381, 2007.
- [13] C. J. Chang-Hasnain, “Tunable vcsel,” *Selected Topics in Quantum Electronics, IEEE Journal of*, vol. 6, no. 6, pp. 978–987, 2000.
- [14] M.-C. Tien, A. T. Ohta, K. Yu, S. L. Neale, and M. C. Wu, “Heterogeneous integration of InGaAsP microdisk laser on a silicon platform using optofluidic assembly,” *Applied Physics A*, vol. 95, no. 4, pp. 967–972, 2009.
- [15] K. Jinguji, “Synthesis of coherent two-port optical delay-line circuit with ring waveguides,” *Lightwave Technology, Journal of*, vol. 14, no. 8, pp. 1882–1898, 1996.
- [16] J. Yao and M. C. Wu, “Bandwidth-tunable add-drop filters based on micro-electro-mechanical-system actuated silicon microtoroidal resonators,” *Optics letters*, vol. 34, no. 17, pp. 2557–2559, 2009.
- [17] P. Orlandi, C. Ferrari, M. John Strain, A. Canciamilla, F. Morichetti, M. Sorel, P. Bassi, and A. Melloni, “Reconfigurable silicon filter with continuous bandwidth tunability,” *Optics Letters*, vol. 37, no. 17, pp. 3669–3671, 2012.
- [18] Y. Ding, M. Pu, L. Liu, J. Xu, C. Peucheret, X. Zhang, D. Huang, and H. Ou, “Bandwidth and wavelength-tunable optical bandpass filter based on silicon microring-mzi structure,” *Optics Express*, vol. 19, no. 7, pp. 6462–6470, 2011.
- [19] K. E. Grutter, A. Yeh, A. Grine, and M. C. Wu, “An integrated, silica-based, MEMS-actuated, tunable-bandwidth optical filter with low minimum bandwidth,” in *CLEO: Science and Innovations*, Optical Society of America, 2013.
- [20] E. L. Wooten, R. L. Stone, E. W. Miles, and E. M. Bradley, “Rapidly tunable narrowband wavelength filter using LiNbO₃ unbalanced Mach-Zehnder interferometers,” *Lightwave Technology, Journal of*, vol. 14, no. 11, pp. 2530–2536, 1996.
- [21] R. Stanley, R. Houdré, U. Oesterle, M. Gailhanou, and M. Ilegems, “Ultrahigh finesse microcavity with distributed bragg reflectors,” *Applied Physics Letters*, vol. 65, no. 15, pp. 1883–1885, 1994.
- [22] M. Y. Liu and S. Y. Chou, “High-modulation-depth and short-cavity-length silicon fabry-perot modulator with two grating bragg reflectors,” *Applied Physics Letters*, vol. 68, no. 2, pp. 170–172, 1996.
- [23] J. W. Strutt, *The Theory of Sound*, vol. II. MacMillan and Co., Ltd., 1896.
- [24] S. McCall, A. Levi, R. Slusher, S. Pearton, and R. Logan, “Whispering-gallery mode microdisk lasers,” *Applied physics letters*, vol. 60, p. 289, 1992.

- [25] G. Anetsberger, R. Rivière, A. Schliesser, O. Arcizet, and T. J. Kippenberg, “Ultralow-dissipation optomechanical resonators on a chip,” *Nature Photonics*, vol. 2, no. 10, pp. 627–633, 2008.
- [26] R. P. Wang and M.-M. Dumitrescu, “Theory of optical modes in semiconductor microdisk lasers,” *Journal of applied physics*, vol. 81, no. 8, pp. 3391–3397, 1997.
- [27] J. A. Stratton, *Electro-Magnetic Theory*. McGraw-Hill, 1941.
- [28] A. Andronico, X. Caillet, I. Favero, S. Ducci, V. Berger, and G. Leo, “Semiconductor microcavities for enhanced nonlinear optics interactions,” *Journal of the European Optical Society-Rapid publications*, vol. 3, 2008.
- [29] T. Harayama, P. Davis, and K. S. Ikeda, “Nonlinear whispering gallery modes,” *Physical review letters*, vol. 82, no. 19, p. 3803, 1999.
- [30] K. Okamoto, *Fundamentals of Optical Waveguides*. Academic Press, 2 ed., 2005.
- [31] M.-C. Lee, *Tunable Optical Microresonators Using Micro-electro-mechanical-system (MEMS) Technology*. PhD thesis, University of California, Los Angeles, 2005.
- [32] D. Rowland and J. Love, “Evanescent wave coupling of whispering gallery modes of a dielectric cylinder,” in *Optoelectronics, IEE Proceedings J*, vol. 140, pp. 177–188, IET, 1993.
- [33] A. W. Snyder and J. D. Love, *Optical Waveguide Theory*. Chapman and Hall, 1983.
- [34] H. A. Haus, *Waves and Fields in Optoelectronics*. Prentice Hall, Inc., 1984.
- [35] E. Marcatili, “Dielectric Rectangular Waveguide and Directional Coupler for Integrated Optics,” *The Bell System Technical Journal*, vol. 48, no. 7, pp. 2071–2102, 1969.
- [36] B. E. Little, S. T. Chu, H. A. Haus, J. Foresi, and J.-P. Laine, “Microring resonator channel dropping filters,” *Lightwave Technology, Journal of*, vol. 15, no. 6, pp. 998–1005, 1997.
- [37] H. Haus, W. Huang, S. Kawakami, and N. Whitaker, “Coupled-mode theory of optical waveguides,” *Lightwave Technology, Journal of*, vol. 5, no. 1, pp. 16–23, 1987.
- [38] L. Chen, N. Sherwood-Droz, and M. Lipson, “Compact bandwidth-tunable microring resonators,” *Optics Letters*, vol. 32, no. 22, pp. 3361–3363, 2007.
- [39] G. Anetsberger, O. Arcizet, Q. P. Unterreithmeier, R. Rivière, A. Schliesser, E. M. Weig, J. P. Kotthaus, and T. J. Kippenberg, “Near-field cavity optomechanics with nanomechanical oscillators,” *Nature Physics*, vol. 5, no. 12, pp. 909–914, 2009.
- [40] D. Van Thourhout and J. Roels, “Optomechanical device actuation through the optical gradient force,” *Nature Photonics*, vol. 4, no. 4, pp. 211–217, 2010.

- [41] T. Carmon, H. Rokhsari, L. Yang, T. J. Kippenberg, and K. J. Vahala, “Temporal behavior of radiation-pressure-induced vibrations of an optical microcavity phonon mode,” *Physical Review Letters*, vol. 94, no. 22, p. 223902, 2005.
- [42] M. Eichenfield, R. Camacho, J. Chan, K. J. Vahala, and O. Painter, “A picogram-and nanometre-scale photonic-crystal optomechanical cavity,” *Nature*, vol. 459, no. 7246, pp. 550–555, 2009.
- [43] A. Schließer, *Cavity Optomechanics and Optical Frequency Comb Generation with Silica Whispering-Gallery-Mode Microresonators*. PhD thesis, Ludwig-Maximilians-Universität München, 2009.
- [44] S. D. Senturia, *Microsystem Design*. Springer Science+Business Media, Inc., 2001.
- [45] T. J. Kippenberg and K. J. Vahala, “Cavity opto-mechanics,” *Optics Express*, vol. 15, no. 25, pp. 17172–17205, 2007.
- [46] K. Ikeda, R. E. Saperstein, N. Alic, and Y. Fainman, “Thermal and kerr nonlinear properties of plasma-deposited silicon nitride/silicon dioxide waveguides,” *Optics Express*, vol. 16, no. 17, pp. 12987–12994, 2008.
- [47] A. D. Bristow, N. Rotenberg, and H. M. van Driel, “Two-photon absorption and Kerr coefficients of silicon for 850–2200 nm,” *Applied Physics Letters*, vol. 90, p. 191104, 2007.
- [48] D. Hohlfeld and H. Zappe, “An all-dielectric tunable optical filter based on the thermo-optic effect,” *Journal of optics A: Pure and applied Optics*, vol. 6, no. 6, p. 504, 2004.
- [49] G. Cocorullo, F. Della Corte, and I. Rendina, “Temperature dependence of the thermo-optic coefficient in crystalline silicon between room temperature and 550 k at the wavelength of 1523 nm,” *Applied Physics Letters*, vol. 74, p. 3338, 1999.
- [50] Q. Lin, O. J. Painter, and G. P. Agrawal, “Nonlinear optical phenomena in silicon waveguides: modeling and applications,” *Optics Express*, vol. 15, no. 25, pp. 16604–16644, 2007.
- [51] T. Carmon, L. Yang, and K. J. Vahala, “Dynamical thermal behavior and thermal self-stability of microcavities,” in *Integrated Photonics Research and Applications*, Optical Society of America, 2005.
- [52] P. T. Rakich, P. Davids, and Z. Wang, “Tailoring optical forces in waveguides through radiation pressure and electrostrictive forces,” *Optics express*, vol. 18, no. 14, pp. 14439–14453, 2010.
- [53] D. B. Leeson, “A simple model of feedback oscillator noise spectrum,” *Proceedings of the IEEE*, vol. 54, no. 2, pp. 329–330, 1966.

- [54] A. Grine, K. E. Grutter, T. Rocheleau, N. Quack, T. Beyazoglu, Z. Zheng, I. Jutla, M. C. Wu, and C. T. Nguyen, “Phase noise spectrum and carrier power modeling of high performance optomechanical oscillators,” in *CLEO: QELS Fundamental Science*, Optical Society of America, 2013.
- [55] J. Steinlechner, C. Kruger, N. Lastzka, S. Steinlechner, A. Khalaidovski, and R. Schnabel, “Optical absorption measurements on crystalline silicon test masses at 1550 nm,” *Classical and Quantum Gravity*, vol. 30, no. 9, p. 095007, 2013.
- [56] A. Gondarenko, J. S. Levy, and M. Lipson, “High confinement micron-scale silicon nitride high Q ring resonator,” *Optics Express*, vol. 17, no. 14, pp. 11366–11370, 2009.
- [57] M. Ohashi, K. Shiraki, and K. Tajima, “Optical loss property of silica-based single-mode fibers,” *Lightwave Technology, Journal of*, vol. 10, no. 5, pp. 539–543, 1992.
- [58] R. Soref and B. Bennett, “Electrooptical effects in silicon,” *Quantum Electronics, IEEE Journal of*, vol. 23, no. 1, pp. 123–129, 1987.
- [59] R. Dekker, N. Usechak, M. Först, and A. Driessen, “Ultrafast nonlinear all-optical processes in silicon-on-insulator waveguides,” *Journal of Physics D: Applied Physics*, vol. 40, no. 14, p. R249, 2007.
- [60] M. Soltani, S. Yegnanarayanan, and A. Adibi, “Ultra-high Q planar silicon microdisk resonators for chip-scale silicon photonics,” *Optics express*, vol. 15, no. 8, pp. 4694–4704, 2007.
- [61] J. F. Bauters, M. J. R. Heck, D. John, D. Dai, M.-C. Tien, J. S. Barton, A. Leinse, R. G. Heideman, D. J. Blumenthal, and J. E. Bowers, “Ultra-low-loss high-aspect-ratio Si_3N_4 waveguides,” *Opt. Express*, vol. 19, pp. 3163–3174, Feb 2011.
- [62] H. Lee, T. Chen, J. Li, K. Y. Yang, O. Painter, and K. J. Vahala, “Ultra-high-Q wedge resonators with precise FSR control,” in *CLEO: Science and Innovations*, Optical Society of America, 2012.
- [63] C. Hammond, “Fusion temperatures of $\text{SiO}_2\text{-P}_2\text{O}_5$ binary glasses,” *Physics and Chemistry of Glasses*, vol. 19, no. 3, pp. 41–42, 1978.
- [64] K. Nassau, R. Levy, and D. Chadwick, “Modified phosphosilicate glasses for VLSI applications,” *Journal of The Electrochemical Society*, vol. 132, no. 2, pp. 409–415, 1985.
- [65] T. Izawa, N. Shibata, and A. Takeda, “Optical attenuation in pure and doped fused silica in the IR wavelength region,” *Applied Physics Letters*, vol. 31, no. 1, pp. 33–35, 1977.
- [66] M. Horiguchi and H. Osanai, “Spectral losses of low-OH-content optical fibres,” *Electronics Letters*, vol. 12, no. 12, pp. 310–312, 1976.

- [67] T. Carmon, L. Yang, and K. J. Vahala, “Dynamical thermal behavior and thermal self-stability of microcavities,” *Optics Express*, vol. 12, p. 4742, 2004.
- [68] S. T. Cheung, B. Guan, S. S. Djordjevic, K. Okamoto, and S. Yoo, “Low-loss and High Contrast Silicon-on-Insulator (SOI) Arrayed Waveguide Grating,” in *CLEO: Science and Innovations*, Optical Society of America, 2012.
- [69] D. Olynick. Personal communication.
- [70] T. Kippenberg, S. Spillane, and K. Vahala, “Modal coupling in traveling-wave resonators,” *Optics letters*, vol. 27, no. 19, pp. 1669–1671, 2002.
- [71] R. Bowling and G. Larrabee, “Deposition and reflow of phosphosilicate glass,” *Journal of The Electrochemical Society*, vol. 132, no. 1, pp. 141–145, 1985.
- [72] Y. Liu, M. Davanço, V. Aksyuk, and K. Srinivasan, “Electromagnetically Induced Transparency and Wideband Wavelength Conversion in Silicon Nitride Microdisk Optomechanical Resonators,” *Physical Review Letters*, vol. 110, no. 22, p. 223603, 2013.
- [73] B. Zhang, D. Leuenberger, M. Ming-Chang Lee, A. E. Willner, and M. C. Wu, “Experimental demonstration of dynamic bandwidth allocation using a mems-actuated bandwidth-tunable microdisk resonator filter,” *Photonics Technology Letters, IEEE*, vol. 19, no. 19, pp. 1508–1510, 2007.
- [74] D. Kilper, R. Bach, D. Blumenthal, D. Einstein, T. Landolsi, L. Ostar, M. Preiss, and A. Willner, “Optical performance monitoring,” *Journal of Lightwave Technology*, vol. 22, no. 1, p. 294, 2004.
- [75] G. K. Fedder, *Simulation of microelectromechanical systems*. PhD thesis, University of California, Berkeley, 1994.
- [76] M. T. A. Saif and N. C. MacDonald, “A millinewton microloading device,” *Sensors and Actuators A: Physical*, vol. 52, no. 1, pp. 65–75, 1996.
- [77] R. Pratt, G. Johnson, R. Howe, and J. Chang, “Micromechanical structures for thin film characterization,” in *Solid-State Sensors and Actuators, 1991. Digest of Technical Papers, TRANSDUCERS’91., 1991 International Conference on*, pp. 205–208, IEEE, 1991.
- [78] K. A. Shaw, Z. L. Zhang, and N. C. MacDonald, “SCREAM I: a single mask, single-crystal silicon, reactive ion etching process for microelectromechanical structures,” *Sensors and Actuators A: Physical*, vol. 40, no. 1, pp. 63–70, 1994.
- [79] K. E. Grutter, A. M. Yeh, S. K. Patra, and M. C. Wu, “A new fabrication technique for integrating silica optical devices and MEMS,” in *Optical MEMS and Nanophotonics (OPT MEMS), 2010 International Conference on*, pp. 33–34, IEEE, 2010.
- [80] J. Chan, T. M. Alegre, A. H. Safavi-Naeini, J. T. Hill, A. Krause, S. Gröblacher, M. Aspelmeyer, and O. Painter, “Laser cooling of a nanomechanical oscillator into its quantum ground state,” *Nature*, vol. 478, no. 7367, pp. 89–92, 2011.

- [81] M. Hossein-Zadeh and K. J. Vahala, “Photonic RF down-converter based on optomechanical oscillation,” *Photonics Technology Letters, IEEE*, vol. 20, no. 4, pp. 234–236, 2008.
- [82] T. O. Rocheleau, A. J. Grine, K. E. Grutter, R. A. Schneider, N. Quack, M. C. Wu, and C. T.-C. Nguyen, “Enhancement of mechanical Q for low phase noise optomechanical oscillators,” in *Micro Electro Mechanical Systems (MEMS), 2013 IEEE 26th International Conference on*, pp. 118–121, IEEE, 2013.
- [83] L. Ding, C. Baker, P. Senellart, A. Lemaitre, S. Ducci, G. Leo, and I. Favero, “High frequency GaAs nano-optomechanical disk resonator,” *Physical review letters*, vol. 105, no. 26, p. 263903, 2010.
- [84] X. Sun, K. Y. Fong, C. Xiong, W. H. Pernice, and H. X. Tang, “GHz optomechanical resonators with high mechanical q factor in air,” *Optics Express*, vol. 19, no. 22, pp. 22316–22321, 2011.
- [85] W. C. Jiang, X. Lu, J. Zhang, and Q. Lin, “A high-frequency silicon optomechanical oscillator with an ultralow threshold,” in *Frontiers in Optics*, Optical Society of America, 2012.
- [86] X. Sun, X. Zhang, and H. X. Tang, “High- q silicon optomechanical microdisk resonators at gigahertz frequencies,” *Applied Physics Letters*, vol. 100, no. 17, pp. 173116–173116, 2012.
- [87] M. Mitchell, A. C. Hryciw, and P. E. Barclay, “Cavity optomechanics in gallium phosphide microdisks,” *arXiv preprint arXiv:1309.6300*, 2013.
- [88] M. Eichenfield, C. P. Michael, R. Perahia, and O. Painter, “Actuation of micro-optomechanical systems via cavity-enhanced optical dipole forces,” *Nature Photonics*, vol. 1, no. 7, pp. 416–422, 2007.
- [89] C. T.-C. Nguyen, *Micromechanical Signal Processors*. PhD thesis, University of California, Berkeley, 1994.
- [90] S.-S. Li, Y.-W. Lin, Y. Xie, Z. Ren, and C.-C. Nguyen, “Micromechanical “hollow-disk” ring resonators,” in *Micro Electro Mechanical Systems, 2004. 17th IEEE International Conference on. (MEMS)*, pp. 821–824, IEEE, 2004.
- [91] C. Stephenson, “Radial vibrations in short, hollow cylinders of barium titanate,” *The Journal of the Acoustical Society of America*, vol. 28, p. 51, 1956.
- [92] S. D. Penn, A. Ageev, D. Busby, G. M. Harry, A. M. Gretarsson, K. Numata, and P. Willems, “Frequency and surface dependence of the mechanical loss in fused silica,” *Physics Letters A*, vol. 352, no. 1, pp. 3–6, 2006.
- [93] K. Y. Yasumura, T. D. Stowe, E. M. Chow, T. Pfafman, T. W. Kenny, B. C. Stipe, and D. Rugar, “Quality factors in micron- and submicron-thick cantilevers,” *Microelectromechanical Systems, Journal of*, vol. 9, no. 1, pp. 117–125, 2000.

- [94] T. V. Roszhart, “The effect of thermoelastic internal friction on the Q of micromachined silicon resonators,” in *Solid-State Sensor and Actuator Workshop, 1990. 4th Technical Digest., IEEE*, pp. 13–16, IEEE, 1990.
- [95] D. Southworth, R. Barton, S. Verbridge, B. Ilic, A. Fefferman, H. Craighead, and J. Parpia, “Stress and silicon nitride: A crack in the universal dissipation of glasses,” *Physical Review Letters*, vol. 102, no. 22, p. 225503, 2009.
- [96] S. Pourkamali and F. Ayazi, “SOI-based HF and VHF single-crystal silicon resonators with sub-100 nanometer vertical capacitive gaps,” in *TRANSDUCERS, Solid-State Sensors, Actuators and Microsystems, 12th International Conference on, 2003*, vol. 1, pp. 837–840, IEEE, 2003.
- [97] S. S. Verbridge, J. M. Parpia, R. B. Reichenbach, L. M. Bellan, and H. Craighead, “High quality factor resonance at room temperature with nanostrings under high tensile stress,” *Journal of Applied Physics*, vol. 99, p. 124304, 2006.
- [98] D. K. Sparacin, S. J. Spector, and L. C. Kimerling, “Silicon waveguide sidewall smoothing by wet chemical oxidation,” *Journal of Lightwave Technology*, vol. 23, no. 8, p. 2455, 2005.
- [99] M. J. Shaw, J. Guo, G. A. Vawter, S. Habermehl, and C. T. Sullivan, “Fabrication techniques for low-loss silicon nitride waveguides,” in *MOEMS-MEMS Micro & Nanofabrication*, pp. 109–118, International Society for Optics and Photonics, 2005.
- [100] C.-C. Nguyen, “Frequency-selective MEMS for miniaturized low-power communication devices,” *Microwave Theory and Techniques, IEEE Transactions on*, vol. 47, no. 8, pp. 1486–1503, 1999.
- [101] Y.-W. Lin, L.-W. Hung, S.-S. Li, Z. Ren, and C.-C. Nguyen, “Quality factor boosting via mechanically-coupled arraying,” in *Solid-State Sensors, Actuators and Microsystems Conference, 2007. TRANSDUCERS 2007. International*, pp. 2453–2456, IEEE, 2007.

Appendix A

Whispering-Gallery Mode Code

This is the MatLab code that was used to calculate n_{eff} and β_{eq} for optical whispering-gallery mode resonators, described in Chapter 2.

A.1 TM Calculation

```
% Main Parameters
cs=2.99792458e8; % m/s – speed of light
mu=4*pi*10.^-7; % H/m – permeability of free space

n_1=1.45; % index of refraction of waveguide and ring/disk
n_0=1; % index of refraction of air
R=50e-6; % m – radius of microdisk
d=1000e-9; % m – thickness of microdisk

tol=2e-4; % TM_mode must be between +/- tol in order to count as
        solution
l_min=253;
l_max=259;
l_step=1;
k_max=ceil(1+(l_max-l_min)./l_step);
lambda_step=0.00001*10^-6; % m – step size in graph

% Calculate the TM Mode function that must = 0

lambda_min=1.2e-6; % m – minimum desired wavelength in range
lambda_max=2.00e-6; % m – maximum desired wavelength in range

i_max=ceil(1+(lambda_max-lambda_min)/lambda_step);

% Loop through desired wavelengths
% 1. calculate neff
```

```

% 2. calculate mode function value, which is a function of neff

lambda=zeros(1,i_max);
n_eff=zeros(1,i_max);
TM_mode=zeros(1,i_max);
nu=zeros(1,i_max);
l=zeros(1,k_max);
lambda_res=zeros(1,k_max);
neff_res=zeros(1,k_max);
b_eq=zeros(1,k_max);
W_eq=zeros(1,k_max);
n_eff_azi=zeros(1,k_max);

msg1=sprintf('l = azimuthal mode number\nLambda_lm = resonant
wavelength (nm)\nbeta = propagation const (um^-1)\nWmode = mode
width (um)\nn_azi = effective azimuthal index\nn_eff = slab
effective index\n');
disp(msg1)
msg2=sprintf('l\tLambda_lm\tbeta\tWmode\tn_azi\tn_eff ');
disp(msg2)

for k=1:k_max
    l(k)=l_min+(k-1)*l_step;

    for i=1:i_max
        lambda(i)=lambda_min+(i-1)*lambda_step;
        nu(i)=cs./(n_1.*lambda(i));
        omega=2*pi*nu(i);

        % solve for n_eff
        kxd2_max=pi./2; \% this ensures that the solution for kx is
            for TM0
        k0=2.*pi./lambda(i);

        kxd2_sol=(fzero(@(kxd2) findkxTM(lambda(i),n_1,n_0,d,kxd2)
            ,[0 kxd2_max])); \% finds the value of kx at neff
        kx_sol=kxd2_sol.*2./d;

        A=sqrt((n_1.^2-1).*k0.^2-kx_sol.^2);
        kz=sqrt(k0.^2+A.^2);
        n_eff(i)=kz./k0;

        % Calculate TM mode value at this wavelength
        Ulm=(2.*pi.*R.*n_eff(i))./lambda(i);
        Qlm=(2.*pi.*R.*n_0)./lambda(i);
    end
end

```

```

    TM_mode(i) = (0.5.*(besselh((l(k)-1),2,Qlm)-besselh((l(k)+1),2,Qlm)))/(Qlm.*besselh(l(k),2,Qlm))-((n_eff(i)).^2).*(0.5.*(besselj((l(k)-1),Ulm)-besselj((l(k)+1),Ulm)))/(Ulm.*besselj(l(k),Ulm)));

end

lambda_r=0.;
index_r=i_max;
% Find lowest-order zero in TM mode, starting from maximum wavelength
for i=1:i_max
    index=i_max-i+1;

    if real(TM_mode(index))>=0
        if real(TM_mode(index))==0
            lambda_r=lambda(index);
            index_r=index;
            break;
        else
            diff1=abs(TM_mode(index));
            diff2=abs(TM_mode(index-1));
            if diff1<=diff2
                lambda_r=lambda(index);
                index_r=index;
                break;
            else
                lambda_r=lambda(index-1);
                index_r=index-1;
                break;
            end
        end
    end

end

end

end

% Find Mode Profile
R_max=R+8e-6;

R_step=5.*1e-9; % m - step size for calculating mode profile

Ulm_res=(2.*pi.*R.*n_eff(index_r))./lambda_r;
Qlm_res=(2.*pi.*R.*n_0)./lambda_r;

```

```

r_val=0:R_step:R_max;

% Find R_rad
R_rad=R.*l(k)./real(Qlm_res);

% Calculate b_eq
if R_rad>R
    integral_top=quadgk((@(r) ModeProfileSqofR_lessthanR(l(k),
        r,R,Ulm_res,Qlm_res)),0,R)+...
        quadgk((@(r) ModeProfileSqofR_greaterthanR(l(k),r,R,
            Ulm_res,Qlm_res)),R,R_rad);
    integral_bottom=quadgk((@(r) ModeProfileSq_lessthanR(l(k),
        r,R,Ulm_res,Qlm_res)),0,R)+...
        quadgk((@(r) ModeProfileSq_greaterthanR(l(k),r,R,
            Ulm_res,Qlm_res)),R,R_rad);
else
    integral_top=quadgk((@(r) ModeProfileSqofR_lessthanR(l(k),
        r,R,Ulm_res,Qlm_res)),0,R_rad);
    integral_bottom=quadgk((@(r) ModeProfileSq_lessthanR(l(k),
        r,R,Ulm_res,Qlm_res)),0,R_rad);
end

b_eq(k)=l(k).*integral_top./integral_bottom;

% Calculate Mode width
W_eq(k)=2.*(R-l(k)./b_eq(k)); % m

% Calculate n_eff_azi = b_eq./k0
k0=2.*pi./lambda_r;
n_eff_azi(k)=b_eq(k)./k0;

msg3=sprintf('%d\t%6.2f\t%6.2f\t%6.3f\t%6.4f\t%6.4f',...
    l(k),lambda_r.*1e9,b_eq(k).*1e-6,W_eq(k).*1e6,n_eff_azi(k)
    ,n_eff(index_r));
disp(msg3)

lambda_res(k)=lambda_r;
neff_res(k)=n_eff(index_r);
end

```

A.2 TE Calculation

```

% Main Parameters
cs=2.99792458e8; % m/s - speed of light
mu=4*pi*10.^-7; % H/m - permeability of free space

```

```

% n_1=3.45; % index of refraction of waveguide and ring/disk
n_1=1.45; % index of refraction of waveguide and ring/disk
n_0=1; % index of refraction of air
R=50e-6; % m - radius of microdisk
d=2000e-9; % m - thickness of microdisk

tol=2e-4; % TM_mode must be between +/- tol in order to count as
    solution
l_min=273;
l_max=279;
l_step=1;
k_max=ceil(1+(l_max-l_min)./l_step);
lambda_step=0.00001*10^-6; % m - step size in graph

graph_all=false; %boolean value indicating whether we want to
    graph results

% Calculate the TE Mode function that must = 0

lambda_min=1.2e-6; % m - minimum desired wavelength in range
lambda_max=2.00e-6; % m - maximum desired wavelength in range

i_max=ceil(1+(lambda_max-lambda_min)/lambda_step);

% Loop through desired wavelengths
% 1. calculate neff
% 2. calculate mode function value, which is a function of neff

lambda=zeros(1,i_max);
n_eff=zeros(1,i_max);
TE_mode=zeros(1,i_max);
nu=zeros(1,i_max);
l=zeros(1,k_max);
lambda_res=zeros(1,k_max);
neff_res=zeros(1,k_max);
b_eq=zeros(1,k_max);
W_eq=zeros(1,k_max);
n_eff_azi=zeros(1,k_max);

msg1=sprintf('l = azimuthal mode number\nLambda_lm = resonant
    wavelength (nm)\nbeta = propagation const (um^-1)\nWmode = mode
    width (um)\nn_azi = effective azimuthal index\nn_eff = slab
    effective index\n');
disp(msg1)

```

```

msg2=sprintf('l\tLambda_lm\tbeta\tWmode\tn_azi\tn_eff ');
disp(msg2)

for k=1:k_max
    %this loop steps through the bessel function subscripts l
    l(k)=l_min+(k-1)*l_step;

    %Build eigenvalue equation at the given lambda_step that we
    will later use to find zero point
    for i=1:i_max
        lambda(i)=lambda_min+(i-1)*lambda_step;
        nu(i)=cs./(n_1.*lambda(i));
        omega=2*pi*nu(i);

        % solve for n_eff
        kxd2_max=pi./2; % this ensures that the solution for kx is
        for TE0
            k0=2.*pi./lambda(i);

            %You must find kx in TE!
            kx_sol=(fzero(@(kz) findkzWGTE(n_1,n_0,k0,d./2,kz),[1e-9
                kxd2_max.*2./d]));
                % finds the value of kz at neff

            A=sqrt((n_1.^2-1).*k0.^2-kx_sol.^2);
            kz=sqrt(k0.^2+A.^2);
            n_eff(i)=kz./k0;

            % Calculate TE mode value at this wavelength
            Ulm=(2.*pi.*R.*n_eff(i))./lambda(i);
            Qlm=(2.*pi.*R.*n_0)./lambda(i);

            TE_mode(i)=(0.5.*(besselh((l(k)-1),2,Qlm)-besselh((l(k)+1)
                ,2,Qlm)))./...
                (Qlm.*besselh(l(k),2,Qlm))-...
                (0.5.*(besselj((l(k)-1),Ulm)-besselj((l(k)+1),Ulm)))
                ./...
                (Ulm.*besselj(l(k),Ulm)));

        end

        lambda_r=0.;
        index_r=i_max;
        % Find lowest-order zero in TE mode, starting from maximum
        wavelength

```

```

for i=1:i_max
    index=i_max-i+1;

    if real(TE_mode(index))>=0
        if real(TE_mode(index))==0
            lambda_r=lambda(index);
            index_r=index;
            break;
        else
            diff1=abs(TE_mode(index));
            diff2=abs(TE_mode(index-1));
            if diff1<=diff2
                lambda_r=lambda(index);
                index_r=index;
                break;
            else
                lambda_r=lambda(index-1);
                index_r=index-1;
                break;
            end
        end
    end

end

end

% Find Normalized Mode Profile of Hz
R_max=R+8e-6;

R_step=5.*1e-9; % m - step size for calculating mode profile

Ulm_res=(2.*pi.*R.*n_eff(index_r))./lambda_r;
Qlm_res=(2.*pi.*R.*n_0)./lambda_r;

r_val=0:R_step:R_max;

% Find R_rad
R_rad=R.*l(k)./real(Qlm_res);

% Calculate b_eq
if R_rad>R
    integral_top=quadgk(@(r) (ModeProfileSqofR_lessthanR(l(k)
        ,r,R,Ulm_res,Qlm_res))./(n_eff(index_r).^2),0,R)+...
        quadgk(@(r) (ModeProfileSqofR_greaterthanR(l(k),r,R,
            Ulm_res,Qlm_res))./(n_0.^2)),R,R_rad);

```

```

    integral_bottom=quadgk(@(r) (ModeProfileSq_lessthanR(l(k)
        ,r,R,Ulm_res,Qlm_res))./(n_eff(index_r)).^2),0,R)+...
        quadgk(@(r) (ModeProfileSq_greaterthanR(l(k),r,R,
            Ulm_res,Qlm_res))./(n_0.^2)),R,R_rad);
else
    integral_top=quadgk(@(r) (ModeProfileSqofR_lessthanR(l(k)
        ,r,R,Ulm_res,Qlm_res)),0,R_rad);
    integral_bottom=quadgk(@(r) ModeProfileSq_lessthanR(l(k),
        r,R,Ulm_res,Qlm_res)),0,R_rad);
end

b_eq(k)=l(k).*integral_top./integral_bottom;

% Calculate Mode width
W_eq(k)=2.*(R-l(k)./b_eq(k)); % m

% Calculate n_eff_azi = b_eq./k0
k0=2.*pi./lambda_r;
n_eff_azi(k)=b_eq(k)./k0;

%Print results in table
msg3=sprintf('%d\t%6.2f\t%6.2f\t%6.3f\t%6.4f\t%6.4f',...
    l(k),lambda_r.*1e9,b_eq(k).*1e-6,W_eq(k).*1e6,n_eff_azi(k)
    ,n_eff(index_r));
disp(msg3)

lambda_res(k)=lambda_r;
neff_res(k)=n_eff(index_r);
end

```

A.3 Referenced Functions

```

function kxzerofnc=findkxTM(lambda,n_1,n_0,d,kxd2)
k0=2.*pi./lambda;
kxzerofnc=real(sqrt((n_1.^2-1).*(k0.*d./2).^2-(kxd2).^2)-(1./(n_1
    .^2)).*(kxd2).*tan(kxd2));

```

```

function kzzerofnc=findkzWGTE(n1,n0,k0,d,kz)
%d is **half** the height of the slab
kzzerofnc=(((k0.^2)./(kz.^2)).*((n1.^2)-(n0.^2)))-1-(tan(kz.*d)
    .^2);

```

```

function Ezfnc=ModeProfileSqofR_lessthanR(l,r_val,R,Ulm,Qlm)

```

```
Ezfnrc=(((besselj(1,Ulm.*r_val./R))./(besselj(1,Ulm))).^2)./r_val;
```

```
function Ezfnrc=ModeProfileSqofR_greaterthanR(1,r_val,R,Ulm,Qlm)
Ezfnrc=(((besselh(1,2,Qlm.*r_val./R))./(besselh(1,2,Qlm))).^2)./
r_val);
```

```
function Ezfnrc=ModeProfileSq_lesssthanR(1,r_val,R,Ulm,Qlm)
Ezfnrc=(((besselj(1,Ulm.*r_val./R))./(besselj(1,Ulm))).^2);
```

```
function Ezfnrc=ModeProfileSq_greaterthanR(1,r_val,R,Ulm,Qlm)
Ezfnrc=(((besselh(1,2,Qlm.*r_val./R))./(besselh(1,2,Qlm))).^2);
```

Appendix B

Fabrication Details

Here we present some of the more important details of the fabrication processes developed for this work.

B.1 Phosphosilicate Glass Etch Recipe

For the best sidewall smoothness, we etched PSG in a Surface Technology Systems Advanced Planar Source inductively-coupled plasma etch system. The etch parameters were as follows:

Coil Power: 1500 W

Bias Power: 350 W

Bias Frequency: 13.56 MHz

C₄F₈ Flow: 15 sccm

H₂ Flow: 8 sccm

He Flow: 174 sccm

Pressure: 4 mTorr

This recipe resulted in consistently less sidewall roughness than other recipes we tried, as described in Chapter 3.

B.2 Silicon Etch Recipe and Sidewall Smoothing

For etching silicon resonators, we used a Lam transformer-coupled plasma (TCP) etcher. The recipe was as follows:

TCP Power: 300 W

Bias Power: 150 W

Cl₂ Flow: 50 sccm

HBr Flow: 150 sccm

For longer etches, the sidewall roughness was too high to achieve reasonable Q_{opt} , so we chemically smoothed the sidewall with three cycles of RCA cleaning, which oxidizes a thin layer of silicon, then removes it. The RCA cleaning steps were:

1. 5 minutes in a 5:1:1 solution of H₂O, H₂O₂, and NH₄OH kept at 75°C on a hotplate
2. 15 seconds in a 50:1 solution of H₂O and 49% HF (removes newly-formed layer of oxide from silicon)
3. 5 minutes in a 6:1:1 solution of H₂O, H₂O₂, and HCl kept at 75°C on a hotplate

B.3 Stoichiometric Silicon Nitride Etch Recipes

We used two different recipes for etching stoichiometric silicon nitride, both of which resulted in similar device performance. This first recipe had some selectivity with respect to both silicon and SiO₂. We performed the etch in an Applied Materials Centura MxP+ Dielectric Etch Chamber, with the following parameters:

Power: 450 W

Ar Flow: 50 sccm

CH₃F Flow: 50 sccm

O₂ Flow: 7 sccm

Pressure: 50 mTorr

The second recipe we used etched SiO₂ at about the same rate as Si₃N₄ and also attacked silicon. However, as our sacrificial material was SiO₂, it was not crucial that we stop accurately on the SiO₂ layer below the nitride device layer. The etching for this process was performed in a Plasma-Therm parallel-plate reactive ion etch tool with the following parameters:

Bias Power: 200 W

Bias Frequency: 13.56 MHz

O₂ Flow: 2 sccm

CHF₃ Flow: 50 sccm

This recipe had an etch rate of stoichiometric Si₃N₄ of about 50 nm/min.